

DISSERTATION

A SPECTRAL ANALYSIS OF THE CRAB NEBULA AND OTHER SOURCES WITH HAWC

Submitted by

Michael Gussert

Department of Physics

In partial fulfillment of the requirements

For the Degree of Doctor of Philosophy

Colorado State University

Fort Collins, Colorado

Fall 2016

Doctoral Committee:

Advisor: John Harton

Co-Advisor: Miguel Mostafa

Walter Toki

Chuck Anderson

Martin P. Gelfand

Copyright by Michael Gussert 2016

All Rights Reserved

## ABSTRACT

### A SPECTRAL ANALYSIS OF THE CRAB NEBULA AND OTHER SOURCES WITH HAWC

The High Altitude Water Cherenkov observatory (HAWC) is an extensive air shower particle detection array designed to study cosmic gamma ( $\gamma$ ) rays in the Very High Energy (VHE) regime (100 GeV to 100 TeV). One of the most thoroughly studied sources in this energy range is the Crab nebula, a pulsar wind nebula created by the aftermath of supernova 1054. The core of this analysis revolves around the determination of the differential flux spectrum of the Crab nebula using a process known as forward folding. Forward folding allows energy spectra to be fit without requiring a direct measurement of the primary energy of individual extensive air showers. The energy resolution of HAWC is very poor (on the order of 50% or more), and so this method is ideal for any spectral analysis carried out with HAWC data. The differential spectra are modeled as a power law with a normalization ( $\Phi_0$ ), spectral index ( $\gamma$ ), and a cutoff energy ( $E_c$ ):  $dN/dE = \Phi_0(E/E_0)^\gamma e^{-E/E_c}$ . The normalization of the Crab nebula was found to be  $1.03 \pm_{0.083}^{0.091} \text{ stat} \pm 0.19 \text{ sys}) \times 10^{-12} (\text{TeV}^{-1} \text{cm}^{-2} \text{s}^{-1})$  with an index of  $-2.54 \pm 0.095 \text{ stat} \pm 0.27 \text{ sys}$  and a cutoff of  $91.0 \pm_{59}^{174} \text{ stat}$  with  $E_0 = 4.0 \text{ TeV}$ . This method was also applied to 11 other sources, and the minimum detection significance required to constrain a spectrum was found to be between 10 and 14  $\sigma$ .

## DEDICATION

*To my Mother, Father, and Sister*

*who are a constant and continual source of strength, inspiration, and encouragement.*

*I don't think I can properly articulate how much you mean to me.*

*To my Papa*

*who kindled my interest in science through frequent trips to the Milwaukee Public Museum  
and with the clever use of Kerplunk.*

*To my Grandma and Grandpa*

*who helped give me the best childhood anyone could hope for, even to this day.*

*To my friends, Josh Shefchik, Adrien Holtzman, and Matt Kitzman*

*who saw me through the roughest parts of my adolescence by tolerating and loving me when  
it seemed like no one else would.*

*To Jackie Schwehr, for being a source of brutal honesty when I needed it most  
and championing me even when I didn't think I deserved it.*

*To Megan Longo, for all those years of sharing an office with me and my constant fidgeting  
and for laughing with me when I fall.*

*To John Pretz, for tolerating my incessant questioning.*

*To John Harton, for being a mentor and advisor when I had none  
and without whom this document would not exist.*

*To Michael Pijoan*

*who walked into my world when I needed him most.*

## TABLE OF CONTENTS

Abstract .....	ii
Dedication .....	iii
List of Tables .....	viii
List of Figures .....	ix
Chapter 1. Light, The Universe, and Everything .....	1
1.1. Cosmic Rays .....	2
1.2. Genesis .....	6
1.3. Types of Sources .....	10
1.4. Extensive Air Showers .....	15
1.5. Detection Methods .....	20
Chapter 2. The High Altitude Water Cherenkov Gamma Ray Observatory .....	28
2.1. Water Cherenkov Detectors (WCD) .....	30
2.2. Photo Multiplier Tubes (PMT) .....	33
2.3. Electronics .....	37
2.4. Online Processing: Edge Finding .....	39
Chapter 3. Offline Reconstruction .....	45
3.1. Calibration .....	45
3.2. Core Fitting .....	49
3.3. Plane and Angular Fitting .....	52
Chapter 4. Simulation .....	57
4.1. CORSIKA .....	57

4.2.	GEANT4 and HAWCsim .....	62
4.3.	SWEETS .....	63
Chapter 5. The Crab Nebula .....		74
5.1.	The Data .....	75
5.2.	Bins and Cutting Variables .....	76
5.3.	Skymaps and the Background .....	86
5.4.	Probability .....	89
5.5.	$\chi^2$ and Models .....	91
5.6.	Forward Folding .....	100
5.7.	Minimization Algorithms .....	101
5.8.	Uncertainties .....	105
5.9.	The Crab Spectrum .....	121
Chapter 6. Other Sources .....		127
6.1.	Markarian 421 .....	128
6.2.	Markarian 501 .....	135
6.3.	HAWC27646-1340 .....	142
6.4.	HAWC27936-0665 .....	145
6.5.	HAWC27980-0583 .....	148
6.6.	HAWC28107-0332 .....	151
6.7.	HAWC28433+0280 .....	154
6.8.	HAWC28710+0643 .....	157
6.9.	HAWC30476+3680 .....	160
6.10.	HAWC30784+4151 .....	163

6.11. Geminga .....	167
Chapter 7. Conclusions, Discussion, Future Work and All That Jazz .....	171
Bibliography .....	175

## LIST OF TABLES

4.1	CORSIKA atmospheric parameters used by HAWC .....	59
5.1	Analysis cut table .....	77
5.2	Optimal bin table.....	82
5.3	fHit systematic cut table for epoch 1 and 2 .....	109
5.4	Optimal Bin Systematic .....	117
5.5	Table of systematic contributions .....	120
7.1	Tabulated Two Parameter Results .....	174
7.2	Tabulated Two Parameter Results .....	174

## LIST OF FIGURES

1.1	Combined CR Spectrum .....	3
1.2	Hillas Plot .....	11
1.3	Cherenkov Radiation .....	21
1.4	MAGIC telescopes .....	22
1.5	Telescope Array FDs .....	25
1.6	Tibet Air Shower Array .....	26
2.1	The HAWC Observatory .....	28
2.2	Sensitivity Plots .....	30
2.3	Diagram of a Water Cherenkov Detector .....	31
2.4	WCD dimensions .....	32
2.5	R5912 Schematic .....	34
2.6	PMT dynodes .....	35
2.7	TOT Schematic .....	40
2.8	Unedged data .....	41
2.9	Edged data .....	42
2.10	Charge Slewing in TOT .....	44
3.1	Reconstructed Shower Core Positions .....	51
3.2	Schematic of a Shower Front Plane .....	52
4.1	Equinoxes and Solstices .....	70
4.2	Stellar transit in local coordinates .....	72

5.1	Energy distributions per bin .....	78
5.2	Optimal bin definition for single Gaussian.....	80
5.3	Shower Simulations .....	84
5.4	Background map example.....	89
5.5	Crab Skymap.....	92
5.6	Crab declination significance histogram .....	93
5.7	Crab $\chi^2$ space for epoch 1 and epoch 2.....	110
5.8	Excess and fit for epoch 1 and epoch 2.....	110
5.9	$\chi^2$ space for epoch 1+2 .....	113
5.10	Excess and fit for epoch 1+2.....	114
5.11	Bin 5 PSF from data .....	115
5.12	Significance vs Angular bin size .....	116
5.13	Data vs Simulation for CxPE40 and PINC.....	118
5.14	PINC and CxPE systematics .....	119
5.15	$\chi^2$ space for Crab spectrum (1 TeV pivot).....	121
5.16	Crab Excess (two parameters) .....	122
5.17	$\chi^2$ space for Crab spectrum (4 TeV pivot) .....	123
5.18	Crab Excess (three parameters).....	124
5.19	$\chi^2$ space for Crab spectrum (4 TeV pivot, three parameters) .....	125
5.20	Crab $\chi^2$ of Index Vs log(Cutoff) .....	125
5.21	Crab $\chi^2$ of Index Vs log(Normalization).....	126
5.22	Crab $\chi^2$ of log(Normalization) Vs log(Cutoff) .....	126

6.1	Markarian 421 skymap.....	129
6.2	Markarian 421 2 parameter excess .....	130
6.3	Markarian 421 three parameter excess.....	131
6.4	Markarian 421 $\chi^2$ space in 2 parameters.....	132
6.5	$\chi^2$ space for Markarian421 spectrum (4 TeV pivot, three parameters) .....	133
6.6	Markarian421 $\chi^2$ of Index Vs log(Cutoff).....	133
6.7	Markarian421 $\chi^2$ of Index Vs log(Normalization).....	134
6.8	Markarian421 $\chi^2$ of log(Normalization) Vs log(Cutoff) .....	134
6.9	Markarian 421 skymap.....	136
6.10	Markarian 421 2 parameter excess .....	137
6.11	Markarian 421 three parameter excess.....	138
6.12	Markarian 421 $\chi^2$ space in 2 parameters.....	139
6.13	$\chi^2$ space for Markarian501 spectrum (4 TeV pivot, three parameters) .....	140
6.14	Markarian501 $\chi^2$ of Index Vs log(Cutoff).....	140
6.15	Markarian501 $\chi^2$ of Index Vs log(Normalization).....	141
6.16	Markarian501 $\chi^2$ of log(Normalization) Vs log(Cutoff) .....	141
6.17	HAWC27646-1340 map .....	142
6.18	HAWC27646-1340 excess.....	143
6.19	HAWC27646-1340 $\chi^2$ space .....	144
6.20	HAWC27936-0665 map .....	145
6.21	HAWC27936-0665 excess.....	146
6.22	HAWC27936-0665 $\chi^2$ space .....	147

6.23	HAWC27980-0583 map .....	148
6.24	HAWC27980-0583 excess.....	149
6.25	HAWC27980-0583 $\chi^2$ space .....	150
6.26	HAWC28107-0332 map .....	151
6.27	HAWC28107-0332 excess.....	152
6.28	HAWC28107-0332 $\chi^2$ space .....	153
6.29	HAWC28433+0280 map .....	154
6.30	HAWC28433+0280 excess.....	155
6.31	HAWC28433+0280 $\chi^2$ space .....	156
6.32	HAWC28710+0643 map .....	157
6.33	HAWC28710+0643 excess.....	158
6.34	HAWC28710+0643 $\chi^2$ space .....	159
6.35	HAWC30476+3680 map .....	160
6.36	HAWC30476+3680 excess.....	161
6.37	HAWC30476+3680 $\chi^2$ space .....	162
6.38	HAWC30784+4151 map .....	164
6.39	HAWC30784+4151 excess.....	165
6.40	HAWC30784+4151 $\chi^2$ space .....	166
6.41	Geminga skymap .....	168
6.42	Geminga excess.....	169
6.43	Geminga $\chi^2$ space .....	170

7.1 Combined  $\chi^2$  space for two parameter fit results).....173

## CHAPTER 1

# LIGHT, THE UNIVERSE, AND EVERYTHING

The electromagnetic spectrum is vast. The part which we can see with the naked eye accounts for only the tiniest fraction of a percent of the “labeled” portion of the spectrum, which spans from the end of long waves with wavelengths on the order of a kilometer, to the beginning of gamma rays, with wavelengths on the order of a fraction of a nanometer. Yet, blind as we are, the universe yields a great many secrets to the visual spectrum, as early astronomers quickly discovered. With the visual light alone, we proved the heliocentric model of our solar system. We numbered our planetary neighbors and uncovered the secrets of their creation. We found comets and asteroids and meteors. We discovered galaxies and even our location within the Milky Way.

However, as potent a tool as the visual spectrum has proven to be, more can be learned by examining the universe through the lenses of different spectral ranges. In fact, one of the greatest discoveries in modern astronomy was made with the poorly named Microwave spectrum <sup>1</sup>. This discovery was of an isotropic, very nearly homogeneous field of microwave radiation which we now know as the Cosmic Microwave Background (CMB). The CMB has taught us about the origin of the universe itself, and how the cosmos, as we know it, was formed. It is easily one of the greatest pieces of astrophysical evidence ever discovered and it was found through the examination of non-visual light.

As is often the case in physics, the most interesting discoveries are found in the extreme frontiers. What can we see when we look through the lens of the most energetic light in the universe? What new pieces of astrophysical evidence might we find? We call photons with energies beyond the end of the x-ray spectrum Gamma Rays ( $\gamma$ ), and six orders of magnitude

---

<sup>1</sup>Microwaves do not have wavelengths on the order of micrometers.

past this point is the region of interest for this thesis: The Very High Energy (VHE)  $\gamma$ -ray Spectrum. This introductory chapter will serve to examine the “story” of VHE  $\gamma$ -rays, from their creation to their eventual detection, and will provide the necessary background for the rest of this document.

## 1.1. COSMIC RAYS

When discussing VHE gamma rays, with energies between 100 GeV and 100 TeV, it is important to also examine cosmic rays, which form the principle background for most VHE gamma ray experiments. Cosmic rays are a type of cosmogenic radiation composed of bare atomic nuclei, which strike the top of the atmosphere of the Earth. Many of the physical systems responsible for the creation of cosmic rays often create gamma rays as well. The distribution of the differential flux as a function of the energy of this radiation is known as the cosmic ray spectrum. For the most part, the cosmic ray spectrum obeys a power law,

$$(1) \quad \frac{dN}{dE} \propto E^{-\gamma} ,$$

with a spectral index,  $\gamma$ , of approximately 2.7 [1] (see fig 1.1).

The cosmic ray spectrum is divided into three distinct regions: solar, galactic, and extragalactic. Solar cosmic rays, contrary to the name, do not come from the sun but are instead modulated by solar activity (with the exception perhaps of particles associated with solar flares). The solar wind, an expanding magnetized plasma generated by the Sun, partially excludes lower energy galactic cosmic rays from the interior of the solar system. As a result of this effect, the intensity of cosmic rays with energies below about 10 GeV strongly anticorrelates with the 11 year solar cycle [1] .

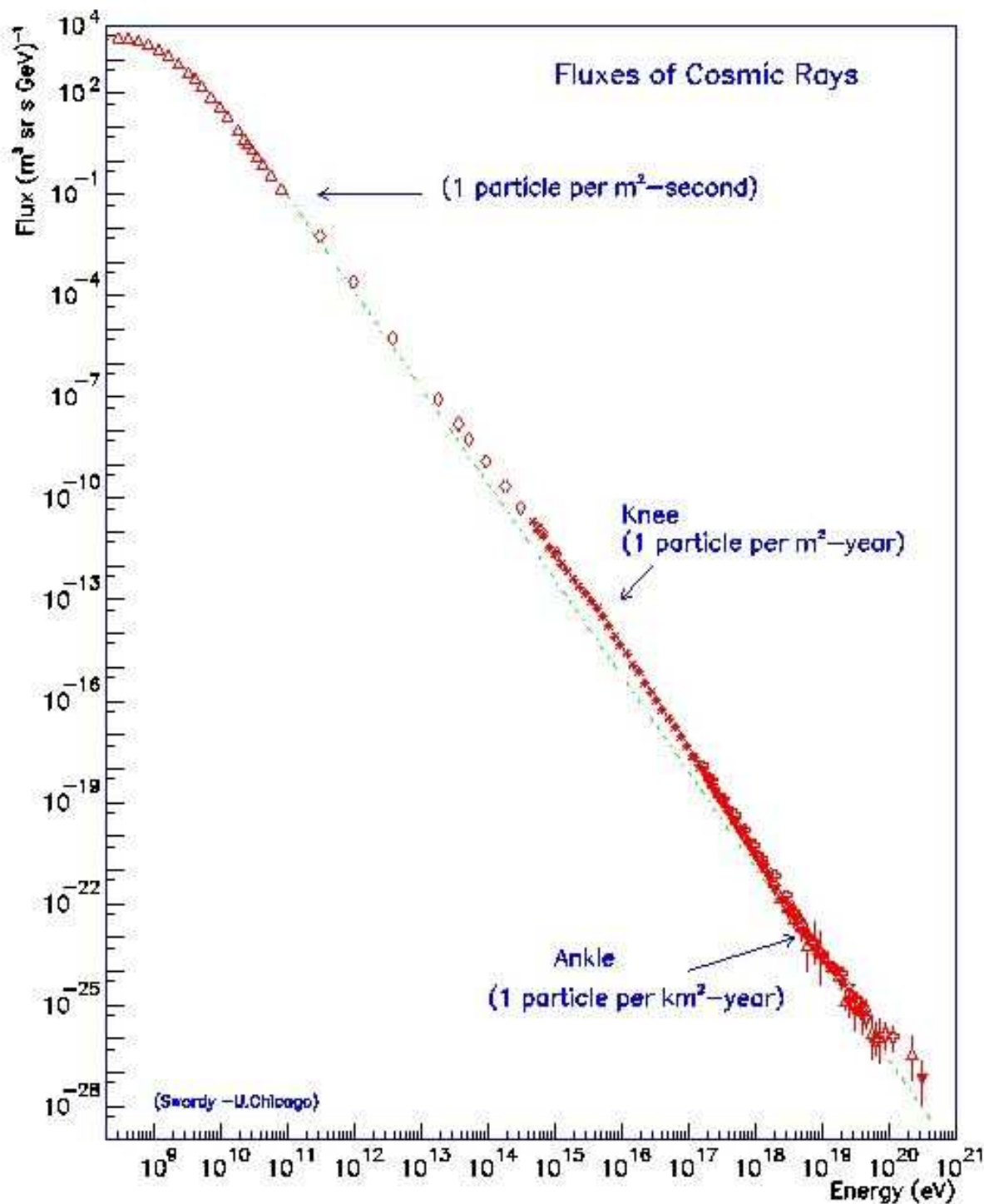


FIGURE 1.1. Combined cosmic ray spectrum from various experiments, from [2]

Galactic cosmic rays are just that: cosmic rays with an origin within the Milky Way.

The galactic cosmic ray spectrum begins at energies above 10 GeV and extends up to 1 PeV

( $10^{15}$  eV), where the spectrum begins to gradually transition into the extragalactic regime. The beginning of this transition region is marked by a change in the spectral index known as “the knee”, where  $\gamma$  softens to a value of 3.1.<sup>2</sup> This transition occurs because cosmic rays with energies above 1 PeV have a Larmor radius which begins approaching the thickness of the galactic plane. The Larmor radius (or cyclotron radius) is defined as the radius of the circular trajectory followed by a charged particle in a uniform magnetic field. While the galactic magnetic field is by no means uniform, as a general rule the Larmor radius  $r_L$  for galactic cosmic rays can be approximated by

$$(2) \quad r_L \simeq 1 \text{ kpc} \frac{E[\text{EeV}]}{ZB[\mu\text{G}]},$$

where  $E$  is the particle energy in EeV,  $Z$  is the charge in units of the electron charge, and  $B$  is the magnetic flux density in  $\mu\text{G}$  [3]. The galactic magnetic field has an average flux density of about  $10 \mu\text{G}$  [4] so protons with an energy of 1 PeV have a Larmor radius of about 0.1 pc (a pc, or parsec is a unit of cosmic distance and is approximately three light years). The stellar disk of the Milky Way has a thickness of about 600 pc, so protons with an energy  $\leq 1$  PeV have virtually no chance of escaping. As the energy increases, this radius increases, and at about 1 EeV the Larmor radius of a proton is almost 20% of the thickness of the stellar disk. Assuming galactic cosmic rays have been created since the birth of the Milky Way, particles with energies below the knee are trapped by the galactic magnetic field and will almost certainly remain so until they interact. Higher energy particles have a greater chance of escaping, and when they do they can never be observed on Earth. It stands to reason

---

<sup>2</sup>“Soft” energies are lower than “hard” energies. Because the index increases, the slope of the spectrum increases negatively, reducing the flux of higher energies, thus softening the spectrum

that cosmic rays observed below this transition energy were most likely created within the Milky Way while cosmic rays with observed energies increasingly larger than the knee are more and more likely extragalactic in origin.

Extragalactic cosmic rays come from origins outside our galaxy and dominate the spectrum at and above 1EeV. Cosmic rays in this energy range begin to be subjected to an effect known as the Greisen—Zatsepin—Kuzmin (GZK) cutoff. The GZK cutoff theory describes a soft upper limit on the energy of extragalactic cosmic rays of a cosmologically distant origin (greater than about 50 Mpc). This upper limit begins at 50 EeV for protons and the CR spectrum should be suppressed above this energy (the index should steepen). Cosmic rays (specifically protons) at or above this energy coming from beyond 50 Mpc will therefore interact with the cosmic microwave background via resonance with  $\Delta^+$ , which immediately decays into a nucleon and a  $\pi^+$  or  $\pi^0$  [5][6]. The  $\pi^+$  will decay into a muon and neutrino while the  $\pi^0$  will decay to photons. The free neutrons will ultimately decay to protons, electrons, and antineutrinos. The end result is that the initial energy of the proton has been drained away through these decay channels, leaving only the lower energy decay products and thus reducing the flux at energies above the cutoff. The GZK cutoff has been observed by both the Pierre Auger Observatory and HiRes [7][8]

The production of electromagnetic radiation hinges on the acceleration and interactions of charged particles. In the end, all  $\gamma$ -ray producing astrophysical phenomena take the form of naturally occurring particle accelerators. In order to achieve  $\gamma$ -ray energies between 1 GeV and 100 TeV, these accelerators must be exceedingly violent or exotic in nature. The question to ask is a simple one. Where do these  $\gamma$ -rays get their energy?

## 1.2. GENESIS

The particle interactions that result in  $\gamma$ -rays fall into four broad categories: Bremsstrahlung, scattering, annihilation, and decay. All other possible production methods eventually boil down to these four channels. Bremsstrahlung radiation is, strictly speaking, photonic radiation that results from the acceleration of charged particles, and directly translates from German as “braking radiation”. Bremsstrahlung radiation includes cyclotron and synchrotron radiation as more specific forms.

Scattering refers to particle interactions that result in the exchange of energy or possibly the creation of new particles. In the context of  $\gamma$ -ray production the most important form of scattering is that of inverse Compton scattering. Compton scattering is the mechanism through which high energy photons scatter low energy electrons to higher energies, resulting in a low energy photon. Inverse Compton scattering is simply the reverse: low energy photons scatter high energy electrons to lower energies, resulting in a high energy photon. The resulting final energy of the scattered photon is a function of scattering angle and the energy of the electron.

Annihilation occurs when a particle interacts with its antimatter counterpart. There are many different channels annihilation interactions can take, but it can commonly result in two photons. This is a frequent occurrence because most quantum numbers (charge, flavor, color etc.) are inverted between a particle and its antiparticle counterpart, forcing the byproducts of the interaction to have those numbers be zero as well by conservation. These annihilation channels are important because they produce discernible features in the gamma ray spectrum of a source. These features can yield important information concerning the composition of the matter that forms the source, and the energies of the physical processes at work therein.

The final production channel describes how  $\gamma$ -rays are created as the byproducts of the decay of a separate parent particle. One of the most common astrophysical decay channels for gamma rays is  $\pi^\circ$  decay, that results in two  $\gamma$ -rays, but there are many other channels that can lead to photons.

Particle interactions represent the finer points when describing the creation of VHE  $\gamma$ -rays. That is not to say that they aren't important, but rather, some larger mechanism needs to be at work in order to get particles up to the necessary energies required for interactions to produce VHE  $\gamma$ -rays. These mechanisms are the natural particle accelerators of the universe, all of which arise from the interactions of electromagnetic and gravitational fields.

Gravitational fields can create particle accelerators by directly converting gravitational potential energy into kinetic energy. One system which commonly accelerates particles in this fashion are accretor-donor systems. Accretor-donor systems consist of a donor, such as a large nearby star or nebula, and an accretor, which is usually a compact object such as a black hole or neutron star. Matter from the donor falls through the gravitational field of the compact object where it accretes and gains kinetic energy. Conservation of angular momentum forces the accreted matter into a quickly spinning disk, where it has enough energy to interact and produce VHE  $\gamma$ -rays. There are many types of accretor-donor systems based on what objects compose them, but the principle is always the same. Gravitational acceleration of charged particles can also occur in the early stages of certain types of supernovae involving extremely massive, iron-fusing stars. When such a star runs out of fuel, the surrounding layers of matter fall inwards towards the core, gaining kinetic energy. Eventually these layers can cannot fall any farther and quite literally bounce back outwards forming a supernova. This process is known as core collapse and the gravitational

potential energy of the collapsing matter provides a portion of the energy for the resulting explosion.

Electromagnetic fields that accelerate charged particles up to GeV and TeV range are almost exclusively found in shock wave fronts. In the case of accretor-donor systems matter that does not fall onto the accretor is launched perpendicular to the accretion disk, forming jets of tightly confined plasma. The difference in velocity between the dense plasma of the jets and the interstellar medium forms shock fronts. The magnetic fields produced by these fronts are extremely ridged with respect to the interstellar medium (that is, they very easily change the momentum of charged particles entering the field from outside the shock) and randomized in direction. Low energy charged particles entering a jet shock front are temporarily trapped by this magnetic field, but eventually gain enough energy from the velocity of the shock to escape. The rapid, frequent, and randomized acceleration of charged particles in the the shock front of accretion jets may be one of the most likely sources of high energy cosmic rays, and therefore  $\gamma$ -rays. Shock fronts also occur as a result of particularly violent explosions such as those created by supernovae. Supernovae create a “short”<sup>3</sup> burst of cosmic and  $\gamma$ -rays when they occur, but result in more steady sources as the resulting shock wave expands into the interstellar medium and bounces particles up to higher energies. The mechanism by which such shock fronts impart energy to charged particles is known as Fermi-acceleration [9].

Fermi-acceleration is an attractive hypothesis for natural particle acceleration because it results in the power law spectrum noted in equation (1), and this can be shown through very simple arguments [10]. Suppose that with every cycle of acceleration in a shock front, a charged particle gains energy some amount of energy that depends on the initial energy

---

<sup>3</sup>Short with respect to the lifetime of the star that created the super nova. SN1054 was visibly detectable with the naked eye for approximately two years before fading from view.

of the particle,  $E_o$ . Classically this makes sense; a ball bouncing elastically off of a moving wall will have a reflected speed equal to the sum of the initial speed and the speed of the wall, so the assumption that the reflected energy depends on the initial initial energy is not too wild.

$$(3) \quad \Delta E = a E_o .$$

After  $n$  cycles of acceleration, the final energy of the particle is given by

$$(4) \quad E = E_o(1 + a)^n .$$

After every cycle of acceleration, the probability that a particle escapes further cycles increases slightly. Suppose the probability that a particle remains in the accelerator after a single cycle is  $P$ . If there are  $N_o$  particles initially, then the number of particles remaining after  $n$  cycles is

$$(5) \quad N = N_o P^n$$

$$(6) \quad \ln\left(\frac{N}{N_o}\right) = n \ln(P) .$$

Solving for  $n$  in (4) and substituting into (6) yields

$$(7) \quad \ln\left(\frac{N}{N_o}\right) = - \frac{\ln(E_o/E) \ln(P)}{\ln(1 + a)}$$

$$(8) \quad N = N_o \left(\frac{E_o}{E}\right)^{-\ln(P)/\ln(1+a)}$$

$$(9) \quad = N_o \left(\frac{E_o}{E}\right)^s .$$

Taking a derivative with respect to  $E$  results in a form which agrees with (1).

$$(10) \quad \frac{dN}{dE} = C E^{-(s+1)}$$

$$(11) \quad = C E^{-\gamma},$$

where  $C$  is a constant. This shows that the spectral index  $\gamma$  is dependent only on the likelihood that a particle escapes the shock front and the amount of energy it gains each shock cycle. These in turn are dependent on the magnetic field density of the source, the velocity of the shock front relative to the interstellar medium, and geometry (see fig 1.2).

### 1.3. TYPES OF SOURCES

A  $\gamma$ -ray source is the origin of some  $\gamma$ -ray flux. These sources can be diffuse, covering large angular regions of the sky on the order of several degrees or point-like, spanning a real angular region much less than the angular resolution of most detectors. Sources can also be transient, meaning that they only exist for short periods of time on the order of seconds or minutes, or steady, meaning that they are permanent fixtures on sky. This thesis focuses only on steady point sources.

There are many types of sources, but they can be grouped into one of six broad categories: oscillators, shells, active galaxies, star clusters, starburst galaxies, and Pulsar Wind Nebulae (PWNe). These are the categories used to divide registered sources on the TeV catalog (<http://tevcat.uchicago.edu/>) which serves as the central archive of confirmed VHE gamma ray sources.

#### 1.3.1. OSCILLATORS.

Oscillators consist of X-ray binary systems,  $\gamma$ -ray binary systems, and pulsars. In short,

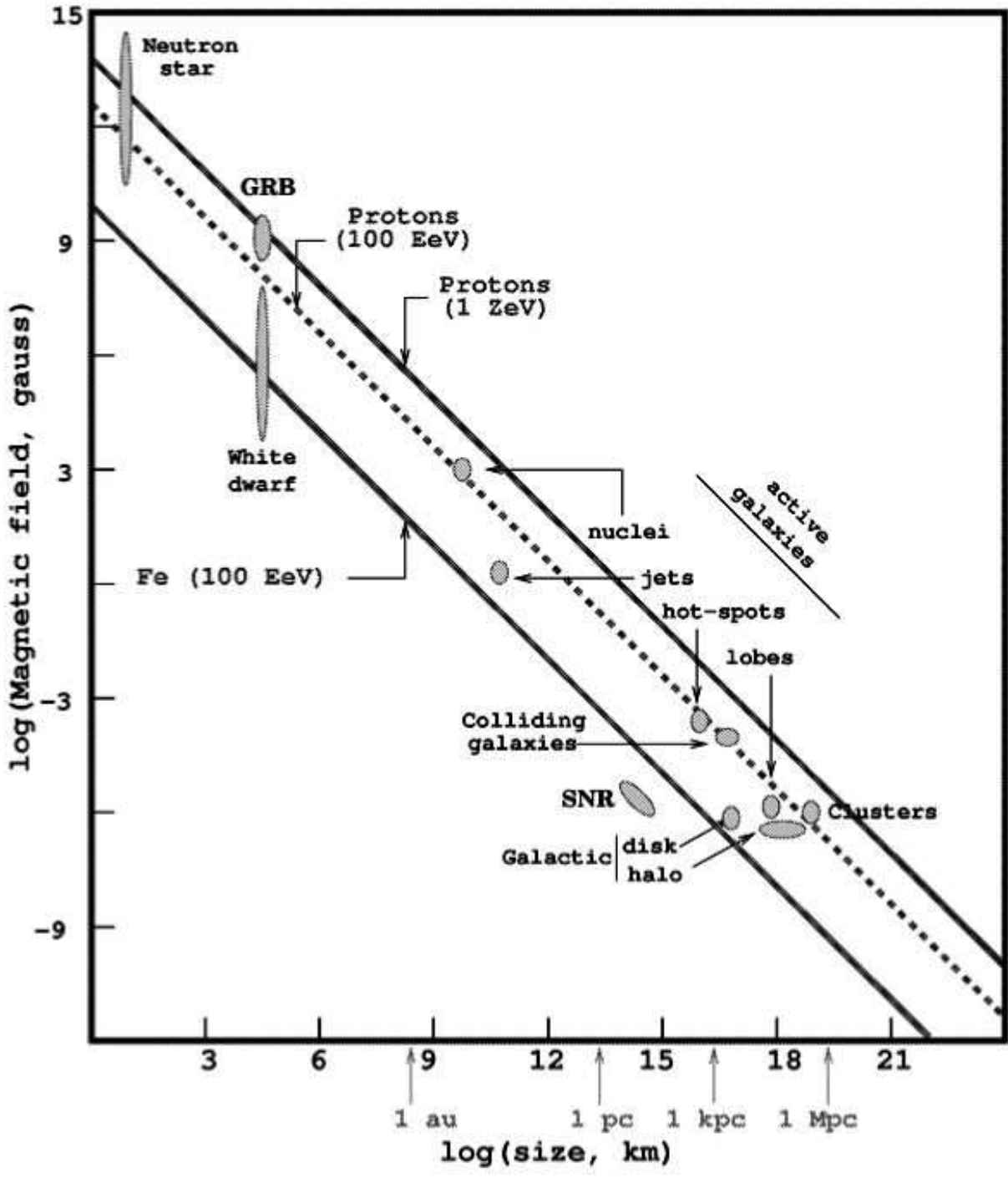


FIGURE 1.2. A Hillas plot indicating the relationship between size and field strength for various cosmic accelerators. The acceleration of protons to above 1 ZeV or Iron to above .1 ZeV require physical conditions above the solid lines [11]

they are objects with an intensity that oscillates in time <sup>4</sup>. Binary systems are those with two stars that orbit each other. The discovery of binary systems that emit in the VHE regime is a very recent one. Indeed, at the time of this writing there are only five binary sources registered, all of which were discovered after 2009. The exact mechanism that governs VHE  $\gamma$ -ray production in these binary systems is still a mystery, however, all five systems house a massive type O or B(e) star with masses between  $10\text{-}20M_{\odot}$  and radii of about  $10R_{\odot}$  [12]. This suggests an accretor-donor system where the resulting  $\gamma$ -rays are created by the interaction between highly energetic particles which have fallen through the resulting gravitational potential difference.

A pulsar is a rapidly rotating neutron star (a highly compact object composed almost entirely of neutrons) which then precesses about a secondary rotational axis. The primary rotational poles of a pulsar emit highly beamed electromagnetic radiation resulting from the conversion of the rotational kinetic energy of the star into a strong, moving magnetic field. This field then accelerates protons and electrons near the surface of the star, resulting in a tight beam of electromagnetic radiation. This radiation can only be observed when the secondary axis of rotation causes the beam to point at the Earth. These objects were first observed in the radio spectrum, but recently, GeV pulses have been observed from the Crab Pulsar, Geminga, and Vela. These are considered separate sources from respective nebulae containing them because the light from pulsars is steadily pulsed, and can therefore be isolated. As an example, the Crab pulsar emits only about 1% of the flux as the Crab nebula and cuts off at an energy of about 150 GeV, while the nebula is steady up to about 700 GeV [13].

---

<sup>4</sup>MRK421 is an Active Galactic Nuclei. These categories are structurally defined instead of behaviorally defined. MRK421 would be considered a steady point source with transient flaring

### 1.3.2. SHELLS.

Shell sources consist of Super Nova Remnants (SNRs), superbubbles, and their nearby molecular clouds. SNRs are the lasting remains of supernovae, and consist of an expanding shell of hot, dense plasma. VHE  $\gamma$ -ray production occurs as a result of shock acceleration in the shell as it expands into the interstellar medium. This expansion can last for hundreds or thousands of years and SNRs can expand to be tens of parsecs in diameter before the expansion rate begins to markedly decrease. Superbubbles are simply compound SNRs that can expand to sizes on the order of a hundred parsecs or so. Molecular clouds are large clouds of stable molecules, unlike the interstellar medium or SNRs, which are both plasmas. They are also grouped into this category because when they are close enough to SNRs or are deformed by SNR shocks, they can serve as secondary targets for cosmic rays created by the nearby shell. Shell type sources are one of the most numerous sources of cosmic rays in the Milky Way.

### 1.3.3. ACTIVE GALAXIES.

Active galaxies are galaxies which host an Active Galactic Nucleus (AGN). An AGN is a compact, highly luminous region at the center of some galaxies. It is believed that the radiation observed from AGN is the result of matter accreting onto a supermassive black hole (black holes with masses between  $10^5$ - $10^9 M_{\odot}$ ). This makes AGN's accretor-donor systems, only in this case the donors consists of entire star systems. AGN are primarily characterized by the presence of massive, relativistic jets composed of matter that failed to fall into the black hole. These jets can be on the order of kiloparsecs in length (defined by the change in density at the shock front), and are thought to be the source of the highest energy cosmic rays. A number of objects which were once thought to be unique are actually just AGNs viewed from different perspectives. When the jets of an AGN are perpendicular

to the line of sight from earth, it appears as a radio galaxy (the light it emits in the direction of the earth is most intense in the radio spectrum). When the jets of an AGN are neither perpendicular or coincident with the line of sight from earth, they are called quasars. When the jets are coincident with the line of sight from earth, they are called blazars. The closer the jets of an AGN align with line of sight, the more VHE  $\gamma$ -rays are detected from that AGN. There are many sub-types of AGNs, but any source playing host to an active nucleus falls into this category.

#### 1.3.4. STAR CLUSTERS.

Star cluster sources are composed of more than one star / object, but are not galaxies. Globular clusters and galactic star forming regions are volumes containing numerous stars and source objects that, for one reason or another, are highly active. An example of this kind of source is Terzan 5, which is a globular cluster near the bulge of the Milky Way. There are as many as 200 radio pulsars, 50 weak X-ray sources, and at least 1 X-ray burster, all within a radius of 2.7 light years [14][15][16]. To put that in perspective, the nearest neighbor to Sol<sup>5</sup> is Proxima Centauri, at 4.2 light years away. Terzan 5 exhibits a diffuse, non-thermal VHE  $\gamma$ -ray emissions up to 24 TeV [15].

#### 1.3.5. STARBURST GALAXIES.

Starburst galaxies are galaxies that exhibit an extremely high rate of star formation. The associated stellar activity results in shock acceleration of cosmic rays, which can lead to VHE photons. Starbursts usually occur as a phase in the evolution of a galaxy or as the result of a collision or interaction between galaxies. The most recent source discovered in this category is Messier 82, the cigar galaxy. It is approximately five times more luminous than all of the Milky Way as a result of starburst formations due to interactions with Messier 81, Bode's

---

<sup>5</sup>The sun

galaxy [17]. At the time of this writing there have been only two starburst galaxies detected in the VHE  $\gamma$ -ray regime: M82 and NGC 253.

#### 1.3.6. PULSAR WIND NEBULAE.

Pulsar Wind Nebulae (PWN) are the most numerous of the TeV  $\gamma$ -ray sources in our galaxy. They consist of a central pulsar enveloped by a SNR. The electromagnetic and particle “wind” from the pulsar powers VHE  $\gamma$ -ray production in the surrounding SNR. The most luminous and steady PWN is the Crab nebula, which will be covered in detail in a separate chapter.

#### 1.3.7. UNIDENTIFIED.

Unidentified sources are just that: Unidentified. These are distinct sources that either do not exhibit any properties which would place them in one of the above categories, or have conflicting identifications across several experiments. VHE  $\gamma$ -ray sources that do not have any other obvious counterpart in other wavelengths are classified as dark sources, and are also placed in this category. There is currently only one dark source registered: HESS J1503-582 [18].

### 1.4. EXTENSIVE AIR SHOWERS

The atmosphere is completely opaque to VHE cosmic radiation and so it behaves as a collision target for both  $\gamma$ -rays and cosmic rays. When such radiation (known as primary radiation) interacts with the atmosphere it produces a large number of secondary particles in a series of successive collisions with atmospheric nuclei (usually nitrogen and oxygen). These in turn produce more secondaries which then continue on, repeating the process, creating a cascade of particles known as an Extensive Air Shower (EAS). EAS serve as the only channel

through which some ground based particle astrophysics experiments can detect VHE cosmic radiation.

Extensive air showers are extremely difficult to properly describe as a result of the sheer number and types of interaction that can occur. Before specific physics can be discussed it is necessary to set up a scaffolding of definitions and concepts, most importantly the coordinate system and parameters used to describe EAS. The primary coordinate axis used to describe an EAS is called the longitudinal axis. It is defined as a line from the point of first interaction to the point on the surface of the earth where the primary particle would land without the presence of the atmosphere. The development of an EAS along the longitudinal axis is parameterized by atmospheric depth. Atmospheric depth is a measure of the quantity of atmosphere through which the shower core has propagated. It is defined by the barometric formula, which assumes that atmosphere is isothermal<sup>6</sup>

$$(12) \quad X(h) = X_o e^{\frac{h}{h_s}} \text{ [g cm}^{-2}\text{]} .$$

This equation describes the mass of atmosphere contained in a column of above height  $h$ , with a cross sectional area of  $1 \text{ cm}^2$ . Here,  $X_o$  is the depth of the atmosphere at sea level ( $1,030 \text{ g cm}^{-2}$ ) and  $h_s$  is the characteristic height ( $8.4 \text{ km}$ )<sup>7</sup>. Because the development of an EAS is parameterized by its atmospheric depth, this quantity is also referred to as the “age” of a shower, with “younger” showers having penetrated through less atmosphere than “older” ones. The secondary coordinate axis used to describe an EAS is called the lateral plane, and is simply defined as the plane normal to the longitudinal axis at a specific atmospheric depth.

---

<sup>6</sup>The barometric equation is derived under the assumption of an isothermal atmosphere. Complex atmospheric models that utilize the barometric equation do so in isothermal layers (usually 5 or 6). The temperature in a given layer is affected in  $X_o$ .

<sup>7</sup>The atmospheric depth depends on the angle, as  $h$  is measured along the primary axis of the shower. Highly inclined showers traverse more atmosphere than vertical showers

At any given point in time, all particles within an EAS are defined with respect to the lateral plane and longitudinal axis, and the foremost edge of an EAS is known as the shower front, which contains the vast majority of particles in the cascade.

Extensive air showers are described by the development of the shower longitudinally (along the momentum of the primary) and laterally (perpendicular to the momentum of the primary). The longitudinal development of the shower is governed by the number of particles produced by interactions as a function of depth within the atmosphere, which is known as the longitudinal distribution. As more and more secondaries are produced throughout the lifetime of the EAS, each secondary will carry a smaller and smaller fraction of the total energy of the primary. Eventually this fraction will be so small that particles within the shower will have insufficient energy to produce more secondaries. As a result, the number of particles rapidly increases to some maximum value at some atmospheric depth, and then gradually begins to fall off. The depth at which the maximum number of particles are present in the shower is dependent on the zenith angle and energy of the primary particle.

A toy model of this process can be developed by considering a vertical cascade consisting of identical particles that interact after some interaction length,  $\lambda$  to produce exactly two secondary particles of the same type. Suppose this cascade is initiated by a primary particle with an energy of  $E_o$ . After one interaction length the cascade consists of two particles, each with half the energy of the primary,  $E_o/2$ . After two interaction lengths there are  $2^2$  particles, each with an energy of  $E_o/2^2$  and so on. This suggests that the number of particles at a depth  $X = N\lambda$  is  $2^N$  where  $N$  is the number of interaction lengths through which the cascade has propagated. Eventually the energy of individual particles will reach some critical energy,  $E_c$ , where they cease interacting with the medium <sup>8</sup>, and no new particles will be

---

<sup>8</sup>Remember, this is a toy model. In reality these particles may continue ionizing the atmosphere even past the critical energy.

produced. The maximum number of particles that could possibly be present in this cascade,  $P_{max}$ , is the ratio between the primary and critical energy of the cascade. If the number of particles in the cascade goes as  $2^N$  then the maximum number of interaction lengths  $N_{max}$  is  $\log_2(E_o/E_c)$  and so the maximum depth of the shower is

$$(13) \quad X_{max} = \lambda \log_2 \left( \frac{E_o}{E_c} \right).$$

From this, the toy model reveals two very important pieces of information about the development of showers. First is that the maximum depth of the longitudinal distribution varies logarithmically with the primary energy, and second is that the number of particles in the cascade at the maximum depth is proportional to the primary energy.

The lateral development of an EAS is dependent on the number of particles with momenta transverse to the longitudinal axis. The 2D distribution of particles defined on the lateral plane is known as the lateral distribution. The lateral distribution is dependent on the type and number of possible interaction channels that are present in the shower. For example, the interaction of leptons and gamma rays within an EAS is governed by electromagnetic processes, including bremsstrahlung, which can create photons that are highly beamed. Hadronic process produce more particles with large momenta in the lateral plane than the electromagnetic component. The result of this is that electromagnetic showers are more laterally compact than hadron showers.

Indeed, the characteristics of an EAS are strongly dependent on the type of the primary particle. Most EAS are initiated by hadron primaries and can be thought of as three separate particle cascades occurring simultaneously, each described by the types of interactions which govern the production of secondaries: the nuclear cascade, the mesonic cascade, and the electromagnetic cascade. The nuclear cascade of an EAS occurs from interactions between

protons and neutrons. Nuclear debris from the primary interaction shatters other atmospheric nuclei, which in turn do the same. There are many byproducts that can occur from such interactions other than atomic nuclei, but the most common are  $\pi^\pm$ ,  $\pi^0$ ,  $K^\pm$ , and  $K^0$ . The charged mesons either strike other atomic nuclei, propagating the nuclear component, or quickly decay into  $\mu^\pm$  and neutrinos, which then penetrate down to the surface of the earth. The mesons which do not interact nuclearly are the mesonic component of an EAS, and the secondary particles produced in this cascade (muons and neutrinos) will almost certainly reach the surface of the earth before interacting. The neutral mesons initiate the electromagnetic cascade. These decay into photons, which then pair produce into leptons and in turn create more photons either through annihilation or bremsstrahlung. These interactions continue successively until the particles reach the surface of the earth. Often the nuclear and meson portions of an EAS are described as the “hard component” of the shower because they can penetrate deeply into the atmosphere and, indeed, the earth. The electromagnetic cascade is usually referred to as the “soft component”.

Extensive air showers initiated by a photon primary are almost exclusively electromagnetic particle cascades. Muons are still present in  $\gamma$ -ray primary showers, but there are significantly fewer of them than in a hadronic shower. This is because there are really only two ways to produce muons in an EM cascade. The first is through the single photon pair production of muons. Technically speaking, so long as a photon has an energy of at least  $2m$  where  $m$  is the mass of any lepton, pair production through that lepton channel is possible. That said, single photon pair production can only occur in the presence of heavy atomic nuclei for kinematic reasons, which suggests that there is a mass dependence on the single photon pair production cross section. Indeed, this cross section has been calculated [19] and it is proportional to  $m^{-2}$ , which means that  $e^+e^-$  pair production is over forty thousand

times more likely than  $\mu^+\mu^-$  and more than twelve million times more likely than  $\tau^+\tau^-$ . So muons can be created through single photon pair production in EM cascades, but only very rarely. The other possible source of muons in EM cascades comes from photonuclear interactions, which can create a short lived nuclear shower resulting in charged mesons and therefore muons, but again, the likelihood of this is small.

## 1.5. DETECTION METHODS

An EAS is characterized by the thin but radially extended shower front, which propagates at essentially the speed of light along the longitudinal axis. Detection of an EAS involves either the direct detection of the particles in this front, or the detection of effects produced by this front. These effects include Cherenkov light, air fluorescence, radio emissions, atmospheric ion recombination, and even acoustic vibrations. The first three effects, Cherenkov, fluorescence, and radio emissions, as well as particle detection arrays are presently employed in live astroparticle physics experiments. The remaining effects have yet to be actually employed (and EAS acoustic signals are still purely hypothetical).

### 1.5.1. IMAGING AIR CHERENKOV TELESCOPES (IACTs).

Cherenkov radiation results from the passage of charged particles through some medium at a speed greater than the speed of light in that medium. The result of the particle traveling faster than electromagnetic waves in that medium results in a conic, constructive phase front of photons not unlike a sonic boom. The cosine of the opening angle of this radiation is the ratio between the speed of light in the medium and the speed of the particle (see fig. 1.3)

Cosmic rays moving at highly relativistic velocities ( $\beta \approx 1$ ) can create EAS which emit Cherenkov radiation within the atmosphere. This radiation can be detected by specially designed telescopes known as Imaging Air Cherenkov Telescopes (IACTs).

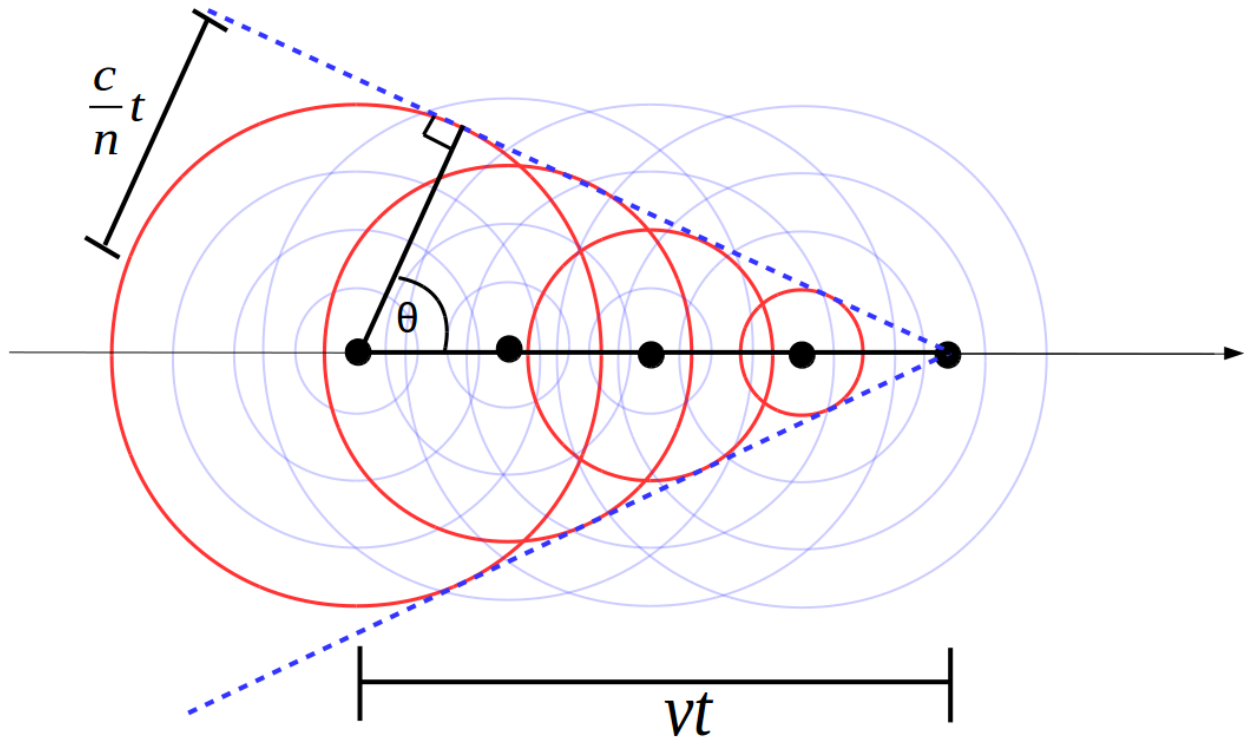


FIGURE 1.3. A 2D schematic of the conic, constructive phase front formed by a particle radiating cherenkov radiation.

IACTs consist of a large, segmented concave mirror that focuses down to an array of highly sensitive PhotoMultiplier Tubes (PMTs) (see chapter 2). These PMTs are monitored by extremely fast electronics which amplify, digitizes, and save the pattern of Cherenkov light created by the activation of the PMT array. These data are in turn used to reconstruct the geometry and energy of the shower. By creating an array of IACTs the detection sensitivity and angular resolution can be increased by requiring a shower to trigger multiple IACTs at once. A prime example of an IACT array can be seen in the MAGIC (Major Atmospheric Gamma imaging Cherenkov Telescopes) experiment, which consists of two, 17m diameter

IACTs located at the Roque de los Muchachos Observatory on La Palma, one of the Canary Islands (see fig 1.4)



FIGURE 1.4. The two MAGIC IACTs. Photo retrieved June 9, 2016 from [https://commons.wikimedia.org/wiki/File:MAGIC\\_Telescope\\_-\\_La\\_Palma.JPG](https://commons.wikimedia.org/wiki/File:MAGIC_Telescope_-_La_Palma.JPG) under the Creative Commons Attribution-Share Alike 3.0 Unported License.

The advantage of using IACTs to detect EAS lies in the ability to detect an EAS as it propagates through the atmosphere. Information about the number and distribution of particles in an EAS is needed to properly reconstruct the energy of the primary particle. Furthermore, the number of Cherenkov photons emitted by a relativistic particle in the atmosphere is very large. As a result, the detected Cherenkov light is not subject to large Poissonian fluctuations. This means that any fluctuations detected by IACTs are caused

by the fluctuation of the actual physical process that take place within the shower, or fluctuations in the background. As a result, IACTs can not only be used to directly measure cosmic ray sources, but they can also be used to directly measure the physics at work within an EAS.

The primary disadvantage IACTs have in detecting EAS arises from the combination of the requirement for the telescope to be pointed at a source, and the extremely small duty cycle of IACTs. Because PMTs are so sensitive to light, IACTs can only be operated on moonless nights, resulting in a yearly duty cycle of approximately 10%. IACT experiments must monitor the atmosphere for aerosol content in order to properly reconstruct a detected EAS from data. As a result, IACTs are only effective on clear nights. IACTs must also be pointed at a specific location on the sky because Cherenkov radiation is so highly beamed. In order to properly image a source, the number of detected EAS must exceed the background estimate for that location on the sky or it will appear empty. This makes IACTs ill suited for searching for new cosmic ray sources, and much more adept at precise measurement of known sources.

#### 1.5.2. AIR FLUORESCENCE DETECTORS (FDs).

Fluorescence is the process by which matter (atoms, molecules, etc...) absorbs photons of one wavelength and then emits photons of a second wavelength (usually lower than the first). The absorption of light excites electrons in certain matter into excited states, and after some time these excited electrons relax back down, emitting a photon. When an EAS passes through the atmosphere, photons in the shower excite diatomic nitrogen and nitrogen ions which then fluoresce light with a wavelength between 300 - 400 nm. Unlike Cherenkov light, fluorescent light is emitted isotropically. Air fluorescence Detectors (FDs) do exactly that:

detect the florescent light created by EAS (as well as any Cherenkov light directed at the FD).

fluorescence detectors resemble IACTs, and have a similar segmented concave mirror focusing down to a PMT array. Unlike IACTs, FDs do not need to point, and so to increase coverage on the sky they are made smaller and combined in groups to cover a large area of the sky (it is much less expensive to have several, smaller mirrors then one large mirror). An example of modern FD design can be seen in the Telescope Array experiment, which is located in the high desert of Millard County, Utah, and consists of 3 FD clusters, each containing between 12 and 14 FDs, and a particle detection array (see fig. 1.5).

The primary advantages of FDs is they do not need to have showers aligned along the telescope axis to detect them. As a result of this, FDs can monitor huge volumes of the atmosphere over a large area. This makes FDs ideal for detecting the highest energy cosmic rays, which have the lowest flux on the surface of the earth. In addition, the ability to detect a shower off the longitudinal axis means that FDs can directly measure an EASs longitudinal distribution, which is a good estimator of the primary composition and energy.

The primary disadvantage of FDs is the duty cycle which, like IACTs, is small due to the need for moonless clear nights. This is actually an overestimate for FDs because of the weaker intensity of fluorescence light and the generally larger distances between the detector and the shower as compared to IACTs. This requires FD experiments to monitor the aerosol and dust content of the atmosphere much more strictly than IACT experiments.

### 1.5.3. PARTICLE ARRAYS.

Particle arrays directly detect the shower front of an EAS as it reaches the ground. Such arrays are composed of particle detectors which sample the shower front as it passes through



FIGURE 1.5. The FD cluster located at the Black Rock Mesa site. Photo by John Matthews. Retrieved June 9, 2016 from <https://en.wikipedia.org/wiki/File:BRM-FD-open.jpg> under the Creative Commons Attribution-ShareAlike 3.0 License.

them. By using the geometry of the array, the number of detected particles, and the relative timing as individual detectors are triggered, the shower geometry and other important parameters can be reconstructed.

Unlike FDs and IACTs, particle arrays have a very large duty cycle ( $\approx 100\%$ ) and are able to, technically, survey the entire sky from horizon to zenith all day every day (in reality quality cuts are often applied to remove highly inclined showers). The modular nature of particle arrays also offer a significant advantage. Particle arrays use many more individual detectors than FDs and IACT arrays, which means that the cost an individual particle



FIGURE 1.6. The Tibet Air Shower Array at the Yangbajing site in Tibet. The white boxes contain individual particle detectors. Photo courtesy of Jordan Goodman.

detector is usually low relative to the cost of the experiment. This gives two main advantages. Firstly, particle arrays are easily extensible (that is, they can be expanded gradually, one detector at a time, as funding permits). Secondly, particle arrays are relatively insensitive to the failure of a single detector, which means maintenance and repairs to the array can be performed while the rest of the detector array is functioning.

The primary disadvantage to using particle arrays comes from the fact that shower fronts are only partially sampled at ground level. That is to say, particle arrays can only ever give an incomplete snapshot of an EAS in time. This means that it is sometimes extremely difficult (or even impossible) to reconstruct the primary composition and energy. Almost all information of the longitudinal development, which is heavily dependent on primary

composition and energy, is lost when detected with a particle array, save the few nanoseconds it takes for the front to pass through the ground.

## CHAPTER 2

# THE HIGH ALTITUDE WATER CHERENKOV GAMMA RAY OBSERVATORY

The High Altitude Water Cherenkov (HAWC) Observatory is an EAS particle array designed to study gamma rays in the very high energy regime. HAWC resides on the flanks of the Sierra Negra volcano near Puebla, Mexico, at an altitude of approximately 4,100 meters above sea level. The detector is the successor to the Milagro experiment [20], which was the first water Cherenkov detector to observe TeV gamma ray sources. HAWC has a time integrated field of view of 8.4 sr between  $-26^\circ$  and  $64^\circ$  in declination, and a nearly 100% duty cycle, providing the means to create the deepest survey of the sky in the VHE regime to date. The Observatory is composed of 300 densely packed Water Cherenkov Detectors (WCDs), covering an area of 20,000 m<sup>2</sup>, approximately ten times that of Milagro (see fig 2.1).



FIGURE 2.1. The HAWC Observatory in the final days of construction.

Each WCD consists of a water filled, bladder lined, cylindrical steel tank 7.3 m in diameter and 5 m deep, containing four upward facing photon detectors: three, 8 inch diameter Hamamatsu R5912 PhotoMultiplier Tubes (PMTs) and one central 10 inch high efficiency Hamamatsu R7081 PMT. These PMTs rest at the bottom of each WCD, forming an equilateral triangle with each corner 1.8 m from the central PMT. The dome of each PMT is surrounded by a conic, polypropylene baffle with white interior and black exterior surfaces. These baffles are designed to restrict the field of view of each PMT to only downward traveling light without optically isolating the PMTs. The PMTs themselves are partially sealed within a waterproof container <sup>9</sup>, which houses the base electronics of the PMT and is fed by a single RG-59 cable carrying both the PMT signal and its high voltage supply. The optical isolation of the WCDs allows the detector to better sample the distribution of particles within the front of Extensive Air Showers (EAS). This aspect of HAWC's design greatly improves the angular resolution of the detector when compared to Milagro, and will be discussed in further detail in section 2.1.

The Milagro collaboration performed the deepest, wide field survey of the TeV gamma ray sky to date [21]. HAWC, with its larger detection area and optically isolated WCDs, boasts a 15-fold increase in sensitivity over its predecessor [22](see fig. 2.2). At the time of this writing, HAWC is complete, though most data presented here were taken with the first 250 WCDs.

This chapter will describe HAWC through the perspective of an EAS, from the creation of light in a WCD to the recording of data to a hard disk.

---

<sup>9</sup>The detection surface is directly exposed to water

FIGURE 2.2. The sensitivity of HAWC compared to other TeV astronomy experiments.

### 2.1. WATER CHERENKOV DETECTORS (WCD)

The HAWC observatory is modular, being composed of hundreds of independent water Cherenkov detectors (WCDs). As the name suggests, WCDs are designed to facilitate and detect the Cherenkov radiation emitted as charged particles of an EAS front pass through the water in the WCDs. The optically isolated nature of the WCDs is a relatively new innovation for EAS particle detection arrays, and this aids in the discrimination between  $\gamma$ -ray and hadron induced showers by constraining the location of muons produced by EAS. The construction and design of the WCDs was an iterative process, which began at Los Alamos National Lab and concluded with a working prototype / physics test at Colorado State University (see fig. 2.3).

The outer surface of each WCD is composed of a cylindrical shell of galvanized corrugated steel 7.3 m in diameter and 5 m tall with a ribbed dome roof of military-grade opaque canvas.

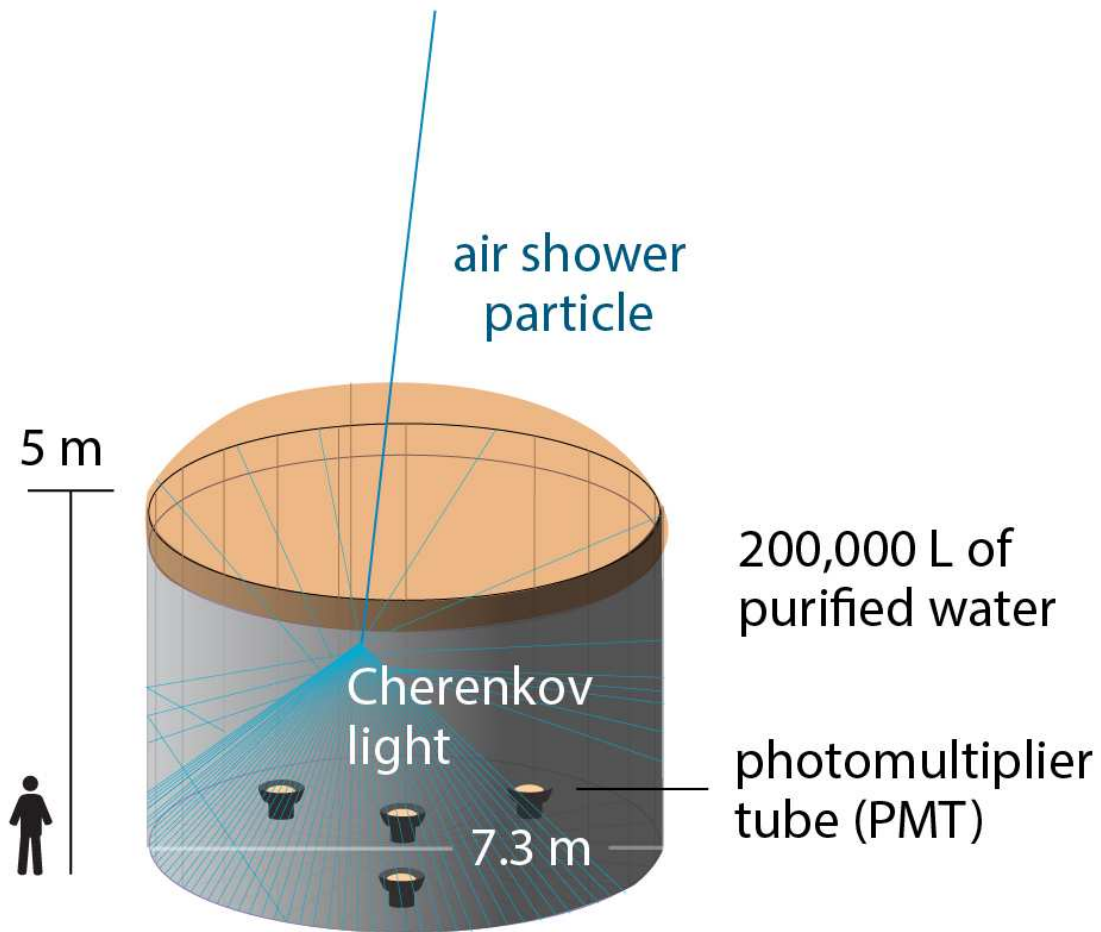


FIGURE 2.3. A Diagram of a single HAWC WCD. Person for scale.

This shell protects a single polypropylene water bladder of similar dimensions. The bladder is photon tight with a black, non reflective interior coating and holds some 200,000 liters of water purified at the sub-micron level. At the top of the bladder is an access hatch and four light tight instrumentation ports which feed the necessary cabling for the depth monitor, temperature monitors, calibration fiber optics, and PMTs. The bottom of the bladder is fitted with four plastic pucks, which secure the PMTs in place relative to the bladder.

The dimensions of the WCDs were chosen to both optimize the sensitivity of HAWC to TeV EAS and to minimize the dependence of the number of detected photoelectrons on the

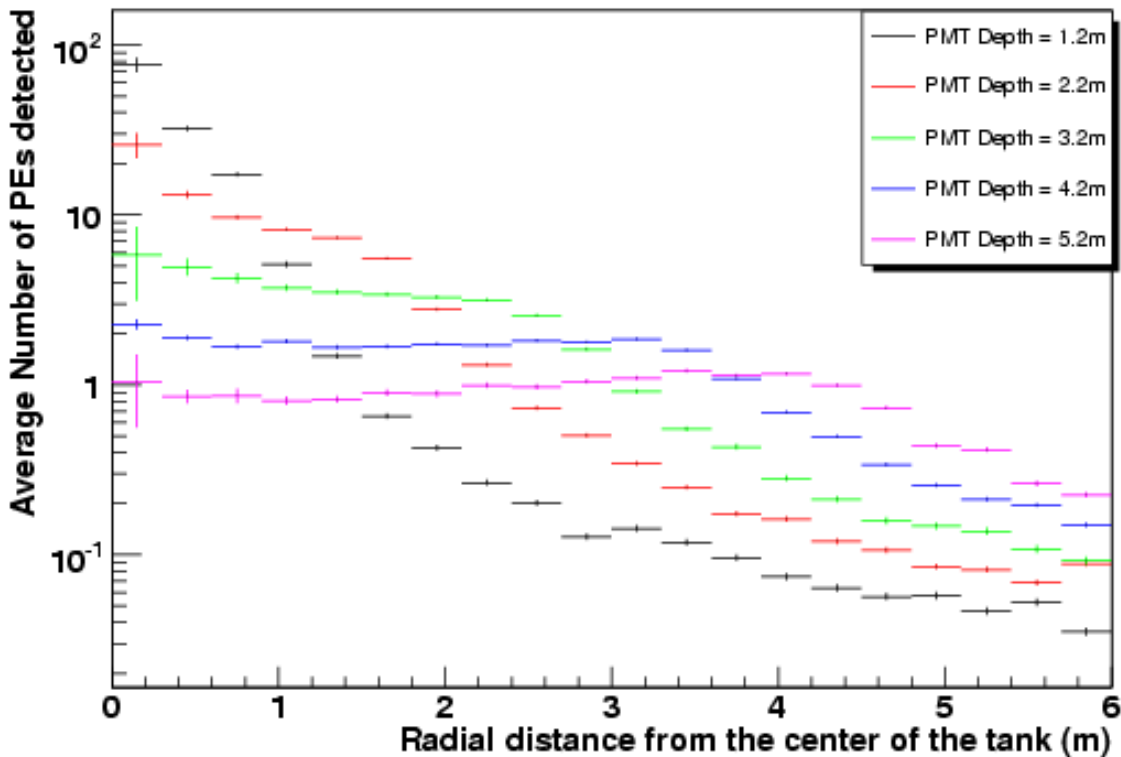


FIGURE 2.4. The average number of PEs detected as the result of a simulated 100 MeV gamma ray, creating a cascade just above a very wide WCD as a function of PMT placement.

location of the PMTs at the bottom of the WCDs. For shallow water depths, low energy secondary particles penetrate all the way to the bottom of the WCD. This causes a large number of PEs to be detected at the PMTs, so every detection by the PMT results in a large signal (every detection looks like an EAS secondary). The depth was chosen to be based on the penetration depth of vertical muons produced by TeV showers (about 10.5 radiation lengths). The width of the WCD was chosen based on the depth, and insures that the PMT response is uniform as a function of radius out to the edge of the WCD (see fig. 2.4). This maximizes the amount of Cherenkov light emitted by the most penetrating charged particles that enter the WCD<sup>10</sup>. The water contained in a WCD is filtered and sterilized

<sup>10</sup>The more water a relativistic charged particle penetrates through, the more Cherenkov light it emits.

such that Cherenkov light has an attenuation length between 7 m-17 m within the WCD. This attenuation is repeatedly tested using a laser and a 100cm glass water-filled tube. It requires approximately 60 million liters of filtered water to fully instrument the HAWC array.

When Cherenkov light from a charged particle reaches the bottom of a WCD it can activate one or more of the four upward facing PhotoMultiplier Tubes, which is the first step in data acquisition.

## 2.2. PHOTO MULTIPLIER TUBES (PMT)

Photomultiplier tubes are a class of extremely sensitive, high gain vacuum phototubes specifically designed to detect a range of the EM spectrum. These devices are sensitive enough to detect single photons, and comprise the core detection instrumentation for many modern particle astrophysics experiments. Every PMT consists of two primary components: the photocathode (see fig. 2.5) and the electron multiplier dynode chain (see fig. 2.6).

The photocathode consists of a thin metallic film, coating the interior of the glass PMT dome. This layer converts incident light into photoelectrons (PEs) by means of the photoelectric effect. The maximum kinetic energy of PEs produced at the photocathode is given by

$$(14) \quad K_{max} = hf - W,$$

where  $h$  is Plank's constant,  $f$  is the frequency of the incident photon, and  $W$  is the work function of the photocathode. The work function describes the minimum energy required to remove a single electron from the surface of the photocathode. It depends both on the electrostatic potential of the cathode, and the physical properties of the cathode material.

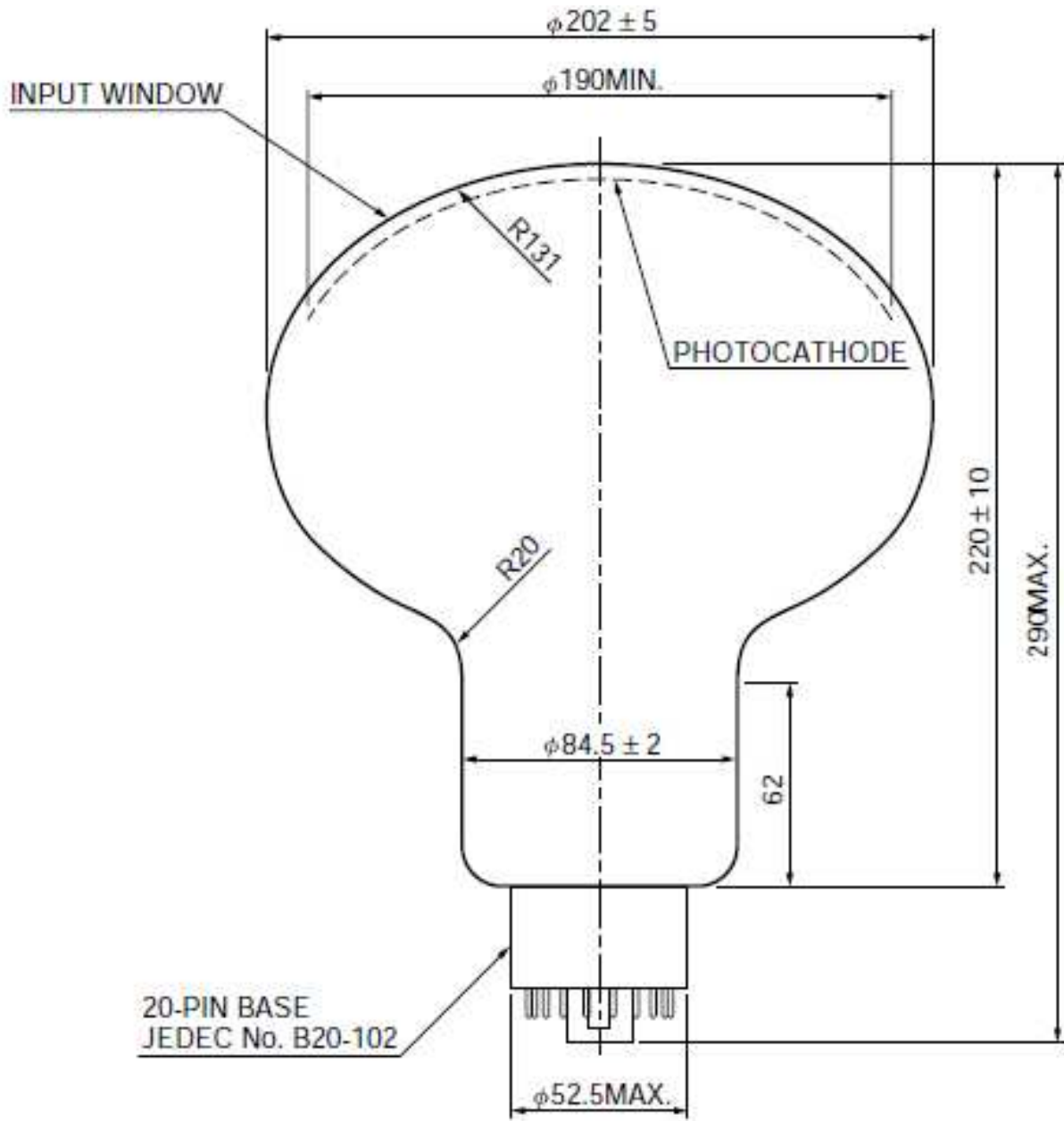


FIGURE 2.5. The R5912 Hamamatsu PMT used for HAWC. All units are in mm unless otherwise noted (image from the Hamamatsu R5912 PMT data sheet).

It is extremely difficult to detect the resulting single electron photocurrent, so this current must be amplified before it can be used.

The electron multiplier is the second primary component of the PMT, and it is responsible for increasing the photocurrent to the point where it can be read out by standard equipment.

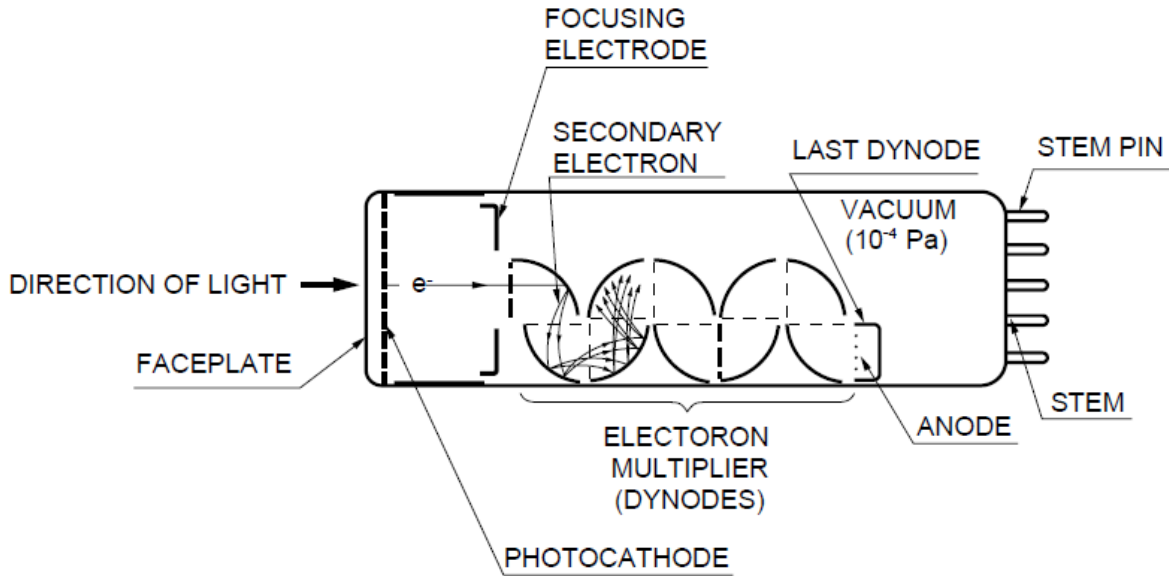


FIGURE 2.6. Basic schematic of a Hamamatsu flat faced PMT which illustrates the dynodes and the motion of secondary emission electrons. Retrieved on June 3, 2016 from <http://www.hamamatsu.com/jp/en/technology/innovation/photocathode/index.html>

It consists of a series of interleaved metallic plates called dynodes, each of which is held at a successively higher positive potential with respect to the photocathode. Photoelectrons produced at the cathode accelerate towards the first dynode, gaining kinetic energy. When they impinge on the first dynode they produce additional electrons through a process known as secondary emission (see fig. 2.6). These then accelerate towards the next dynode, gaining energy and producing additional electrons upon collision, and so on until the cascade of electrons reaches the base of the PMT. By this time, the current has increased several orders of magnitude, and is now easily measurable. There is a direct relationship between the number of the incident photons and the integrated charge of the final current. This means that if a PMT is properly characterized, it can be used to count photoelectrons by making measurements on the resulting current pulse.

Each WCD in HAWC is instrumented with four PMTs. Three of these are 8 inch diameter Hamamatsu R5912 SEL PMTs, which have been refurbished from Milagro for use in HAWC. These form an equilateral triangle at the bottom of a given WCD, with corners 1.8 m from the center. In the center of this triangle rests a single, upward facing, 10 inch Hamamatsu R7081 high efficiency PMT. These PMTs have been purchased new specifically for HAWC, and increase the sensitivity of HAWC to lower energies. PMTs are subject to many different types of noise and by having multiple PMTs in a single tank these effects can be reduced by comparing the signals between PMTs. The most prominent sources of noise in PMTs are dark currents, prepulsing, and afterpulsing.

Dark current is noise that originates from currents traveling through the electron multiplier when the PMT is not being exposed to light. The nature of PMTs requires the use of materials that have low work functions for both the photocathode and dynodes. As a result, these materials are prone to the thermionic emission of electrons. The current density of these emissions within a PMT is heavily dependent on the temperature and (to a somewhat lesser extent) on the age of the PMT<sup>11</sup>. This is an important consideration in HAWC as the majority of the PMTs deployed in the array are refurbished.

Prepulsing is noise that appears as a smaller secondary pulse which precedes the larger, primary pulse. This is the result of a particle penetrating the PMT housing at the photocathode, and stopping at some depth within the electron multiplier. When this particle passes through the photocathode, it deposits enough energy to create the initial photoelectrons of the primary pulse. The initial charged particle then stops at some depth in the electron multiplier ahead of the primary cascade, and creates a secondary cascade. The secondary

---

<sup>11</sup>Most likely as a result of the degradation of the vacuum within the PMT

cascade reaches the base first, but has not been fully amplified because it did not travel the entire length of the electron multiplier. This is then followed by the primary pulse.

Afterpulsing is noise that appears as a smaller secondary pulse which follows the larger, primary pulse. This is the result of electrons ionizing trace gaseous elements within the PMT. When a photoelectron is emitted by the cathode, there is a small probability it will interact with, and ionize, trace atmospheric gases within the PMT. This heavy cation then accelerates in the opposite direction of the electron, back towards the photocathode. When it collides with the photocathode or part of the dynode chain, additional photoelectrons are produced, which then proceed down the electron multiplier in the usual fashion.

Signals produced by the PMTs in a HAWC WCD travel via a cable system out the top of the bladder, over the edge of the corrugated steel tank and down into the ground where they are routed to the counting house, which is at the center of the array and contains all of HAWCs processing electronics.

### 2.3. ELECTRONICS

Each 8 inch PMT in HAWC generates pulses at a rate of approximately 20 kHz from a combination of dark noise, real EAS particles, and other effects . Suppose that this rate holds for all the central PMTs as well (it is much lower than the true rate of the central PMTs). If we were being conservative with our memory and wanted to digitize these pulses with an ADC into 10 time bins with a resolution of 4 bytes each (a long integer), then the full HAWC observatory would generate approximately 320 Mbps of raw data. This is a little over 10 petabytes per year, or 2.7 Libraries of Congress per day <sup>12</sup>. The LHC clocks in at about 25 petabytes per year, and motivated the creation of the worldwide LHC computing

---

<sup>12</sup>see Peter Lyman, Hal R. Varian (2000-10-18). “How Much Information?”. Retrieved 2011-11-29 from <http://groups.ischool.berkeley.edu/archive/how-much-info/>

grid, an intranet consisting of over 170 computing centers in 36 different countries. Suffice it to say, direct digitization of PMT pulses is out of the question for HAWC. Many of the electronic systems employed by the observatory were recycled from Milagro, and so they have been engineered to help solve this data volume problem. As a result, each WCD in HAWC yields less than 50 kB/s of raw data (about one Library of Congress per week).

The first stop a PMT signal has before making it to disk is the analog Front End Board (FEB), also recycled from Milagro. The analog board provides high voltage to PMTs within a set of 4 WCDs (16 channels) and also separates the high frequency PMT signals from the high voltage provided by the board. Once the analog signals are picked off of the high voltage, they are processed into digital square waves before continuing on to the next step in processing. Analog pulses from the PMTs are split, and passed through a low gain (1x) and a high gain (7x) amplifier. The low gain signal is then passed through a “high” discriminator, while the high gain signal is passed through the “low” discriminator. Every time one of these pulses passes the threshold defined by each discriminator, a digital edge is generated. The resulting square pulses from each threshold have a duration equal to the time the analog pulse spent over the threshold specified by the given discriminator.

These digital signals from the analog boards are passed via a custom back end to the digital FEBs. The digital FEBs combine the digital signals from the analog FEB to create a stream of digital pulses, colloquially known as “hits”, which characterize the shape of the analog PMT pulse. This technique is known as Time Over Threshold (TOT) digitization and, for this experiment, is the chosen alternative to full pulse digitization with FADCs. The digital board multiplexes the pulses from each threshold via an exclusive OR, resulting in two-edge and four-edge hits. Two edge hit (one square pulse) are formed when a PMT pulse crosses the first threshold but not the second. A four edge hit (two square pulses separated

by a gap in the signal) occurs when the PMT pulse crosses both thresholds. This section of the FEB also provides triggering and monitoring information (the trigger is a remnant of the multiplicity trigger in Milagro). From here, the TOT hits are passed to the Time to Digital Converters (TDCs), which convert the time of each edge into binary, which is then written to disk. The TDCs have a minimum time resolution of 0.1 ns, and so some reshaping is done when the digital time pulses are multiplexed together, in order to insure that the difference in time between two edges in a hit are not less than the resolution of the TDCs.

At this point, the Extensive Air Shower has been successfully digitized to hard disk, and from here online and offline reconstruction begins. HAWC does not employ any form of electronic multiplicity trigger. All hits are written to disk, and these hits are either combined into events or discarded as noise through software techniques.

#### 2.4. ONLINE PROCESSING: EDGE FINDING

An example stream of post TDC edges can be seen in figure 2.7. The individual edges in a four-edge hit are labeled consecutively as  $t_0$ ,  $t_1$ ,  $t_2$ , and  $t_3$ . Time differences are labeled with two numbers,

$$(15) \quad t_{01} = t_1 - t_0$$

$$(16) \quad t_{12} = t_2 - t_1$$

$$(17) \quad t_{23} = t_3 - t_2$$

$$(18) \quad t_{03} = t_3 - t_0.$$

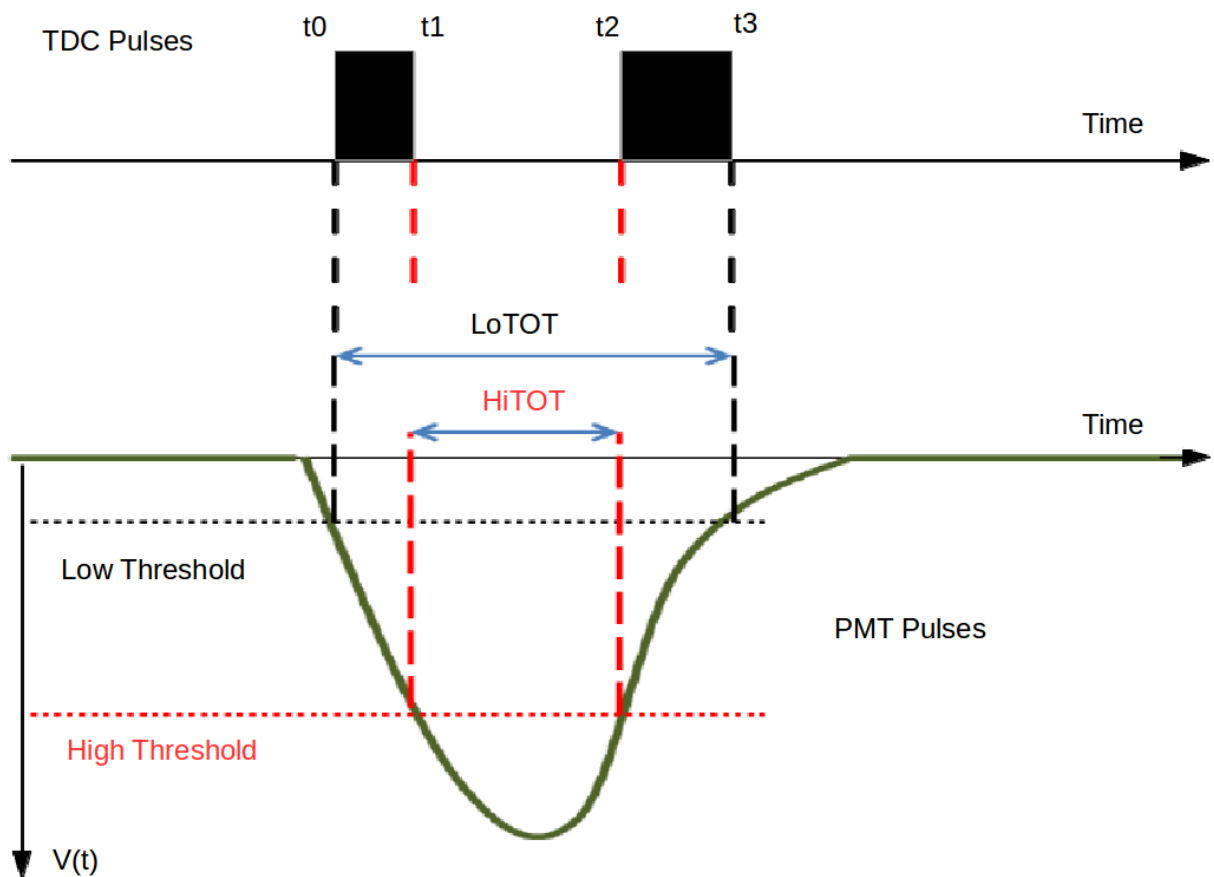


FIGURE 2.7. An example of the post TDC data stream and the resulting edge times.

The time  $t_{01}$  is representative of the time it takes the PMT pulse to rise to some maximum value (small  $t_{01}$  indicates a short rise time). The time  $t_{23}$  is representative of the time it takes the PMT pulse to return to zero (small  $t_{23}$  indicates a short fall time). The times  $t_{03}$  and  $t_{12}$  represent the time the pulse spends over the low threshold (LoTOT) and high threshold (HiTOT) respectively. Because of this, they are related to the number of photoelectrons produced by the PMT which generated the pulse.

Consider four square pulses (8 edges) streaming out of a TDC. Which edges belong to a two edge event (a PMT pulse that only crossed the low threshold) and which edges belong to a four edge event? The method used for answering this question is known as edge finding. The edge finding process discriminates between two-edge and four-edge events by applying

a set of statistical cuts to the data stream as it is produced. These cuts are determined by pulling a sample of raw edge data from the stream, which is simply a series of time values. First, a period of at least  $10 \mu\text{s}$  of silence is found within the stream, which marks the beginning of the edge finding analysis. After this period, consecutive sets of edges are arbitrarily grouped into two-edge and four-edge hits, and the resulting HiTOT and LoTOT values are examined as a 2D histogram (see fig. 2.8).

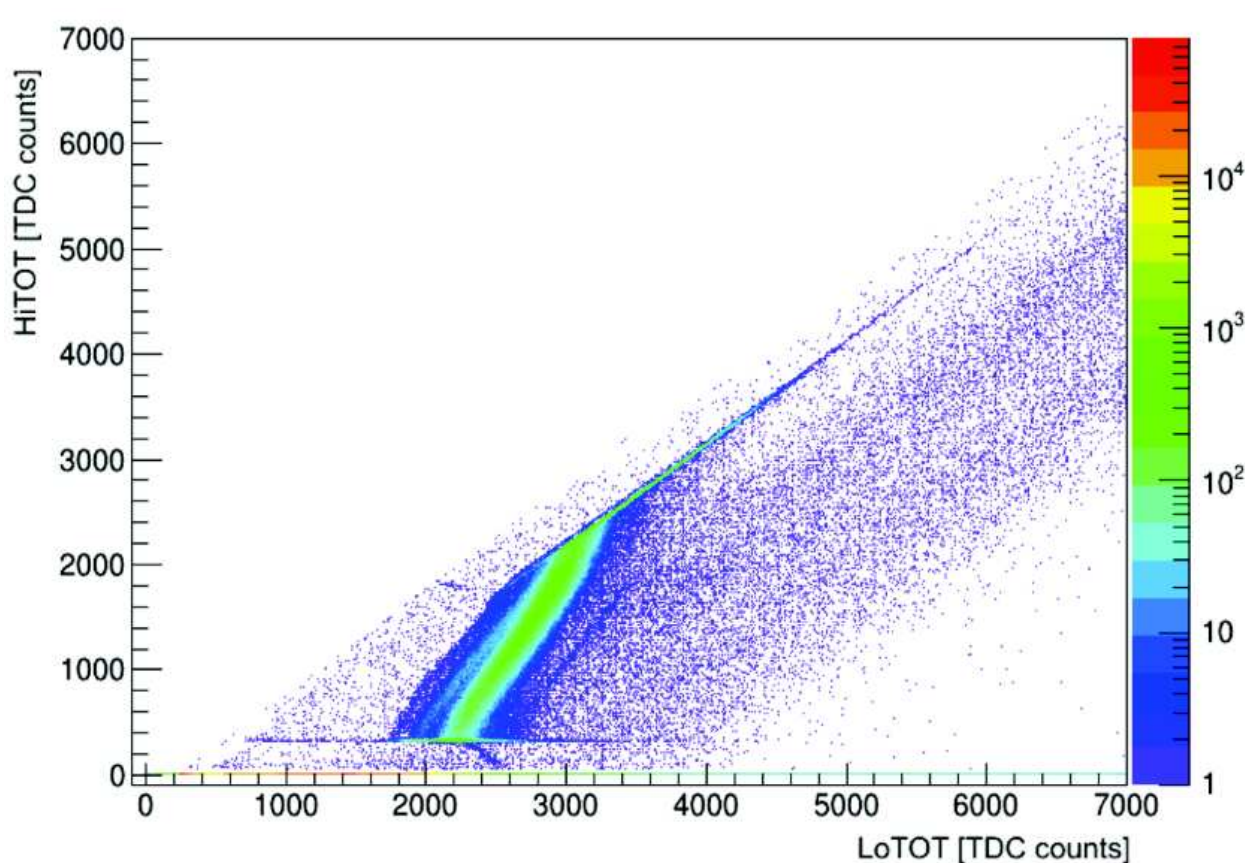


FIGURE 2.8. The result of arbitrarily pairing edges from the TDC data stream. Courtesy of Joshua Wood.

The random pairings of edges will result in two superimposed distributions. The first is a relatively uniform distribution resulting from pairs of real two-edge sets being considered as four-edge hits. Because these sets are physically two-edge hits, they can land anywhere in HiTOT-LoTOT space that is permissible by the electronics, creating a flat haze of random

hits. The second distribution is the result of real four-edge sets being correctly grouped as a four-edge hit. In this case, HiTOT and LoTOT are physically related because they come from the same analog PMT pulse. These real four-edge hits must therefore land within the region of HiTOT-LoTOT space permissible by the physics governing PMTs, creating a uniquely shaped region with much higher statistics. The bounds of this region are then used to define a set of linear cuts in TOT space. Once these cuts are defined, then any set of hits falling within the cut region are considered to be a four-edge hit, otherwise it is a pair of two-edge hits (see fig. 2.9).

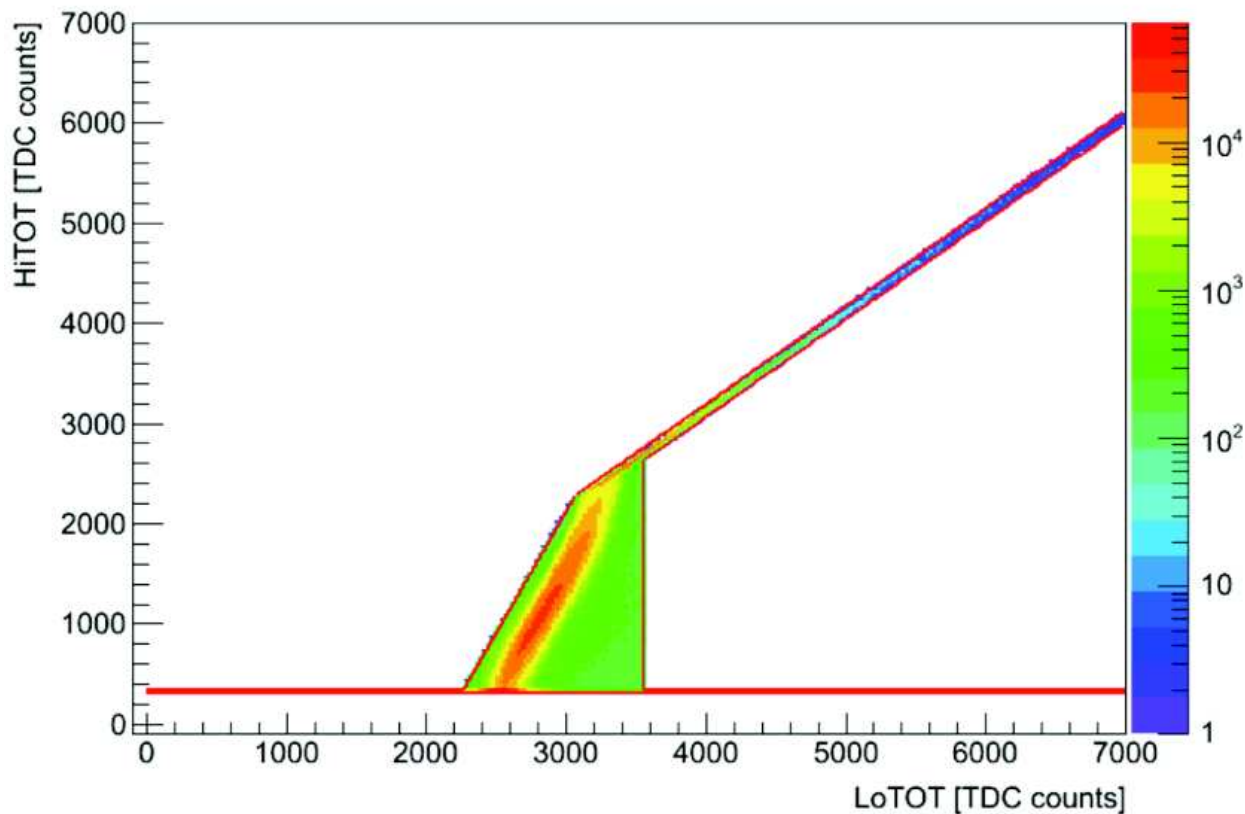


FIGURE 2.9. Example cuts for defining four-edge events. Courtesy of Joshua Wood.

The statistical nature of this process means that some four-edge hits are misclassified two-edge pairs. This process is known as PE promotion because PMTs with promoted hits are reconstructed as having produced more PEs. This effect has been deeply studied by the

HAWC collaboration and it has been determined that PE promotion only occurs about 0.4% of the time (that is, about 0.4% of four-edge hits are actually pairs of two-edge hits in disguise [23]). The presence of PE promoted hits in the data is almost entirely removed via a process known as edge refining. Similar to edge finding, a stream of edges is arbitrarily grouped into four-edge sets, and the resulting TOT values are used to determine the location of real hits within some TOT space and define a cut for future use. In edge refining the relationship between  $t_{01}$  (the time between the first and second edges) and HiTOT is examined (see fig. 2.10). Physical hits will exhibit slewing, meaning that smaller hits (smaller HiTOT) have a longer rise time than larger hits (larger HiTOT). Again, the slewing region is identified and any previously classified four-edge hit that falls outside of this slewing region is reclassified as a set of two-edge hits.

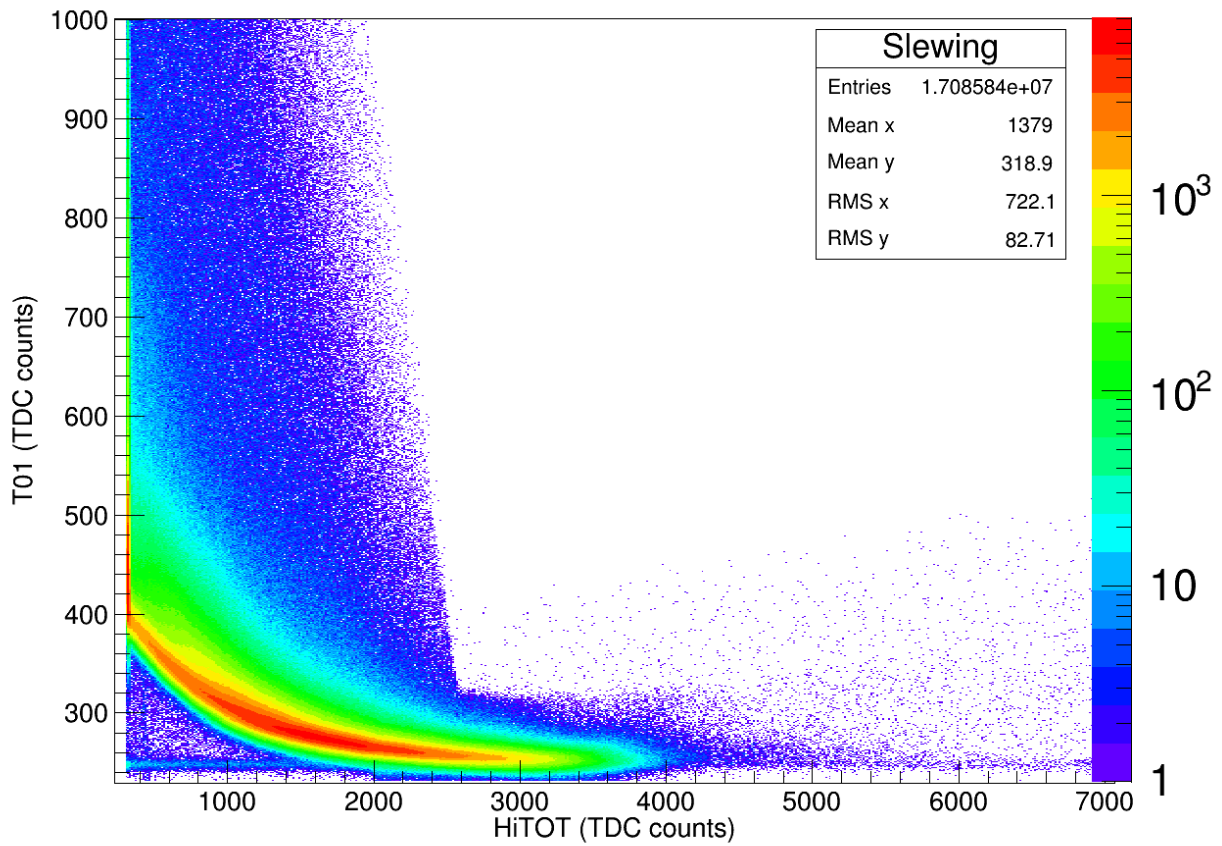


FIGURE 2.10. The presence of charge slewing in  $t_{01}$ -HiTOT space. The sharp edges are present because this is post edge refinement. These data are considered to be real four-edge hits.

## CHAPTER 3

# OFFLINE RECONSTRUCTION

At this point, the raw data are complete. Individual PMT hits have been grouped into events containing the individual HiTOT, LoTOT, hit times, and PMT IDs for every hit in the event. These data still need to be cleaned (remove faulty channels, ignore PEs that fall below or above some calibration threshold, etc...), but that is done on a per-reconstruction basis. The goal now is to use geometric, timing, and intensity information to determine the trajectory of the primary particle and locate its origin on the sky.

### 3.1. CALIBRATION

The goal of any calibration system is to translate raw recorded data into meaningful information. For HAWC, this means converting TOT values into some number of PEs, and converting the time stamp on each hit into the time at which each PMT was hit. These two translations are known as the charge and slewing calibration respectively, and both rely on examining the detector response to a controlled amount of light released into the WCD array. The system begins with a 532 nm wavelength laser that pulses at a given repetition rate through an optical fiber. The light is split along two paths; one to a radiometer to measure the energy of each pulse, and the other to a series of filter wheels. The filter wheels attenuate the light to some chosen level, before it is split again to be measured by a second radiometer. The remaining light travels along the fiber optics through a series of switches and splitters until it finally makes it to one of the calibration diffusers that are contained in every tank. From here the light is split one last time. Part of the light is sent back to the calibration house in order to record the time of flight while the remainder travels downward through the WCD until it impinges on the photocathode of any of the four upward facing

PMTs in each WCD. This system allows for the injection of a known quantity of light, which in turn allows for the measurement of the detector response to a controlled signal. The goal of the calibration procedure is to relate the measured PMT response to the number of photoelectrons produced at the photocathode of a PMT. This is done by relating the probability of a PMT producing photoelectrons to the intensity of the light released into a WCD.

The probability of a photocathode producing  $n$  PEs from a single light pulse is governed by the Poisson distribution about a mean PE value of  $\lambda$

$$(19) \quad P(n, \lambda) = \frac{\lambda^n}{n!} e^{-\lambda}.$$

Because the laser light is pulsed at a known rate, the hits which result from light pulses can be isolated using a time cut. In the ideal case this sample only contains hits that resulted from the laser light entering the WCD. All of these hits represent the presence of some number of PEs greater than zero. When the number of PEs produced is small (the low intensity regime) the ratio of the number of measured hits to the number of injected laser pulses is the probability of the photocathode producing  $n > 0$  PEs when said light pulse is expected to produce  $\lambda$ .

$$(20) \quad \eta = \frac{signal}{trigger} = P(n > 0, \lambda = \langle nPE \rangle).$$

Here,  $\eta$  is known as the occupancy. The probability of seeing some number of PEs and not seeing any PEs must sum to 1. Therefore,

$$(21) \quad \eta = 1 - P(n = 0, \lambda = \langle nPE \rangle)$$

$$(22) \quad = 1 - e^{-\langle nPE \rangle}.$$

If all of the hits in the selected laser time window were signal, this would allow for the direct calculation of  $\langle nPE \rangle$  by simply measuring  $\eta_o$ . Unfortunately the cut window is contaminated by random radiation events (stray muons, dark currents, etc...). By measuring the hit rates outside of the sampling window, the number of noise hits *within* the sampling window can be estimated. With an estimation of the number of noise events within the sampling window, the occupancy can be directly calculated as the ratio between the number of laser shots detected, to the number of shots fired. This implies that

$$(23) \quad \eta = \frac{N_{hit} - N_{noise}}{N_{laser} - N_{noise}},$$

where  $N_{hit}$  is the number of hits within the sampling window,  $N_{laser}$  is the number of laser shots fired, and  $N_{noise}$  is the number of unrelated radiation hits within the sampling window. There is some probability that a noise hit will land with the laser shot. That is to say, the PMT will register a hit that is in time with a laser shot, but is actually the result of noise. The  $N_{noise}$  term in the numerator and the denominator accounts for this.

With these two corrections to the occupancy, the expected number of PEs can be calculated to be

$$(24) \quad \langle nPE \rangle = -\ln(1 - \eta).$$

It is important to note that this equation was derived by assuming that the number of PEs present is small and so can be modeled by a Poisson distribution (it is assumed that the occupancy can be directly measured by looking at the ratio of signal to trigger). At low light intensities this is fine as the probability of a light pulse not creating at least 1 PE is non zero. At high light intensities this is no longer true, and every single light pulse will produce multiple PEs at the photocathodes of the WCD PMTs.

In this high intensity regime it is better to assume that the number of photoelectrons at the cathode of a PMT is proportional to the light intensity in the WCD. This implies that there is a linear relationship between  $\langle nPE \rangle$  and the transmittance set at the filter wheels of the calibration system

$$(25) \quad \langle nPE \rangle = -\ln(1 - \eta) = AT + B ,$$

where  $T$  is the transmittance. The transmittance of a medium (in this case the filter wheels) is defined as the ratio of radiant flux after the medium to the radiant flux before the medium. This is calculated to be the ratio of the energy readings from the radiometers before and after the filter wheels:  $I_{ref}$  and  $I$  respectively.

$$(26) \quad \langle nPE \rangle = A(I/I_{ref}) + B .$$

Assuming the calibration laser is stable,  $I_{ref}$  is the maximum laser output, or  $5.3 \times 10^{-8}$  J. A measurement of zero  $\langle nPE \rangle$  should correspond to a transmittance of zero ( $I$  is zero), and so the parameter  $B$  is expected to be zero. If parameter  $B$  is zero, the parameter  $A$  represents the maximum number of PEs that can be produced at the photocathode (when transmittance is 1). By combining equations (26) and (22) together, a new expression for

the occupancy can be obtained.

$$(27) \quad \eta = C[1 - e^{-A(I/I_{ref})+B}]$$

This provides a functional fit to between the measured intensity of the laser after the filter wheels and the measured occupancy. For a given occupancy (that is, for a given laser intensity), this fit can then be used to simulate the distribution of the actual number of PEs, assuming they follow a Poisson distribution with a mean of  $\langle nPE \rangle$ . The PMT response distribution can be simulated and then percentile-matched with the measured distribution in increments of 10% in order to create the calibration curves required to translate hit TOT values into a measure of PEs.

### 3.2. CORE FITTING

The next step in the offline reconstruction is to determine the location of the shower core (detailed in chapter 1). In order to accomplish this, the core position must first be estimated somehow. This is done by simply calculating the Center Of Mass (COM) of the hits located on the array. It should be noted that this estimate restricts the core location to only positions on the HAWC array.

$$(28) \quad \vec{r}_{com} = \frac{\sum \vec{r}_i q_i}{\sum q_i}$$

Where  $r_i$  is the position of the  $i^{th}$  PMT in detector coordinates and  $q_i$  is the number of photoelectrons detected by the  $i^{th}$  PMT. Because this is a center of mass calculation, this initial estimation of the core position can only ever be on the array. In order to get a better estimate of the position of the shower core, the lateral distribution must be fit (detailed in chapter 2). This fit is done via simple  $\chi^2$  minimization using the COM location as the initial

seed (details concerning  $\chi^2$  minimization can be found in chapter 4). For HAWC the lateral distribution is observed as the distribution of particle density as a function of distance from the core. This distribution is described by the Nishimura-Kamata-Greisen (NKG) function,

$$(29) \quad \rho(r, s, N) = \frac{N}{2\pi R_{mol}^2} \frac{\Gamma(4.5 - s)}{\Gamma(s)\Gamma(4.5 - 2s)} \left(\frac{r}{R_{mol}}\right)^{s-2} \left(1 + \frac{r}{R_{mol}}\right)^{s-4.5},$$

where  $r$  is the radius with respect to the core location,  $N$  is an arbitrary amplitude parameter, and  $s$  parameterizes the shower age such that when  $s = 1$  the number of particles in the shower is maximized.  $R_{mol}$  is the Moliere radius [24], which is the radius of a cylinder coaxial to the core containing 90% of the particles generated by the shower. HAWC uses a value for  $R_{mol}$  as 124.21 m, which is a calculated value based on the radiation length of electrons in air, the density at the observed altitude, and the ratio between the electron scattering energy and critical energy. This function was obtained theoretically and requires several rough approximations of electromagnetic cascade theory, but it is still used by HAWC and other projects to describe the LDF of EAS [25] (see fig 3.1).

Once the core is reconstructed, a parameter known as the Core Fiducial Scale (CFS) can be defined. This parameter defines the percentage of the radial distance to the center of the array from where the core lands. A CFS value of 100 indicates that the core has been reconstructed directly on the edge of the array, while a CFS of 0 means that the core was reconstructed at the defined coordinate origin (roughly the center of HAWC). A quality cut of  $CFS < 90$  can be used to insure that all showers are well contained within HAWC. As the energy of the shower increases, the probability of the shower core landing within some area per unit time decreases while it's lateral distribution at the ground increases in area. This means that high energy showers are biased towards being off-array events, and so this CFS cut effectively places an upper limit on the sensitivity of HAWC. This has yet to be studied

by the collaboration as the CFS cut is, at the time of this writing, a recent addition and so was not used in this analysis.

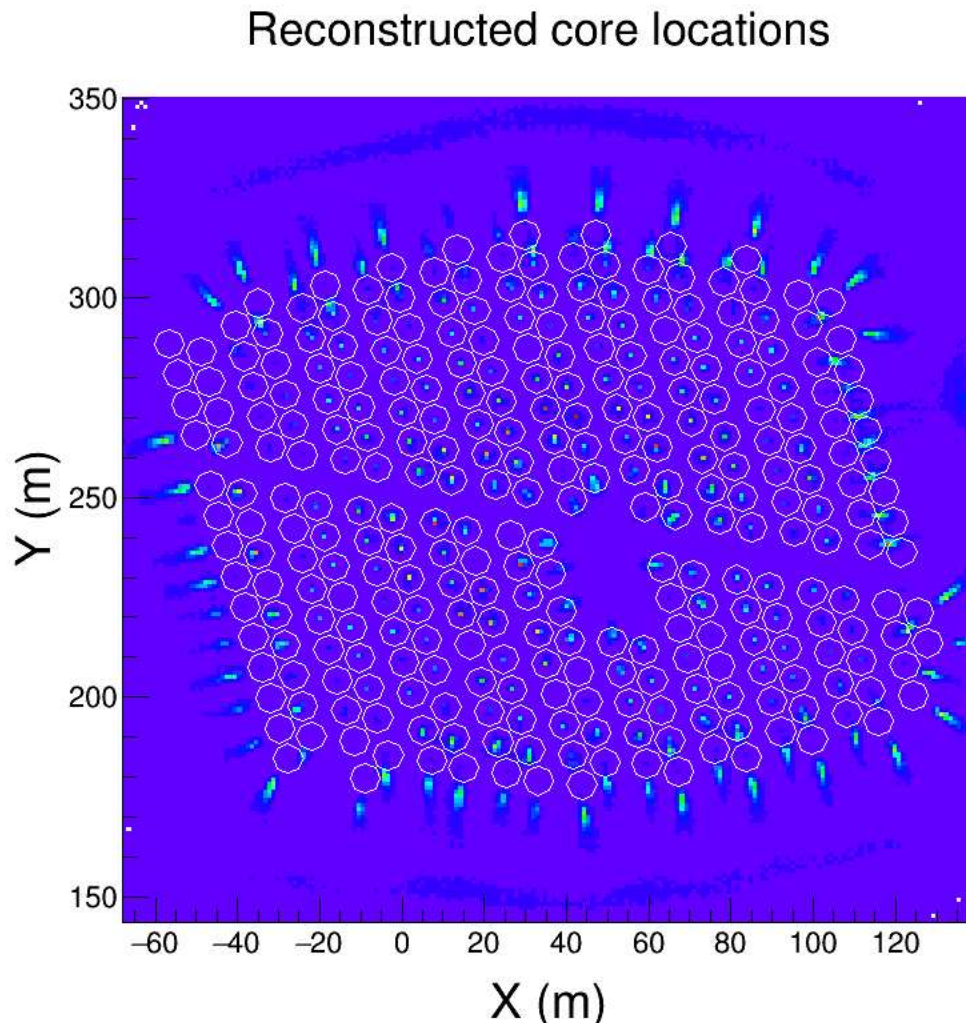


FIGURE 3.1. A histogram of the reconstructed core positions with HAWC over 125 seconds of live time (no cuts). The bright spots represent more events being reconstructed with cores at that location. Near the center of the array the NKG fit tends to place the cores directly on the WCDs. Near the edges of the array, the probability of the core being off of the array increases, and so the reconstructed cores get pulled off of the array.

### 3.3. PLANE AND ANGULAR FITTING

The next step in the reconstruction is fitting the shower front plane. This fit provides information on the trajectory of the primary particle and therefore the location at which it originated on the sky. Fitting the particle trajectory involves minimizing the difference in time between when a PMT was hit and when a PMT was expected to be hit for a shower with some trajectory  $\hat{p}$ . Consider the two dimensional case shown in figure 3.2.

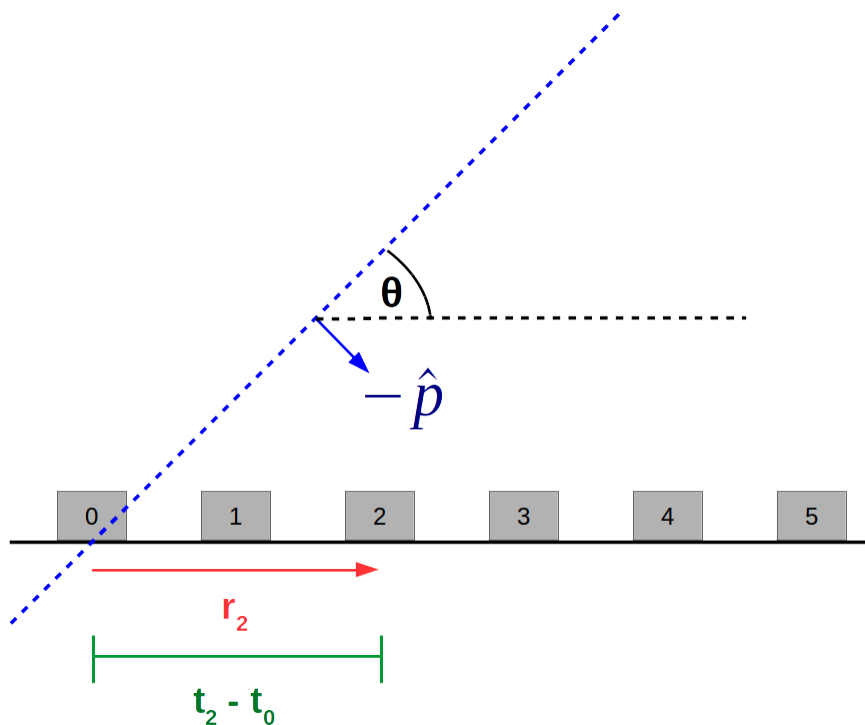


FIGURE 3.2. Schematic of a shower front plane in two dimensions. The gray boxes represent WCDs and the dotted blue line is the shower front plane

The shower front plane moves in the  $-\hat{p}$  direction at a velocity of  $c$ . Detector 0 is triggered at time  $t_0$  and position  $\vec{r}_0$ , detector 1 at time  $t_1$  and position  $\vec{r}_1$  and so on. The difference in time between  $t_0$  and  $t_n$  is known as the residual of detector  $n$ . The time that it would take the shower front plane to trigger detector  $n$  after triggering detector 0 is  $\|\vec{r}_n\|/V_x$  where  $V_x$  is the

velocity of the plane in the x direction and  $\vec{r}_n$  is  $(x_n, y_n, z_n)$ . To fit the plane the difference between these two times must be minimized [26]. This is done via  $\chi^2$  minimization.

$$(30) \quad \chi^2 = \sum_n w_n \left( (t_n - t_0) + \frac{x_n \cos(\theta)}{c} \right)^2 .$$

Here,  $w_n$  is the weight given to the nth detector, and the positive sign comes from the fact that the velocity of the plane is opposite the direction of  $\hat{p}$ . The weight of each detector is based on the number of PEs detected by that specific PMT. In the general, three dimensional case where  $\hat{p} = (i, j, k)$  such that  $i^2 + j^2 + k^2 = 1$  the argument of  $\chi^2$  becomes

$$(31) \quad \chi^2 = \sum_n w_n \left( (t_n - t_0) + \frac{\vec{r}_n \cdot \hat{p}}{c} \right)^2 ,$$

$$(32) \quad = \sum_n w_n (t_n - t_0 + x_n i + y_n j + z_n k)^2 ,$$

where the value of  $c = 1$  is implied. In order for  $\chi^2$  to be an extrema,

$$(33) \quad \frac{\partial \chi^2}{\partial t_0} = 0$$

$$(34) \quad \frac{\partial \chi^2}{\partial i} = 0$$

$$(35) \quad \frac{\partial \chi^2}{\partial j} = 0$$

must be true. The time derivative can be solved explicitly.

$$(36) \quad \frac{\partial \chi^2}{\partial t_0} = 0$$

$$(37) \quad = \sum_n w_n (t_n - t_0 + x_n i + y_n j + z_n k)$$

$$(38) \quad \therefore t_0 \sum_n W_n = \sum_n w_n (t_n + x_n i + y_n j + z_n k) .$$

The form of the  $t_0$  equation suggests the following variables.

$$(39) \quad W = \sum_n w_n$$

$$(40) \quad A_x = \sum_n w_n x_n$$

$$(41) \quad A_{xx} = \sum_n w_n x_n x_n$$

$$(42) \quad A_{xy} = \sum_n w_n x_n y_n$$

⋮

$$(43) \quad t_0 = \frac{A_t}{W} + \frac{iA_x}{W} + \frac{jA_y}{W} + \frac{kA_z}{W} .$$

The partials in  $i$  and  $j$  are also straight forward. In both cases the substitution  $k = \sqrt{1 - i^2 - j^2}$  must be used because the system only has three degrees of freedom.

$$(44) \quad \frac{\partial \chi^2}{\partial i} = 0$$

$$(45) \quad = \sum_n w_n (t_n - t_0 + x_n i + y_n j + z_n k) \left( x_n + z_n \frac{\partial \sqrt{1 - i^2 - j^2}}{\partial i} \right)$$

$$(46) \quad = \sum_n w_n (t_n - t_0 + x_n i + y_n j + z_n k) \left( x_n + z_n \frac{i}{k} \right)$$

$$(47) \quad \begin{aligned} \therefore A_{xt} - t_0 \left( \frac{i}{k} A_z - A_x \right) + i(A_{xx} - A_{zz}) + jA_{xy} \\ + \left( k - \frac{i^2}{k} \right) A_{xz} - \frac{ij}{k} A_{yz} + \frac{i}{k} A_{zt} = 0 . \end{aligned}$$

And similarly,

$$(48) \quad A_{yt} - t_0 \left( \frac{j}{k} A_z - A_y \right) + j(A_{yy} - A_{zz}) + iA_{xy} \\ + \left( k - \frac{j^2}{k} \right) A_{yz} - \frac{ij}{k} A_{xz} + \frac{j}{k} A_{zt} = 0 .$$

Substituting  $t_o$  from equation 43 into equations 47 and 49 produces two equations of three unknowns

$$(49) \quad i \left( B_{xx} - B_{zz} - \frac{i}{k} B_{xz} - \frac{B_{zt}}{k} \right) + j \left( B_{xy} - \frac{i}{k} B_{yz} \right) + (B_{xt} + kB_{xz}) = 0$$

$$(50) \quad j \left( B_{yy} - B_{zz} - \frac{j}{k} B_{yz} - \frac{B_{zt}}{k} \right) + i \left( B_{xy} - \frac{j}{k} B_{xz} \right) + (B_{yt} + kB_{yz}) = 0$$

where

$$(51) \quad B_{mn} = A_{mn} - \frac{A_m A_n}{W} .$$

By first assuming  $\theta$  is small (so  $k \approx 1$ ), these equations become linear and an exact solution for  $k$  can be found. This can then be plugged into the original set of equations to find solutions for  $i$  and  $j$ . By repeating these steps the components of the best fit shower front plane approach that which minimizes  $\chi^2$ . This assumes that the  $W_n$  values chosen for each detector in the array is correct. In reality, some of the hits detected by a PMT may not be from the shower front. The arrival time residuals of hits which belong to the shower front plane should be Gaussian. By fitting the time residual distribution to a Gaussian, hits from outside the shower front plane can be removed. This effectively changes the  $W_n$  for each PMT. This iterative fitting method is extremely fast and after only a few cycles, the

zenith angle  $\theta$  changes by less than  $0.0001^\circ$ . This shower front plane can now be used at the seed to a likelihood fit.

Likelihood fitting is an effective procedure for determining the parameters that best fit some model to a given data set. Suppose there is a data set  $x$  consisting of  $x_1, x_2, x_3, \dots, x_n$  independent observation of some physical phenomena (say, the EAS time residuals of  $n$  PMTs in a particle detector array like HAWC). These observations can effectively be thought of being pulled from an unknown distribution with some probability density function  $f(\mathbf{X})$  where  $\mathbf{X}$  is some vector of parameters needed to define  $f$ . For example, if  $f$  were a Gaussian distribution,  $\mathbf{X}$  would represent a specific mean and standard deviation of  $f$ . For a chosen set of parameters  $\mathbf{X}$ , the probability of drawing  $x_1$  from the distribution  $f(\mathbf{X})$  is written as  $f(x_1|\mathbf{X})$ . The joint probability of drawing  $x_2$  given  $x_1$  would be  $f(x_1, x_2|\mathbf{X}) = f(x_1|\mathbf{X}) \times f(x_2|\mathbf{X})$ . It follows then that the joint probability of drawing the set  $x$  is then

$$(52) \quad \mathcal{L}(x|\mathbf{X}) = \prod_{i=1}^n f(x_i|\mathbf{X}),$$

where  $\mathcal{L}$  is known as the likelihood. The unique set of parameters  $\mathbf{X}_o$  that maximizes  $\mathcal{L}$  are therefore those parameters that would most likely produce the observed data set  $x$ . The analytical fit to the shower plane is used to set the initial estimates on the parameters used to calculate the likelihood, which significantly reduces the parameter space which must be searched to maximize  $\mathcal{L}$ .

## CHAPTER 4

# SIMULATION

The most basic form of the scientific method is to create some hypothesis, test it against observation, and then modify the hypothesis to match the observations. In particle astrophysics this hypothesis takes the form of intricate simulations of both the physical interactions taking place and the detector itself. If the disagreement between the behavior of the simulated detector and the real detector can be minimized, then the presence of a disagreement between the observed data and the simulation is indicative of unaccounted, or possibly new physics.

### 4.1. CORSIKA

The simulations used for this analysis begin with CORSIKA (Cosmic ray simulations for Kascade) [27]. CORSIKA is a program that produces detailed Monte Carlo simulations of extensive air showers initiated by a wide variety of cosmic ray primaries, including photons and protons, respectively the principle signal and background for HAWC. Originally written in 1989, CORSIKA is a conglomeration of FORTRAN code designed to handle everything from individual particle interactions to atmospheric modeling. Much of the code was written specifically for CORSIKA, but some of it (particle interaction models) was written to be utilized by any simulation suite.

CORSIKA showers are created by simulating in discrete time steps referred to here as cycles. Each cycle can be thought of as being divided into two distinct phases: interaction and propagation<sup>13</sup>. Each of these phases occurs for every particle in the EAS, including

---

<sup>13</sup>This description is dramatically oversimplified, but a full discussion of CORSIKA is beyond the scope of this thesis

Cherenkov and fluorescent photons. At the end of a cycle, the simulated EAS has effectively been propagated through time by some small amount  $dt$ .

The interaction phase of a CORSIKA cycle invokes some form of interaction model based on user input and the particle currently being targeted by the simulation. CORSIKA recognizes 52 unique particles including photons, leptons, selected baryons and antibaryons, resonant states, and nuclei up to  $A=56$ . There are eight interaction models available to CORSIKA: these are VENUS [28], QGSJET [29], DPMJET [30], SIBYLL [31], GHEISHA [32], FLUKA [33], UrQMD [34], and EGS4 [35]. Each of these models is used for different energy regimes and particle types. VENUS, QGSJET, DPMJET, and SIBYLL are optimized for high energy inelastic hadron interactions, while GHEISHA, FLUKA, and UrQMD are optimized for low energy hadrons. EGS4 is used only for photon and lepton interactions (including any form of bremsstrahlung or Coulomb scattering). For the purposes of this analysis these models can be thought of as functions that accept initial particle IDs, and momenta, and then uses these parameters to draw randomized results (a set of post interaction parameters) from numerical distributions based on experimental data. All of these interaction take place within the atmosphere, and so this must also be characterized with some mathematical model by CORSIKA.

As briefly mentioned in chapter 1, the atmosphere is a highly complex, dynamic, and literally fluid system. With a depth of approximately 17 km at sea level, it would take a vertical cosmic ray about  $56 \mu\text{s}$  to traverse. Because of this timescale, the atmospheric model used in CORSIKA is completely static, as any time dependent variations in density or depth would occur at characteristic times on the scale of hours. The atmosphere of the Earth is modeled by CORSIKA in five layers, with a uniform simplified composition of  $\text{N}_2$  at 78.1%,  $\text{O}_2$  at 21.0%, and Ar at 0.9%. Each layer is characterized by the quantity of mass present

above a specific altitude, known as the mass overburden  $T(h)$ , and is characterized by the equations

$$(53) \quad T(h) = a_i + b_i e^{-h/c_i} \quad i = 1, 2, 3, 4$$

$$(54) \quad T(h) = a_5 - \frac{b_5 h}{c_5} .$$

Here,  $T(h)$  is in units of  $\text{g}/\text{cm}^2$ , while  $a$ ,  $b$ , and  $c$  are chosen constants based on measurements made of the real atmosphere at specific locations on the earth. HAWC uses CORSIKA atmospheric model 22, which is characterized by measurements made at Malargue, Argentina [27]. The constants can be found in table 4.1. CORSIKA, by default, simulates a flat atmosphere. This is a fine approximation as the curvature of the earth is only about 7.84 cm/km. A shower primary with a zenith angle of  $75^\circ$  traverses approximately 10 m more atmosphere under the flat approximation than it would if a realistic curvature were taken into account (remember, zenith angle limit for this analysis is  $65^\circ$ ). CORSIKA can simulate a curved atmosphere using tables of atmospheric depth as a function of angle, but this may significantly increase simulation time, and so a flat atmosphere was used as the difference between the two for this analysis is small.

TABLE 4.1. The parameters for atmospheric model 22. The parameters listed are the exact values used by CORSIKA (hence the significant figures).

Layer #	Altitude $h$ (km)	$a_i(\text{g}/\text{cm}^2)$	$b_i(\text{g}/\text{cm}^2)$	$c_i(\text{cm})$
1	0 to 10.2	-125.11468467	1169.9511302	947742.88769
2	10.2 to 15.1	-14.591235621	1277.6768488	685089.57509
3	15.1 to 35.9	0.93641128677	1493.5303781	609640.01932
4	35.9 to 100.0	$3.2475590985 \times 10^{-4}$	617.9660747	747555.95526
5	> 100	0.01128292	1.	$10^9$

The next step in a single CORSIKA cycle is the propagation phase, where no particles are created or destroyed in the simulation. In this phase the post interaction secondary particles are only moved through the atmosphere. When charged particles translate through a medium, energy deposition occurs whereby some of the energy of secondary particles is given up to the surrounding medium. At high energies (where  $\beta \approx 1$ ) the trajectories of charged secondary particles are largely unaffected. The electromagnetic fields generated by the motion of these particles literally rips electrons away from local atoms in the medium in a process known as ionization, which reduces the energy of the secondary. It is reasonable to assume that the amount of energy lost as a secondary propagates through some tiny path length, is dependent on the charge and relative velocity of the secondary, the local electron density, and the energy required to remove an electron from orbit (for the elements that compose the medium). Indeed, this process was first articulated by Hans Bethe in 1930 and is well described at high energies by,

$$(55) \quad dE = \frac{4\pi n z^2 \lambda}{m_e c^2 \beta^2} \left( \frac{e^2}{4\pi\epsilon_0} \right)^2 \left[ \ln \left( \frac{2m_e c^2 (\gamma^2 - 1)}{U_{atmo}} \right) - \beta^2 \right] ,$$

$$(56) \quad \beta = \frac{v^2}{c^2} ,$$

$$(57) \quad \gamma = (1 - \beta^2)^{-1/2} ,$$

where  $\lambda$  is the thickness of the medium traversed,  $z$  is the charge of the particle,  $v$  is the velocity of the particle,  $n$  is the number density of electrons in the medium,  $m_e$  is the electron mass,  $e$  is the electron charge,  $U_{atmo}$  is the mean excitation potential,  $\epsilon_0$  is the permittivity of free space, and  $c$  is the speed of light. Most of these factors are constant for a medium of

uniform composition. Condensing those constants yields,

$$(58) \quad dE = \frac{\lambda z^2}{\beta^2} \kappa_1 (\ln(\gamma^2 - 1) - \beta^2 + \kappa_2) ,$$

where  $\kappa_1=0.153287 \text{ MeV } g^{-1} \text{ cm}^2$  and  $\kappa_2=9.386417$  (unitless) are derived for dry air using [36]. For a given path length,  $\lambda$ , this expression can be used to compute the ionization energy loss for a single secondary particle. For muons with exceptionally large Lorentz factors ( $\gamma > 2 \times 10^4$ ), additional energy losses occur due to bremsstrahlung and  $e^+e^-$  production. If at the end of a simulation cycle the Lorentz factor drops below threshold, the muon is dropped from these additional calculations.

The propagation phase of each computation cycle also includes calculations concerning the deflection of secondary particles through scattering and through interaction with the magnetic field of the Earth. In both of these cases, the energy of the secondary particle is held constant; only the trajectory is modified. The scattering of charged particles in CORSIKA is considered for both muons and electrons. This process is simplified into the modification of the trajectory of a secondary particle only once per propagation phase. In a real EAS, these particles may scatter multiple times as some path length is traversed, each time resulting in a tiny change in trajectory. In CORSIKA, once a given particle has reached the middle of the propagation path length for a given cycle, the trajectory of that particle is modified by randomly pulling deviation angles from a predefined distribution. This Coulomb multiple scattering distribution is well approximated by a Gaussian, but can also be explicitly calculated by employing Moliere's theory [24].

The final step of the propagation phase involves a process known as statistical thinning. For most showers, it is computationally unreasonable to simulate each and every particle produced in an EAS. This is because computing times for EAS simulations roughly scale

with the primary energy (the number of particles in a shower generally increases with energy). Thinning is the process by which this scaling effect is mitigated for high energy showers. All particles in the simulation except neutrinos that fall below some adjustable fraction of the primary energy ( $\epsilon_{thin} = E/E_0$ ) are subject to this process. At the end of a cycle, if any single particle has an energy less than  $\epsilon_{th}E_0$ , thinning takes place. Each particle for which this is true is assigned a survival probability of

$$(59) \quad p_i = \frac{E_i}{\epsilon_{th}E_0} ,$$

where  $E_i$  is the energy of the  $i^{th}$  particle. Survivors are selected at random based on their probability, and are assigned a weight of  $1/p_i$ . The remaining particles are discarded. In this way, the surviving particles represent more than one secondary in the shower, but only require one particle's worth of computational time.

After thinning occurs, the simulation cycle repeats until the shower front reaches some predefined altitude and the next phase in the simulation can begin.

## 4.2. GEANT4 AND HAWCSIM

At this point the simulation exists as a set of files for each simulated primary type:  $\gamma$  rays, protons, helium, oxygen, silicon, carbon, magnesium, neon, and iron. Each file contains the values of the particle weights, locations, and velocities at the end of the CORSIKA simulation for each shower in the file, 10m above the tops of the HAWC WCDs. These serve as the input to GEANT4, which will propagate the showers through a simulated HAWC array. Like CORSIKA, GEANT4 simulates the motion and interactions of particles but unlike CORSIKA, GEANT4 is specifically designed to handle interaction through multiple media and interfaces. GEANT4 can handle things like the reflection of photons from the

interior of the WCDs and the production of PEs at the photocathode of the PMTs in HAWC. HAWCsim is the specific implementation of the GEANT4 libraries for HAWC. HAWCsim defines all the geometries and variables needed to propagate particles through the WCDs of the HAWC array.

For a single shower post CORSIKA, every particle in that shower is defined by a particle type ID, position, and momentum. From this HAWCsim translates the particles through HAWC in a very similar manner as CORSIKA translates them through the atmosphere, cycling between interaction and propagation. The major change here is that HAWCsim explicitly checks for interaction at the interface between media (between the plastic bladder and water, for example) and changes the propagation behavior after the interface accordingly<sup>14</sup>. The output of HAWCsim contains, among other things, the creation time and energies of every PE created by the interaction between the simulated Cherenkov light within the WCDs and the simulated photocathodes of the HAWC PMTs. Given that information, the electronics output can be determined and from there, the simulation can be reconstructed in the exact same fashion as the data (with the same software).

### 4.3. SWEETS

At this point, the simulation is reconstructed. For the primaries thrown (simulated) by CORSIKA, there are now files containing the final reconstruction of the associated EAS as if they been detected by the real HAWC detector (assuming the simulation is perfect). The challenge is now to use these reconstructed simulations to produce physically meaningful results. EAS are thrown onto the simulated HAWC array in a deliberately non-physical way in order to maximize the effectiveness of the simulation (for example, there is no point in

---

<sup>14</sup>Again, this is dramatically oversimplified. HAWCsim / GEANT4 includes a much wider range of interaction and decay models than CORSIKA does. It is a much more detailed simulation.

wasting CPU time simulating a shower that will not even partially land on the array). In doing so, two biases are introduced to the simulation.

The first bias is in the primary energy. The distribution of primary energies thrown in the simulation takes the form of a power law,  $E^{-2}$ , while in reality the cosmic ray spectrum is most closely approximated by  $E^{-2.7}$ . This means that higher energy events are more frequently simulated than what would be detected in reality<sup>15</sup>. This is done because the behavior of the HAWC observatory must be properly studied at all energies, and a steeper simulated spectrum would increase the rarity of high energy events.

The second bias is in where the showers are thrown on the array as defined by the distance  $r$  from the shower core to the center of HAWC. Physically more events should land at larger  $r$  than smaller  $r$ , simply because there is more area at larger  $r$ . In the simulation, events are thrown such that this distribution goes as  $r^{-1}$ , which throws more events near the center of HAWC than what would be there in reality. Again, this is done on purpose to more effectively study the behavior of HAWC.

In order to get a simulation of a physical source transiting over the array, these biases must first be removed, and then weights must be introduced to change the distributions reflect physicality. This is where the Software for Weighting Events and Event-like Things and Stuff, SWEETS<sup>16</sup>, comes in. Given a source spectrum and a declination, SWEETS reweights the events in a reconstructed simulation to mimic the distributions that would be seen were that source to transit over HAWC. These weights can be calculated analytically as follows.

---

<sup>15</sup>The reason why energy is not thrown uniformly is because of the increase in computation times at high energy.

<sup>16</sup>I feel a great disturbance in the Force, as if millions of lives face palmed and were suddenly silenced.

The throwing biases suggest that the differential distribution,  $T$ , with which events are thrown in CORSIKA has the form of

$$(60) \quad T = T(E, r) = \frac{dN}{dE dA d\Omega} \propto \frac{E^{-2}}{r} .$$

This describes the number of events with an energy between  $E$  and  $E+dE$  that will fall on some tiny patch of area  $dA$  a distance  $r$  from the center of the detector which came from some tiny patch of sky  $d\Omega$ . It is the time independent differential flux artificially created by throwing events with CORSIKA. Integrating this across the phase space must yield the total number of events thrown, such that

$$(61) \quad N_{thrown} = C \int_E \int_A \int_\theta \int_\phi \frac{E^{-2}}{r} \cos(\theta) \sin(\theta) dE dA d\theta d\phi ,$$

where  $C$  represents the proportionality constant of the differential distribution. The form of this integral demands comment. The first comment is that  $\sin(\theta)d\theta d\phi$  is the differential solid angle  $d\Omega$ . The second comment concerns the presence of  $\cos(\theta)$  in the integrand which is present because the incident flux on  $dA$  decreases with increasing zenith angle as a result

of geometry<sup>17</sup>. Affecting the integral results in

$$\begin{aligned}
N_{thrown} &= C \int_{E_i}^{E_f} \int_A \int_{\theta_i}^{\theta_f} \int_0^{2\pi} \frac{E^{-2}}{r} \cos(\theta) \sin(\theta) dE dA d\theta d\phi \\
&= C \pi (\cos^2(\theta_i) - \cos^2(\theta_f)) \int_{E_i}^{E_f} \int_A \frac{E^{-2}}{r} dE dA \\
&= C \pi (\cos^2(\theta_i) - \cos^2(\theta_f)) (E_i^{-1} - E_f^{-1}) \int_A r^{-1} dA \\
&= C \pi (\cos^2(\theta_i) - \cos^2(\theta_f)) (E_i^{-1} - E_f^{-1}) \int_{R_i}^{R_f} \int_0^{2\pi} r dr d\phi' \\
N_{thrown} &= C 2\pi^2 (\cos^2(\theta_i) - \cos^2(\theta_f)) (E_i^{-1} - E_f^{-1}) (R_f - R_i)
\end{aligned}$$

$$(62) \quad \therefore C = \frac{N_{thrown}}{2\pi^2 (\cos^2(\theta_i) - \cos^2(\theta_f)) (E_i^{-1} - E_f^{-1}) (R_f - R_i)} .$$

The ranges for R,  $\theta$ , and E are 0 to 1km, 0 to 75°, and 5 GeV to 2 PeV respectively. The distribution with which events are thrown on the simulated array is now fully defined.

$$(63) \quad T(E, r) = \left( \frac{N_{thrown}}{2\pi^2 (\cos^2(\theta_i) - \cos^2(\theta_f)) (E_i^{-1} - E_f^{-1}) (R_f - R_i)} \right) \left( \frac{E^{-2}}{r} \right) .$$

Note the units on  $T(E, r)$ . The units of differential flux include inverse time, but  $T$  does not. This is because the simulation has no time. The arrival time of simulated showers relative to each other is not simulated. The tricky question is this: how do you reweight the simulation and use it to calculate  $dN/dt$ , the number of events detected per second, for a uniform differential flux described by  $\Phi(E) = \Phi_0 (E/E_0)^{-\gamma}$  where  $\Phi$  has units of inverse area

---

<sup>17</sup>Remember, the differential describes in part the number of events that will fall on some tiny area of the detector. If those events come from a large zenith angle, then this tiny area will appear edge on and no events will be able to fall on it. Basically, with a bit of vector maths it can be shown that for a vector field  $\vec{F}$ , the integral flux through some area defined by normal vector  $\vec{A}$  is  $\int \vec{F} \cdot d\vec{A} = \int F \cos(\theta) dA$ .

time energy? Let  $w$  be some yet to be defined weight function. What is the form of  $w$  such that

$$(64) \quad \frac{dN}{dt} = \int w T(E, r) \cos(\theta) dA d\Omega dE$$

$$(65) \quad = \int \Phi(E) \cos(\theta) dA d\Omega dE ?$$

Assuming both integrals have the same limits, then the form of the weight function must be  $w = \Phi(E)/T(E, r)$  by association, and so

$$(66) \quad w = w(E, r) = \frac{r E^2 \Phi(E)}{N_{thrown}} 2\pi^2 (\cos^2(\theta_i) - \cos^2(\theta_f)) (E_i^{-1} - E_f^{-1}) (R_f - R_i) .$$

It is important to note the units of  $\Phi(E)$  and  $w(E, r)$ . Again, because the relative time between events is not simulated the energy, area, and solid angle units of the differential flux cancel with the units of  $T(E, r)$  leaving the weight in units of Hz, as intended.

This is all well and good on paper, but the simulation is discrete. Given a file, finding the number of events in the file (and therefore the number of showers thrown) is as simple as looping over the file and counting the number of entries. This is similar to carrying out the integration with the weight function  $w = 1$ . The weight function derived above can be used to assign an individual event a new weight other than unity, and finding  $dN/dt$  from the simulation should be approximately equal to summing the weights.

$$(67) \quad \sum_{i=0}^{N_{thrown}} w(E_i, r_i) \approx \frac{dN}{dt} .$$

With the tricky question out of the way, a new question is raised. How do you reweight the simulation and use it to calculate  $dN/dt$ , the number of events detected per second,

for a differential flux described by  $\Phi(E) = \Phi_0(E/E_0)^{-\gamma}$  coming from a specific declination? Calculating  $w$  in this case will be slightly different than in the isotropic case because the location on the sky from which flux originates changes as the source transits. Basically, the zenith and azimuth angles become time dependent, and this dependence must somehow be accounted for with the weight in order for the simulation to be meaningful.

Because the simulation has no time, a good first place to start would be to parameterize the time dependence of a single transit by some other variables, ideally  $\theta$  and  $\phi$ . First, consider the physical case, where the total number of events detected during a single transit can be described by

$$(68) \quad N_{transit} = 2 \int_0^{t_{max}} \int_E \int_A \Phi(E) \cos(\theta(t)) dt dE dA ,$$

where  $t_{max}$  is the time required for the source to rise to its maximum altitude (assuming it rises at  $t=0$ ). Notice that the solid angle dependence of the integral is no longer present. This is because the source is a point, and subtends no solid angle on the sky. The factor of 2 comes from symmetry. If the detector is symmetric in azimuth, a fair assumption for HAWC, then the same number of events will be detected as the sources rises as would be detected as it sets. The transit of the source from horizon to its maximum altitude (or reverse) is single valued in  $\sin(\theta(t))$  and  $\cos(\theta(t))$ . In order to determine the weight by association as done for the isotopic case, reparameterization should be done in terms of  $\sin(\theta)d\theta$ .

$$(69) \quad N_{transit} = 2 \int_\theta \int_E \int_A \Phi(E) \frac{dt}{\sin(\theta)d\theta} \cos(\theta) \sin(\theta) d\theta dE dA ,$$

At this point, the integral does not depend on time, and so it can be compared to the simulation

$$(70) \quad N_{transit} = 2 \int_{\theta} \int_E \int_A \Phi(E) \frac{dt}{\sin(\theta)d\theta} \cos(\theta) \sin(\theta) d\theta dE dA$$

$$(71) \quad = 2\pi \int_{\theta} \int_E \int_A w T(E, r), \cos(\theta)\sin(\theta) d\theta dE dA ,$$

Where the  $\phi$  integral has been carried out. Again, by association, the weight must be

$$(72) \quad w(E, r, \theta) = \frac{1}{\pi} \frac{\Phi(E)}{T(E, r)} \frac{dt}{\sin(\theta)d\theta} .$$

The transit of the source over the detector is completely described by the derivative  $dt/d\theta$ . In order to examine this derivative, we need a conversion between the time independent equatorial coordinate system and the time *dependent* horizontal (also known as local) coordinate system. This conversion is known as the transit function and can be explicitly derived.

The local coordinate system has already been discussed. It describes the location of an object on the sky with respect to zenith ( $\theta$ )<sup>18</sup> and azimuth ( $\phi$ ). The equatorial system is slightly less intuitive because it describes the location of an object on the sky with respect to the celestial sphere, as opposed to some location on the surface of the Earth. The celestial sphere appears to turn coaxially with the rotational north pole of the Earth and the plane that lies normal to this axis is the equatorial plane because it directly intersects the equator of the Earth. A second plane can be defined by the path in which the earth orbits the sun. This path is known as the ecliptic, and it intersects the equatorial plane at exactly two points on the celestial sphere: the vernal and autumnal equinoxes.

---

<sup>18</sup>Altitude can also be used, which is  $\pi/2 - \theta$ . Altitude is the angular altitude of an object as measured from the horizon.

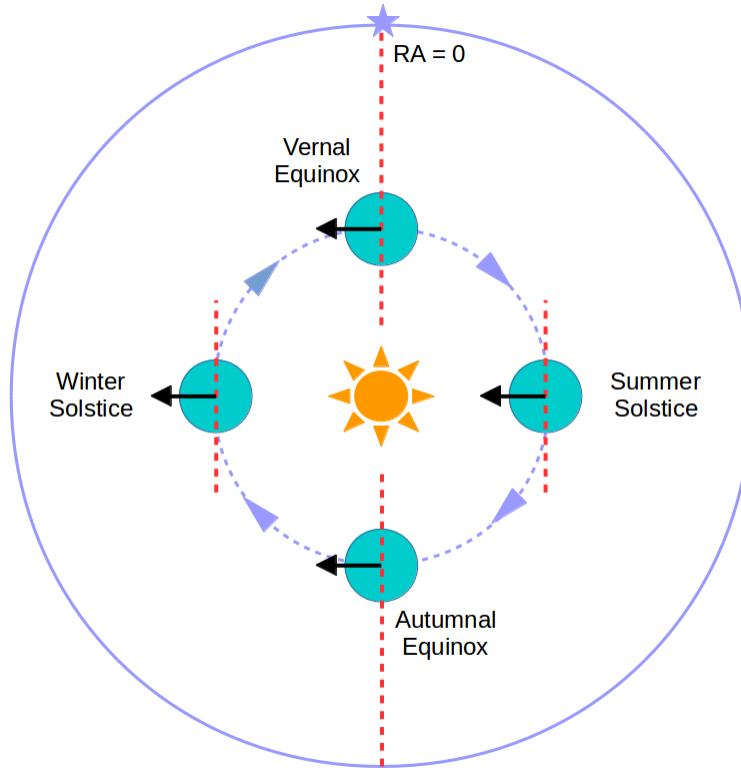


FIGURE 4.1. Schematic showing the definition of the vernal and autumnal equinoxes on the celestial sphere as seen when viewed from above the northern hemisphere of the ecliptic. The dashed red lines represent the intersection between the ecliptic and equatorial planes, while the black arrows represent ecliptic projection of the north rotational pole.

It can be difficult to visualize (see fig. 4.1) but a good way to understand this is to imagine standing anywhere on the equator during the vernal equinox. At that time and place, the vernal equinox is the location on the sky that first rises in the east as the sun sets behind you. The equatorial system defines a fixed point on the celestial sphere by the right ascension (the angular displacement from the vernal equinox) and the declination (the angular displacement from the equatorial plane). Conveniently, because of how the equatorial system is defined, the right ascension of a celestial body is the time required for that object to rise from the horizon after the vernal equinox (known as the local hour angle). With the coordinate systems defined, the transit function can be derived.

Imagine standing at any point on the northern hemisphere as a star transits across the sky. Let  $\hat{C}$  be the unit vector from that point to the star, let  $\hat{Z}$  be the unit vector to the local zenith (straight above you), and let  $\hat{P}$  be a unit vector directed towards the north, parallel to the rotational axis of the Earth (see fig. 4.2). The latitude,  $l$  at this point on the Earth is the angular displacement from the equator along the meridian to that point. Therefore, the angle between  $\hat{Z}$  and  $\hat{P}$  is the difference between the latitude and  $90^\circ$ . The declination,  $\delta$ , of the star is the angular displacement from the equatorial plane to the star, and so the angle between the  $\hat{P}$  and  $\hat{C}$  is the difference between the declination and  $90^\circ$ . The zenith angle of the star is the angular displacement from the zenith to the star, which is the angle between  $\hat{Z}$  and  $\hat{C}$ . These three angular displacements form the highlighted spherical triangle in fig. 4.2

To summarize,

$$(73) \quad \hat{Z} \cdot \hat{C} = \cos(\theta)$$

$$(74) \quad \hat{Z} \cdot \hat{P} = \cos(\pi/2 - l) = \sin(l)$$

$$(75) \quad \hat{P} \cdot \hat{C} = \cos(\pi/2 - \delta) = \sin(\delta) .$$

If the goal is to determine the time dependence of  $\theta$  then the opposite angle, the relative local hour angle  $H$  must be defined (spherical angle  $\angle ZPC$  in fig. 4.2). Again, this is the angle between the meridian plane and the plane containing both  $\hat{P}$  and  $\hat{C}$ . To define  $H$ , we need to define two unit vectors which are both perpendicular to  $\hat{P}$ , one pointing along arc  $PZ$  and one along arc  $PC$ . These vectors are,

$$(76) \quad \hat{V}_\delta = \frac{\hat{C} - \hat{P}(\hat{P} \cdot \hat{C})}{\|\hat{C} - \hat{P}(\hat{P} \cdot \hat{C})\|} = \frac{\hat{C} - \hat{P}(\sin(\delta))}{\cos(\delta)} ,$$

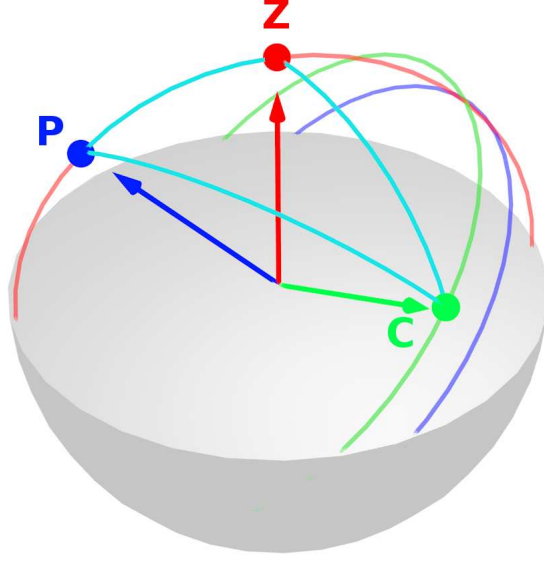


FIGURE 4.2. Schematic showing the relevant geometry of the transit of an object on the celestial sphere in local coordinates. P is the rotational axis of the earth, Z is the local zenith, and C is the transiting object. The associated great circles are the equator (blue), the meridian (red) and the transit path (green). In equatorial coordinates the declination of the object is the angular displacement from the equator to the transit path.

and

$$(77) \quad \hat{V}_l = \frac{\hat{Z} - \hat{P}(\hat{P} \cdot \hat{Z})}{\|\hat{Z} - \hat{P}(\hat{P} \cdot \hat{Z})\|} = \frac{\hat{Z} - \hat{P}(\sin(l))}{\cos(l)},$$

respectively. The cosine of the hour angle is therefore

$$(78) \quad \hat{V}_\delta \cdot \hat{V}_l = \cos(H) = \frac{\cos(\theta) - \sin(l)\sin(\delta)}{\cos(\delta)\cos(l)}.$$

Rearranging this yields the transit function.

$$(79) \quad \cos(\theta) = \sin(l)\sin(\delta) + \cos(\delta)\cos(l)\cos(H).$$

The time dependence of the transit function is expressed in  $H$ , the relative local hour angle. Any point on the celestial sphere will, by definition, return to that location on the sky after one sidereal day. The relative local hour angle is the angular displacement between the initial location of said point and the current location at time  $t$ , and so  $H = 2\pi t/t_{sid}$  where  $t_{sid}$  is the duration of a sidereal day. Because the transit function is defined in terms of  $\cos(\theta)$  changing the variables used to calculate the weight appropriately will clean up the derivatives, and so

$$(80) \quad w(E, r, \theta) = \frac{1}{\pi} \frac{\Phi(E)}{T(E, r)} \frac{dt}{\sin(\theta)d\theta}$$

$$(81) \quad = \frac{-1}{\pi} \frac{\Phi(E)}{T(E, r)} \left( \frac{d \cos(\theta)}{dt} \right)^{-1}$$

$$(82) \quad \therefore w(E, r, \theta) = \frac{\Phi(E) t_{sid}}{2\pi^2 T(E, r) \cos(l) \cos(\delta) \sin(2\pi t/t_{sid})} .$$

Normally these kinds of differential manipulations would require more rigor, but these are known physical quantities and so the derivative  $d\theta/dt$  is simply the ratio between a tiny difference in angle and a tiny difference in time. Note that even though  $t$  is present in the weight, it can be directly calculated by inverting the transit function and using the zenith angle of a given simulated event. Any event with a zenith angle less than the minimum transit zenith of the source is assigned a transit weight of 0.

With the entirety of the universe that matters well defined, the spectrum of the Crab nebula can be discussed.

## CHAPTER 5

### THE CRAB NEBULA

The Crab nebula, the remnant of supernova SN 1054 located 6.5 kly from Earth at an equatorial right ascension of  $83.64^\circ$  and declination of  $22.01^\circ$ , is a source of Very High Energy (VHE) gamma rays. The physical structure of the Crab Nebula consists of an optically luminous shell of gases approximately 11 ly in diameter enveloping a central 33 ms pulsar. The production of gamma rays in the Crab is powered by interactions between the relativistic electron wind produced by the central pulsar and the surrounding nebula. This energetic flow of electrons scatters lower energy synchrotron photons up into the TeV range where they can be observed by HAWC [37]. The Crab nebula is an important VHE gamma ray source because of its stability. While it does occasionally flare [38], it is still widely regarded as stable when observed over the course of months. This makes it an important comparative tool because it can act as a standard candle and reference.

Historically, the Crab Nebula first appeared as a supernova in the skies of 1054 C.E., when it was recorded by Chinese, Middle Eastern, and Native American astronomers. Historical documents from the period describe the event as a “guest star” which was visible, even during the day, for two years before fading from view. Modern observations of the Crab nebula have been made by many different TeV gamma ray experiments including Milagro[39], HESS[40], and Whipple[41], which was the first to observe TeV emissions from the Crab in 1989. The physical properties of the Crab, including its size, expansion rate, and spectrum have been very thoroughly measured since its discovery. The spectral properties of the Crab are often used to characterize experiments, study TeV gamma rays and evaluate related systematic uncertainties. The size of the Crab nebula is significantly smaller than the point

spread function of most ground based TeV observatories, which means it can also be used to calibrate the angular resolution of a detector. This analysis is primarily a study of the spectrum of the Crab nebula with the HAWC observatory, but other sources of interest are also examined.

## 5.1. THE DATA

The data used in this analysis were recorded between August 2, 2013 and January 11, 2016 and are comprised of four parts. The first two parts consists of 181 days of live time ending on March 3, 2014, spanning the construction of the final 16 WCDs leading to the completion of the first 111 WCDs of HAWC (consequently, these data are also referred to as HAWC-111). These parts are known as epoch 1 and epoch 2 (the early and late period of the construction of these 16 WCDs). These two epochs are usually examined together because the only change in the detector between the two is the number of PMTs active in the array. The epoch 1 and epoch 2 data sets exist as one large group of runs which must either be manually separated, or the combined set must be analyzed with appropriate weighting. The third part of the data is known as epochs 1+2 which is simply the combined epoch 1 and 2 data set. Examining the combined set will illustrate how to appropriately weight data that has a fluctuating number of active PMTs<sup>19</sup>, without needing to separate the data sets. The fourth and final part of the data used in this analysis consists of 340 days of live time, ending in January 2016, after the completion of the array and is known as HAWC-SP<sup>20</sup>. This portion of the data was used to determine the spectral properties of the Crab and other sources.

---

<sup>19</sup>Even with a completed detector, the number of PMTs fluctuates slightly with time as a result of maintenance and malfunction.

<sup>20</sup>SP is an acronym for the most recent reconstruction, known as Saucy Platypus.

## 5.2. BINS AND CUTTING VARIABLES

The data used for this analysis were divided into 10 bins defined by the fraction of PMTs triggered in the HAWC array (fHit). Data within each fHit bin were further excluded from this analysis based on quality, probability of being background, and reconstructed location on the sky (see table 5.1). Unless otherwise stated, bins 0 and 1 were excluded from the analysis. At the moment, the purity of events (the relative fraction of real gamma rays to real cosmic rays) in these bins is being studied by the HAWC collaboration. It is suspected that these bins contain mostly cosmic rays, but bin composition was not examined for this analysis. Furthermore, fit spectra do not result in reasonable  $\chi^2$  values on *any* of the examined sources when bins 0 and 1 are included. Strictly speaking, it *is* possible that this is evidence that the tested models do not fit the data, but given that HAWC is still young and the Crab is so well characterized as a standard candle, it is more likely that the quality of the data in bins 0 and 1 is poor. In the future, when the detector is better understood and the signal-background selection methods are improved, this will probably change. For now this simply means that the results of this analysis only apply at energies well above 800 GeV.

This section will describe these cutting variables while the following sections will describe how these variables are used in the creation of skymaps for this analysis, and the systematic uncertainties associated with these variables.

### 5.2.1. FHIT AND ENERGY.

HAWC is, at its most fundamental level, a calorimeter. When an extensive air shower front passes through the array, it deposits energy into the WCDs and this is, essentially, what gets recorded as data. EAS array experiments such as Milagro and HAWC, which make no measurement of the shower before it reaches the ground, are only able to directly measure

TABLE 5.1. Cuts used for this analysis of the Crab Nebula with HAWC.

Bin #	fHit >	fHit $\leq$	Angular Bin (degrees)	Compactness >	PINC <
0	0.045	0.067	1.06	21.0	1.50
1	0.067	0.105	0.84	7.0	2.20
2	0.105	0.162	0.65	9.0	3.0
3	0.162	0.247	0.52	11.0	2.30
4	0.247	0.357	0.41	15.0	1.90
5	0.357	0.485	0.35	18.0	1.90
6	0.485	0.618	0.33	17.0	1.70
7	0.618	0.740	0.25	15.0	1.80
8	0.740	0.840	0.23	15.0	1.80
9	0.840	1.00	0.20	3.0	1.60

the energy that arrives at the ground. Unfortunately, an EAS primary of a given energy that interacts at a shallow atmospheric depth will deliver significantly more energy at the ground than one with the same energy that interacted deeper. This implies that the correlation between the energy at the ground and the energy at the first interaction is very weak (if it exists at all). Most ground based EAS experiments define some calculated variable that strongly correlates with primary energy that can be used as a proxy. Analysis bins are then defined with respect to this energy proxy variable.

Regardless of these facts, it is not necessary to determine the primary energy of individual showers in order to measure the spectrum of TeV gamma rays emitted by a source (as discussed in section 5.6). The fraction of PMTs in HAWC that are triggered by an EAS, known as fHit, is used as the energy proxy for this analysis. As expected, fHit correlates weakly with energy, as can be see in fig. 5.1.

Because fHit serves as the energy proxy in this analysis, the fHit bins were specifically chosen such that the mean simulated energy of the bins were evenly separated across  $\log_{10}(\text{energy})$  space.

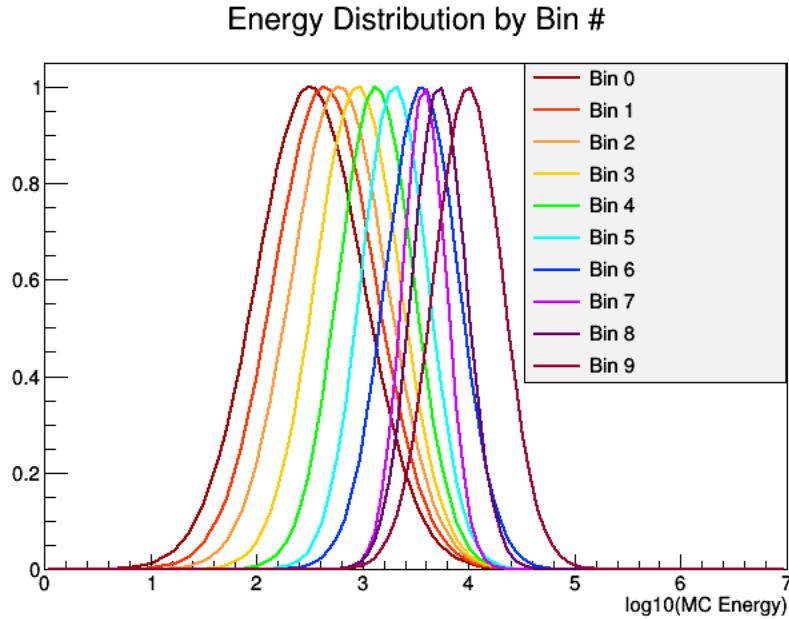


FIGURE 5.1. The distribution of simulated energy in units of  $\log_{10}(E/\text{GeV})$  for HAWC-111.

### 5.2.2. ANGULAR BIN.

The angular bin defines the radius about a given location on the sky within which events are accepted into the analysis. The optimal angular bin size is that which maximizes the statistical significance of a given source and it is a function of the angular resolution of HAWC.

A good estimation of statistical significance for any counting measurement governed by the Poisson distribution is

$$(83) \quad \text{Significance} = \frac{\text{Excess}}{\sqrt{\text{Background}}} ,$$

where the background is the number of counts assuming the null hypothesis, and the excess is the number of counts above or below the background. In this case, the statistical significance is explicitly the number of standard deviations a given measurement is away from a Poisson background.

Consider a circular angular bin of radius  $R$  degrees. If the background is isotropic, then the number of background events that come from that circular bin is proportional to the area of that bin,

$$(84) \quad \text{Background} \propto \pi R^2 .$$

If there is a source in a certain bin, then the number of excess events is dependent on intensity of the source and the angular uncertainty of reconstructed events in the associated fHit bin, which is expressed as the point spread function (PSF). This function defines the likelihood of reconstructing an event on the sky at a location other than where it originated. To first order, the PSF of HAWC is a radially symmetric Gaussian distribution, which is coaxial with the circular bin used to calculate the background. The total excess in a given bin is then the integral of the PSF over the circular bin.

$$(85) \quad \text{Excess} = \int_0^{2\pi} \int_0^R A e^{-\frac{r^2}{2\sigma^2}} r \, dr \, d\theta = 2\pi\sigma^2 A (1 - e^{-\frac{R^2}{2\sigma^2}}) ,$$

where  $A$  is a constant that accounts for the intensity of the source and  $\sigma$  is the angular uncertainty of reconstructed events in this fHit bin. The significance is then,

$$(86) \quad \text{Significance} = \frac{A\sigma^2}{R} (1 - e^{-\frac{R^2}{2\sigma^2}}) ,$$

where the constants have been absorbed into A. If R is written in units of  $\sigma$  this becomes

$$(87) \quad \text{Significance} = \frac{\sigma}{R} \left(1 - e^{-\frac{R^2}{2}}\right),$$

which peaks at  $1.58\sigma$  (see figure 5.2). This implies that the angular bin which optimizes the significance is 1.58 times the reconstructed angular uncertainty in that bin. Ideally this would mean that finding the optimal bin is simply a matter of measuring the angular uncertainty of the HAWC detector. To second order, the PSF of HAWC is not a single radially symmetric

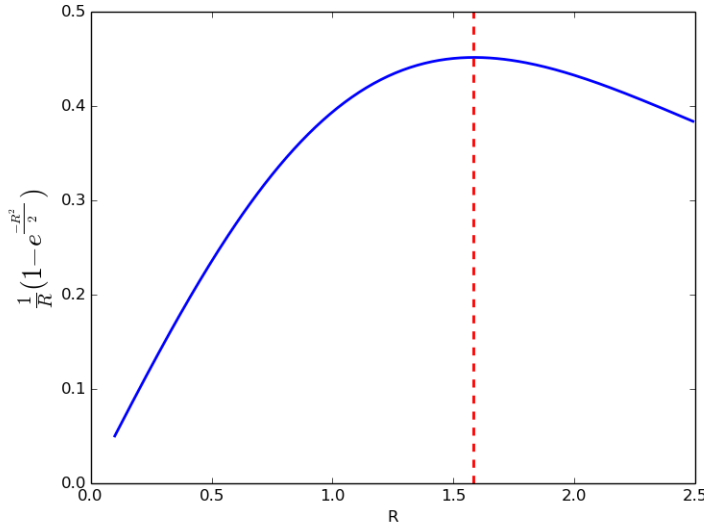


FIGURE 5.2. Significance as a function of bin radius in units of angular uncertainty. The vertical line is the maximum at  $1.58\sigma$ .

Gaussian. It is in fact most closely approximated by the sum of two Gaussians.

$$(88) \quad \text{PSF}(A, r, \sigma_1, \sigma_2) = Ae^{-r^2/2\sigma_1^2} + (1 - A)e^{-r^2/2\sigma_2^2}.$$

The  $1.58\sigma$  approximation serves fine as a first step, but the true PSF of HAWC must be accounted for. Determining the optimal bin size can be carried out in the same fashion

as for a single Gaussian: derive an expression for the significance of a source on isotropic background, and maximize for the bin radius.

The total signal from a source in a radial bin  $R$  is now

$$(89) \quad \text{Excess} = \int_0^{2\pi} \int_0^R \left[ A e^{-r^2/2\sigma_1^2} + (1-A) e^{-r^2/2\sigma_2^2} \right] r dr d\theta ,$$

and the background still goes as  $R^2$ . The significance of the source is then

$$(90) \quad \text{Significance} = C \left[ \frac{A\sigma_1^2}{R} (1 - e^{-R^2/2\sigma_1^2}) + \frac{(1-A)\sigma_2^2}{R} (1 - e^{-R^2/2\sigma_2^2}) \right] ,$$

where the integration constants have been absorbed into  $C$ . This can be simplified somewhat by changing the units such that  $R \rightarrow R\sigma_1$  and  $\sigma_2 = \eta\sigma_1$ . Taking a derivative with respect to  $R$  and setting the result equal to zero results in

$$(91) \quad 0 = A \left( 1 + \frac{1}{R^2} \right) e^{-R^2/2} - \frac{A}{R^2} + (1-A)\eta^2 \left( \frac{1}{\eta^2} + \frac{1}{R^2} \right) e^{-R^2/2\eta^2} - \frac{(1-A)\eta^2}{R^2} ,$$

which is transcendental. An approximate solution can be found by expanding the exponential terms to second order.

$$(92) \quad e^{-R^2/2\eta^2} = 1 - \frac{R^2}{2\eta^2} + \frac{R^4}{8\eta^4} - \dots$$

$$(93) \quad \therefore 0 = \left( \frac{A(\eta^4 - 1) + 1}{8\eta^4} \right) R^4 - \left( \frac{3A(\eta^2 - 1) + 3}{8\eta^2} \right) R^2 + \frac{1}{2} .$$

The above expression is quadratic in  $R^2$  and can be explicitly solved with the quadratic equation, resulting in complex roots on the domain of  $A = [0, 1]$  and  $\eta = [1, +\infty)$ . The real

part of these roots are identical, and is explicitly

$$(94) \quad \text{RE}(R) = \frac{3}{2}\eta^2 \left( \frac{A(\eta^2 - 1) + 1}{A(\eta^4 - 1) + 1} \right) .$$

Note that the real parts of the roots do not solve the quadratic in  $R^2$ , however, they do provide reasonable optimal bins with a measurable systematic. The optimal bins can therefore be found by fitting the distribution of angular uncertainty in MC to a double Gaussian, determining  $\eta$ , and then simply calculating the optimal bin. The optimal bin can also be found numerically by finding the maximum value of the integral of the angular uncertainty distribution in units of  $1/R$  (see table 5.2). The analytical bins were chosen for this analysis for two reasons. First, the analytical angular bins are not limited by the arbitrarily chosen bin width used to discretize the angular uncertainty distribution into a histogram (in this case, 0.025 degrees). Second, the analytical bins are less influenced the presence of statistical fluctuation in the simulation sample.

TABLE 5.2. Comparing the analytical optimal bin to the numerical solution. The values  $A$ ,  $\sigma_1^2$ ,  $\sigma_2^2$ , and  $\eta$  are found by fitting the angular uncertainty in MC to a double Gaussian.

Bin #	A	$\sigma_1^2$	$\sigma_2^2$	$\eta^2$	Analytical Bin (deg)	Numerical Bin (deg)
0	0.929	0.492	1.669	3.387	1.06	1.275
1	0.983	0.319	3.366	10.519	0.84	0.775
2	0.993	0.189	2.883	15.239	0.65	0.575
3	0.995	0.121	2.236	18.452	0.52	0.425
4	0.997	0.0783	1.899	24.249	0.41	0.325
5	0.998	0.0553	1.519	27.448	0.35	0.275
6	0.996	0.0506	0.990	19.557	0.33	0.275
7	0.995	0.0278	0.467	16.821	0.25	0.175
8	0.990	0.0237	0.280	11.814	0.23	0.125
9	0.980	0.0181	0.161	8.900	0.20	0.125

### 5.2.3. COMPACTNESS.

The events used in this analysis are those which have passed a set of cuts to distinguish gamma rays from cosmic rays. That is to say, the background is made only of events that appear gamma-like (the background exists because this cutting method is far from perfect, and cosmic rays vastly outnumber gamma rays). One of the parameters used to do this is known as the compactness, which is a measure of how compact a given shower is about its longitudinal axis. Compactness is calculated by examining muon-like signals occurring far from the core of an extensive air shower. Gamma ray showers primarily produce muons through photonuclear reactions that lead to pions, or through pair production high in the atmosphere [42], and so the muon content in gamma showers is small in comparison to cosmic ray showers simply because there are significantly fewer production channels in a gamma ray shower. The muons produced in a gamma ray shower will fall much closer to the shower core in comparison to a cosmic ray shower. This is because the electromagnetic cascade products (pair produced electrons and bremsstrahlung photons) do not, on average, gain the large transverse momenta often seen from hadrons emerging from typical production reactions. As a result, gamma ray and cosmic ray EAS have significantly different spatial structures. Gamma ray showers are simply more compact than cosmic ray showers (see fig. 5.3).

The signature used to calculate compactness appears in the data as PMTs with very large signals, as would be produced by muons. Cosmic ray showers are therefore discriminated by examining the ratio of the total number of PMTs triggered in an event to the number of PEs measured in the PMT with the largest signal outside 40m from the reconstructed core.

$$(95) \quad \text{Compactness} = \frac{n_{\text{Hit}}}{C_{\text{xPE40}}}$$

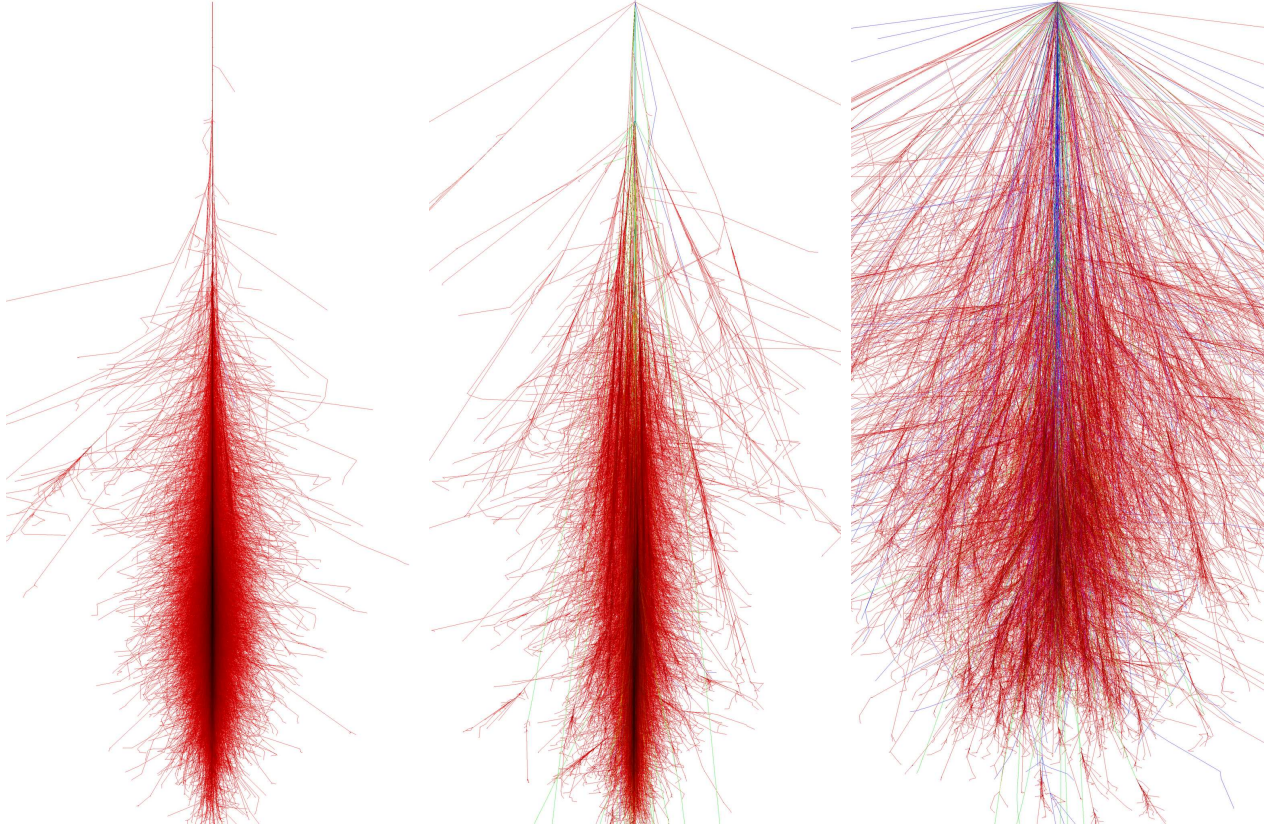


FIGURE 5.3. Example CORSIKA shower simulations for (from left to right) a 1 TeV photon, proton, and iron nucleus. Compiled by Fabian Schmidt, University of Leeds, UK.

Here,  $n_{\text{Hit}}$  is the total number of PMTs in the recorded event and  $C_{\text{xPE40}}$  is the number of photoelectrons recorded from the hottest PMT outside a 40m radius around the shower core. A large compactness value is more gamma-like. The cut values on compactness used for this analysis were determined by maximizing the significance on a simulated Crab nebula as a function of the cut value.

#### 5.2.4. PINCNESS.

The Parameter for Identifying Nuclear Cosmic rays (PINC) is the the second parameter used to separate gamma-like showers from hadron-like showers. As discussed in previous chapters, the lateral distribution of PEs in a single HAWC event is fit to the NKG distribution in order to reconstruct the shower core location. The lateral distributions of hadron induced EAS

have characteristically larger  $\chi^2$  when fit to the NKG distribution, and a good first thought might be to cut on this  $\chi^2$  to separate gammas from hadrons (after all, the NKG distribution is technically only defined for electromagnetic cascades). Unfortunately, if a shower lands partially off of the HAWC array or even if there are significant fluctuations in the shower front,  $\chi^2$  may increase. There are many variables which could lead to a gamma ray shower having a hadron like  $\chi^2$  from the core fit. PINCness takes this idea to the next level and compensates for these issues.

PINCness assumes that gamma ray EAS are axially symmetric and radially smooth. This is a fair assumption as the other gamma hadron separator, compactness, specifically targets LDF asymmetries in hadron showers. If a shower displays axial symmetry and radial smoothness then the charge measured at a given PMT some distance  $R$  meters from the shower core should be close to the mean charge of all PMTs at that radius. Here the definition of closeness is the  $\chi^2$  deviation of that PMT from the mean of all PMTs at  $R$  meters. Naturally, a first attempt definition of PINCness is

$$(96) \quad P = \frac{1}{N} \sum_{i=0}^N \frac{(q_i - \bar{q}_i)^2}{\sigma_i^2},$$

where  $N$  is the number of PMTs in the event,  $q_i$  is the measured number of PEs in PMT  $i$ ,  $\bar{q}_i$  is the mean number of PEs measured by all PMTs within an annular region of  $R = R_i \pm 5$  m<sup>21</sup>, and  $\sigma_i$  uncertainty in the effective charge as defined by the calibration. This is a great first definition and works fine on paper and in practice, but slight modifications to this calculation have recently lead to a new version of PINC (aptly named PINCness version 2). Because the distribution of possible PE counts in an event is very wide (1 to 1000 or more), PINC

---

<sup>21</sup>The location of PMTs in the array is a discrete variable, and so an annular region is needed to choose PMTs “at the same radius”.

is actually calculated using the log of the number of measured PEs. The uncertainty,  $\sigma_1$ , is calculated using a functional form that was derived based on past observations of gamma ray like events with HAWC. The uncertainty reported by the calibration only describes the uncertainty in the measurement, and does not account for the statistical uncertainty arising from fluctuations inherent in all EAS. If the symmetry and smoothness assumptions used for gamma ray showers are consistent with observations, and if the uncertainties are properly defined, then PINC should be 1 for gamma ray showers, and hadron showers will be "more PINC" than gamma ray showers. As a result of this, typical cut values for PINC version 2 range from 1 to 2.

Like compactness, PINCness was optimized by choosing cut values that maximize the significance of a simulated Crab nebula.

Now that the data and all of the analysis variables have been discussed, the first step in the analysis can be examined, which is the creation of skymaps.

### 5.3. SKYMAPS AND THE BACKGROUND

Reconstructed event data include the location on the sky from which a given event originated. These locations form a two dimensional histogram known as a skymap. Skymaps are created with uniform bins of  $0.1^\circ$  characteristic dimension using the HEALPix library, and cover HAWCs field of view (approximately 8.4 sr, or 2 sr instantaneous). All events are recorded in the J2000 coordinate epoch, and for each analysis bin (these bins are of the energy proxy variable, fHit, discussed in 5.2.1) two maps are created: a signal map and a background map. The signal map contains the measured number of events on the sky while the background map contains the expected number of background events. Because the relative excess between signal (TeV gamma rays) and background (cosmic rays) is very small,

the background must be estimated both precisely and accurately or real signal excesses will be indistinguishable from statistical fluctuations.

The background is estimated through a method known as Milagro Direct Integration (MDI)[39]. The goal of MDI is to create a background skymap,  $B(\alpha, \delta)$ , in bins of right ascension  $\alpha$  and declination  $\delta$ , which can then be subtracted from the raw signal skymap,  $S(\alpha, \delta)$  to produce a single map of event excesses. Hadronic cosmic rays form the principle background for all measurements made with HAWC. At the TeV energy scale, it is assumed that they arrive at the earth in an isotropic distribution because they are created by distant sources, and so must propagate through the magnetic field of the galaxy. Cosmic rays in the TeV energy range are completely scrambled by this field and cannot be used to point back to their source. As a result of this diffuse propagation the hadronic background is steady in time, and carries enough energy to not be effected by solar activity. Thus, the observed background is only sensitive to variations in the detector and atmosphere [39].

The background rate in *local* coordinates is denoted by  $F(t, h, \delta)$  where  $t$  is the sidereal time,  $h$  is the hour angle, and  $\delta$  is the declination. Because of the isotropic, diffuse nature of the hadronic background,  $F$  is separable.

$$(97) \quad F(t, h, \delta) = R(t)\epsilon(h, \delta)$$

Here,  $R(t)$  is the all-sky event rate and  $\epsilon(h, \delta)$  is the local angular distribution of events. This implies that even large changes in  $R(t)$  do not affect the local angular distribution of events. Furthermore, it implies that the local angular distribution is a constant with respect to time. As a result, each of these terms can be directly measured using the same data. Once  $R$  and  $\epsilon$  are measured, the background map,  $B(\alpha, \delta)$ , can be calculated.

To calculate  $B(\alpha, \delta)$  an integration duration,  $\Delta t$ , is chosen (typically 24 hours). Next, events are recorded for this duration and  $R(t)$  is calculated using events from the entire sky while  $\epsilon(h, \delta)$  is calculated using events from the entire duration. A pixel located at a right ascension of  $\alpha$  is at a local sidereal time  $t = \alpha + h$ . The time bins of  $R(t)$  where this relationship is true are multiplied by the corresponding bins in  $\epsilon(h, \delta)$ , and summed together, finally resulting in a single bin of  $B(\alpha, \delta)$ .

$$(98) \quad B(\alpha, \delta) = \sum_{t=0}^{2\pi} R(t)\epsilon(h, \delta)O(t, h, \alpha) ,$$

$$(99) \quad O(t, h, \alpha) = \begin{cases} 1, & \text{if } h = t - \alpha \\ 0, & \text{otherwise} \end{cases}$$

This effectively creates a background map of relatively uniform intensity. These maps have a striated structure as a result of the continual sum along sidereal time, but the effects of these fluctuations are small (see fig. 5.4). It is important to note that the sum used to calculate  $B(\alpha, \delta)$  does not distinguish between signal and background. As a result,  $B(\alpha, \delta)$  slightly over estimates the background at a given location on the sky. It is possible to compensate for this by masking regions of interest when the background is calculated, but these methods were not employed for this analysis because the effect is small (on the order of one part in ten thousand<sup>22</sup>). In 24 hours of recording time, approximately 40 million events are detected in the vicinity of the Crab nebula and the difference between this and the estimated background is on the order of 20 thousand.

---

<sup>22</sup>The ratio between excess and background in bin zero for the Crab is about .00013

For this analysis, the maximum significance on the Crab Nebula was detected at  $(83.62^\circ, 22.02^\circ)$ . The exact pixel location on the map is known to 0.0001 degrees, but the angular resolution of the detector is on the order of 0.01 degrees at the absolute best.

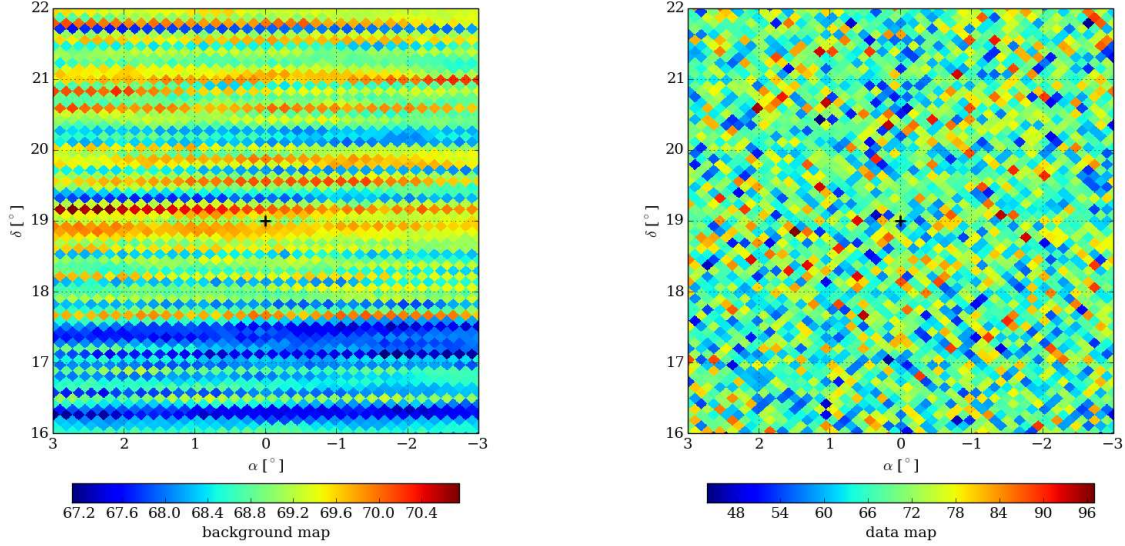


FIGURE 5.4. The background as expected using Milagro Direct Integration (MDI),  $B(\alpha, \delta)$  (left), and the measured signal,  $S(\alpha, \delta)$  (right) at zenith declination in number of events. The striations are a result of the integration over sidereal time. Note that the difference in scale was preserved in order to illustrate the structural difference between the MDI background and observed signal.

#### 5.4. PROBABILITY

The significance of deviation of signal above the expected background is calculated using Li & Ma equation 17 from [43]. This significance test assumes Poisson fluctuations and that the excess signal is small in comparison to background, which is ideal for HAWC.

$$(100) \quad N_s = \sqrt{2} \left\{ N_{on} \ln \left[ \frac{1 + \alpha_{LiMa}}{\alpha_{LiMa}} \left( \frac{N_{on}}{N_{on} + N_{off}} \right) \right] + N_{off} \ln \left[ (1 + \alpha_{LiMa}) \left( \frac{N_{off}}{N_{off} + N_{on}} \right) \right] \right\}^{\frac{1}{2}}$$

This expression was originally derived with a pointable telescope in mind, where  $N_{on}$  and  $N_{off}$  were the counts while pointing on and off source respectively,  $\alpha_{LiMa}$  is the relative time exposure between the two, and  $N_s$  is the number of standard deviations by which  $N_{on}$  exceeds  $N_{off}$ . HAWC however does not point, because it is an air shower array. Instead excess counts are found by taking the difference between skymaps. In this case, the on counts come from the signal map  $S(\alpha, \delta)$  while the off counts come from the background map  $B(\alpha, \delta)$ . The background map is over exposed in comparison to the signal map and the relative exposure corrects this.

$$(101) \quad N_{on}(\alpha, \delta) = S(\alpha, \delta)$$

$$(102) \quad N_{off}(\alpha, \delta) = \frac{B(\alpha, \delta)}{\alpha_{LiMa}}$$

Absolute significance values greater than  $5\sigma$  are usually considered to be a discovery by other experiments. For HAWC this is not necessarily the case. Due to the sheer amount of sky surveyed with the observatory and the point spread function of the detector, a  $5\sigma$  fluctuation may occur quite frequently. For example, suppose you were to randomly sample some value which follows a normal distribution. The odds of selecting a value at random beyond  $\pm 5$  standard deviations from the mean is 1 in 1,744,278. If you were to sample this distribution 17 million times, you would expect to get about 10 values outside of  $\pm 5\sigma$  just by sheer chance. For a large data set with no sources,  $N_s$  is normally distributed about 0 with a standard deviation of 1. The presence of sources and deficits appear as tails in this distribution (see fig. 5.6). If each pixel represented an independent sampling of this distribution and there are about 8 million observable pixels in the map used for this analysis, then a little less than 5 pixels with excess or deficits outside  $\pm 5\sigma$  would be expected to have

come from statistical fluctuations. However, each pixel *does not* represent an independent sampling of the significance distribution. This is because of the PSF of the detector. The excess in a single pixel is dependent on the excess in neighboring pixels, and so significantly more  $5\sigma$  fluctuations are present in the map than would be expected from purely independent sampling. As of this writing the trials factor, the factor by which the significance of a source is reduced due to the sample size, is still being discussed, and so the effect of trials on this analysis is not accounted for.

For this analysis, the Crab was detected at a significance of  $83\sigma$  above background (see fig. 5.5) and the trials factor is a non-issue.

## 5.5. $\chi^2$ AND MODELS

The goal of this analysis is to determine the spectral model and parameters which best describe the observed distribution of detected excess as a function of energy. A reasonable starting point is the spectral model discussed in chapter 1, equation 11. This is known as the two parameter model.

$$(103) \quad \frac{dN}{dE}(\Phi_o, \gamma) = \Phi_o \left( \frac{E}{E_o} \right)^\gamma .$$

In this equation,  $\Phi_o$  and  $\gamma$  are the fit parameters of flux and spectral index, respectively. The value  $E_o$  is known as the pivot of the spectrum and is a constant during fitting. It is chosen to maximize the linear independence of  $\Phi_o$  and  $\gamma$ . This model is perfectly fine in that it arises from simple assumptions and first principle equations used to describe the escape of high energy particles from plasma shock waves, but it isn't completely physical. The greatest non-physical attribute of the two parameter model is that it is not energy limited. It is unreasonable to assume that this model will hold at arbitrarily low or high energies.

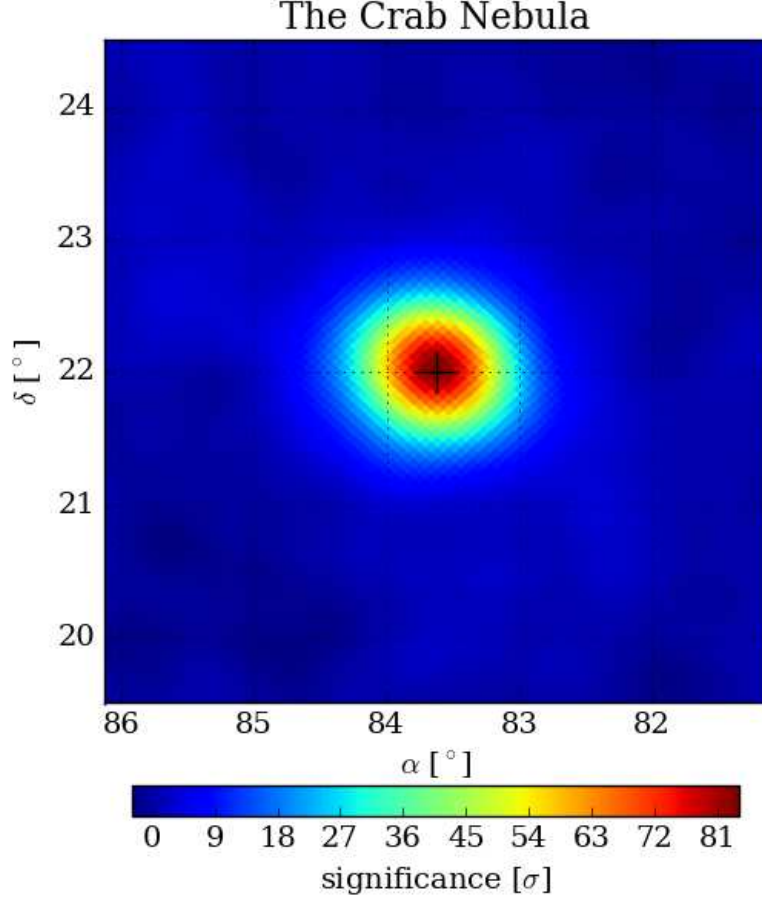


FIGURE 5.5. The spatial significance of the Crab nebula from HAWC-SP.

Low energy effects (characteristics that appear below 100 GeV) are not a major concern for this analysis, because events with sufficiently small energy will not trigger HAWC, and so don't need to be accounted for in this model. High energy effects *will* trigger the array, and do need to be accounted for. It is reasonable to assume that at some energy the type of processes at work will change, or the generated radiation will interact in some way. At that point, new gamma rays may not be observable or possibly even generated, and so the observed flux from the source will rapidly fall off. This suggests a third parameter which

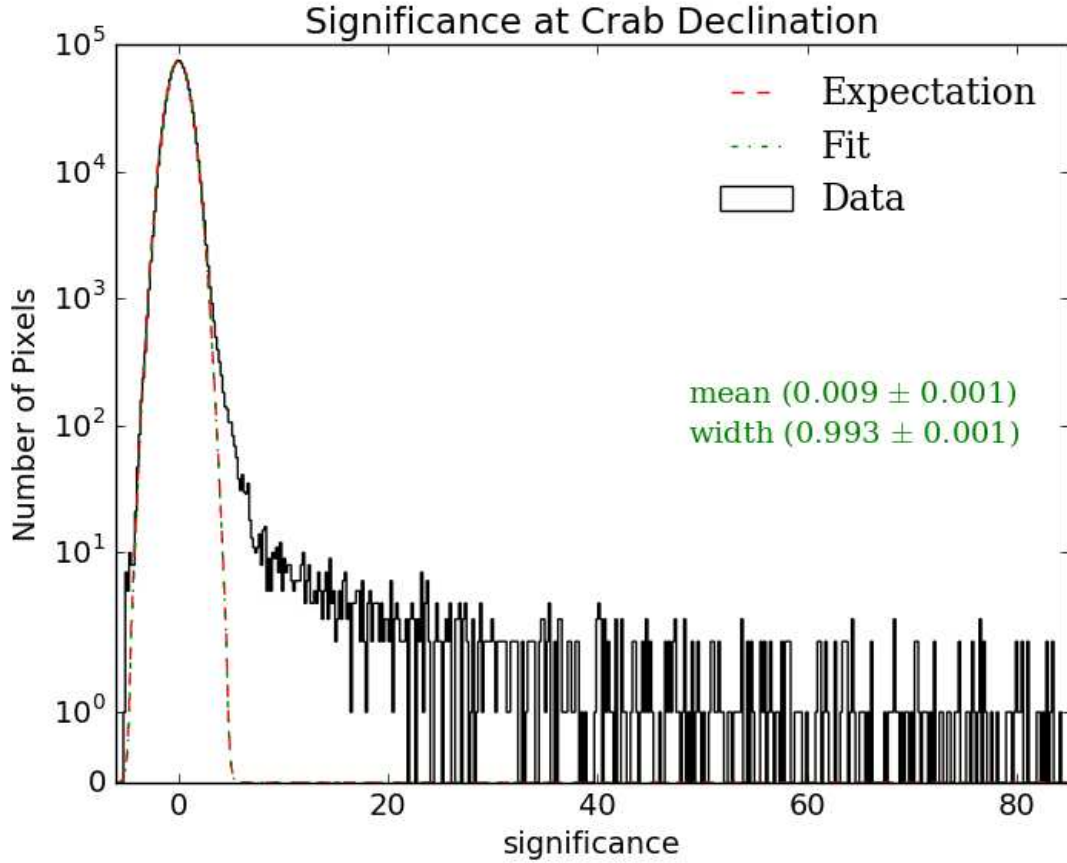


FIGURE 5.6. The distribution of significance for the skymap created with the HAWC-SP data. The tail on the far right indicates that there are intense sources present in the map.

encapsulates this idea.

$$(104) \quad \frac{dN}{dE}(\Phi_o, \gamma, E_c) = \Phi_o \left( \frac{E}{E_o} \right)^\gamma e^{-E/E_c} .$$

Here,  $E_c$  is the cutoff energy. As the measured energy approaches  $E_c$  the modeled flux will rapidly fall to zero. This is known as the three parameter model.

With the models well described mathematically, the question becomes this: Given a set of measurements of flux as a function of energy, which model and model parameters best

describes those measurements? This is an extremely common question in most scientific fields, including physics.

Suppose you were to take a set of measurements,  $y_i$ , which depend on some other variable,  $x_i$  (where the subscripts here represent the  $i^{th}$  measurement). Suppose also that you have a hypothesis: that  $y_i$  depends on  $x_i$  as described by some mathematical model  $y_i = f(x_i, \vec{\mu})$  where  $\vec{\mu}$  is a vector of your model parameters (for example, if the model is linear,  $\vec{\mu}$  would be a specific slope and intercept). If you were to take a great many measurements of  $y_i$  at a specific  $x_i$  then the distribution of measured  $y_i$  values would approach a normal distribution of width  $\sigma_{y_i}$  centered on a mean that can be considered to be the “true” value  $y'_i$ . The probability P of measuring a single  $y_i$  in this distribution is

$$(105) \quad P(y_i) \propto e^{-(y_i - y'_i)^2 / 2\sigma_{y_i}^2} .$$

If your hypothesis well describes this true value,  $y'_i = f(x_i, \vec{\mu})$ , then the probability P explicitly depends on  $\vec{\mu}$ .

$$(106) \quad P_{\vec{\mu}}(y_i) \propto e^{-(y_i - f(x_i, \vec{\mu}))^2 / 2\sigma_{y_i}^2} .$$

The joint probability of the hypothesis giving the true value of every single point is

$$(107) \quad P_{\vec{\mu}}(y_1, y_2, \dots, y_i) = P_{\vec{\mu}}(y_1) \times P_{\vec{\mu}}(y_2) \times \dots \times P_{\vec{\mu}}(y_i) \propto e^{-\chi^2/2} ,$$

where

$$(108) \quad \chi^2(\vec{\mu}) = \sum_i \frac{(y_i - f(x_i, \vec{\mu}))^2}{\sigma_{y_i}^2} .$$

This is known as the  $\chi^2$  statistic. The specific model parameters,  $\vec{\mu}$  which minimize  $\chi^2$  will maximize the probability that the measured values  $y_i$  were sampled from some true distribution described by  $f(x, \vec{\mu})$ . The procedure for determining  $\vec{\mu}$  seems simple, just search for those model parameters which minimizes  $\chi^2$ .

So what value of  $\chi^2$  is good? Any hypothesis can be chosen and a minimum  $\chi^2$  can be found for that hypothesis, so what characteristic values of  $\chi^2$  would indicate that the chosen model best fits the data? Too large and the model obviously does not describe the measurements well. Too small and the model describes the data *too* well<sup>23</sup>. In order to use  $\chi^2$  to claim agreement with a model (or exclusion of said model) a quantitative measure of “agreement” must be defined.

A good place to start is to determine the expected  $\chi^2$  measurement for a model that fits the data well. Such a model would ideally be within most of the error bars  $\sigma_{y_i}$  for the measurements  $y_i$ , and so each term in the  $\chi^2$  sum would be on the order of 1 or less and the total  $\chi^2$  would be on the order of the number of data points used to calculate the fit. In reality, the minimum  $\chi^2$  for a model that best fits the data is always less than the number of points. This is because the model parameters  $\vec{\mu}$  constrain the possible values that the other measurements could take. For example, consider trying to fit a line to a single point. An infinite number  $\vec{\mu}$  (slope intercept pairs) exist which define lines that pass through this single point. Once a second point is added, a single  $\vec{\mu}$  can be selected that *exactly* fits these two points, resulting in a  $\chi^2$  of precisely zero. Adding a third point would result in a  $\chi^2$  of order 1 or less because at least one point is free (the fit is not required to pass exactly through this point in order to distinguish a single  $\vec{\mu}$ ), and so on. As a result, the expected  $\chi^2$  for a good fit is approximately equal to the *number of degrees of freedom* between the

---

<sup>23</sup>Think connect the dots. This is known as overfitting or overtuning the model. A model with hundreds of parameters can fit any measurement you please.

model and the data. This number is defined as  $n - m$  where  $n$  is the number of data points and  $m$  is the number of parameters used to specify the model [44].

Given this, a new parameter can be defined, the reduced  $\chi^2$ , as the ratio of  $\chi^2$  to the number of degrees of freedom,

$$(109) \quad \tilde{\chi}^2 = \frac{\chi^2}{n - m} ,$$

and the goal is to find  $f(x, \vec{\mu})$  and  $\vec{\mu}$  such that  $\tilde{\chi}^2$  is close to 1. Quantifying the agreement between some model and some measurement is to set a limit on the maximum value of  $\tilde{\chi}^2$ , above which said model can be rejected. This is effectively setting a limit on the probability of finding a  $\tilde{\chi}^2$  at least as extreme (large) than the originally observed  $\tilde{\chi}^2$  when the experiment is repeated. If that probability is large, then the originally observed  $\tilde{\chi}^2$  is likely to occur given the hypothesis  $f(x, \vec{\mu})$ , and so there is no reason to doubt that  $f$  describes the measurements well. On the other hand, if the probability of finding a more extreme  $\tilde{\chi}^2$  is small, then the originally observed value is *unlikely* to occur given the hypothesis  $f(x, \vec{\mu})$ , and so  $f$  is rejected as a hypothesis. The plan of attack is therefore to first choose a rejection probability, and then determine the critical limit of  $\tilde{\chi}^2$  given that probability. If a tested model yields a minimum  $\tilde{\chi}^2$  that exceeds this critical limit, then that model can be rejected with the chosen probability.

In order to set this limit, the probability density of possible  $\chi^2$  values must be known for a given number of degrees of freedom. Probability can be a confusing topic<sup>24</sup> and so it's best to first cover the basics. Consider the function

$$(110) \quad f(y) = \frac{1}{\sigma_y \sqrt{2\pi}} e^{-y^2/2\sigma_y^2} .$$

---

<sup>24</sup>Anyone who says otherwise is lying.

In the language of statistics,  $f(y)$  is the probability density function of a random variable  $Y$  and is known as the normal or Gaussian distribution. It can be thought of having units of probability per unit of  $y$ . The best way to think about this is to imagine a machine that prints out a single number whenever you tell it to, and that the number it chooses is governed by  $f(y)$ . The single number you get from the machine is  $Y$ : a single draw from the distribution  $f(y)$ . If you get many numbers from the machine and create a histogram of the numbers the machine gives you, that histogram will be  $f(y)$  up to a scale factor as the number of draws approaches infinity. The probability of getting a number  $Y$  that is greater than  $y$  as governed by  $f$  is noted as  $P_f(Y > y)$  and is the integral of  $f(y)$  from  $y$  to positive infinity. The function  $f(y)$  is defined such that the total area under the curve is 1, and so the probability of getting  $Y > y$  is the area under the curve beyond that point, or the fraction of that area to the total area.

A single term in  $\chi^2$  is given by  $(y - y_{true})^2 / \sigma_y^2$  where  $y$  is normally distributed about  $y_{true}$  with a variance of  $\sigma_y^2$ . This should be equivalent to  $\chi^2$  with precisely one degree of freedom. Without losing generality, this can be shifted to be about zero, and so the probability density of  $y$  (and therefore  $\sigma_y \chi^2$ ) is exactly that given in equation 110.

Now, consider a new random variable,  $Z = Y^2$  (this is a good question to ask because  $\chi^2$  is governed by  $Y^2$ ). Imagine a new machine that prints out numbers equal to the square of those given to you by the first machine. What is the function  $g(z)$  which governs this machine? It is immediately obvious that  $P_g(Z < 0) = 0$  because the square of a number is always positive. The probability of drawing  $Z < z$  from  $g(z)$  must be equal to the probability of drawing  $Y^2 < z$ . The probability of drawing  $Y^2 < z$  from  $g(z)$  must be equivalent to drawing  $Y$  between  $\pm\sqrt{y}$  from  $f(y)$  for  $y = z$ , and as stated before this must be equal to the area under  $f(y)$  between  $\pm\sqrt{y}$ . This integral is therefore equal to  $P_g(Z < z)$  for  $z > 0$

and so the derivative of this with respect to  $z$  *must* be  $g(z)$ . To put it concisely,

$$(111) \quad P(Z < z) = \int_0^z g(z) dz = \int_{-\sqrt{z}}^{\sqrt{z}} f(y) dy$$

$$(112) \quad \therefore g(z) = \frac{d}{dz} \int_{-\sqrt{z}}^{\sqrt{z}} f(y) dy .$$

The limits of integration can be cleaned up a bit with some simple arguments,

$$(113) \quad P_f(-\sqrt{y} < Y < \sqrt{y}) = P_f(Y < \sqrt{y}) - P_f(Y < -\sqrt{y}) ,$$

$$(114) \quad = P_f(Y < \sqrt{y}) - (1 - P_f(Y < \sqrt{y})) ,$$

$$(115) \quad = 2P_f(Y < \sqrt{y}) - 1 ,$$

and so

$$(116) \quad g(z) = 2 \frac{d}{dz} \int_{-\infty}^{\sqrt{z}} f(y) dy ,$$

$$(117) \quad = 2 \frac{d}{dz} \int_{-\infty}^{\sqrt{z}} \frac{1}{\sigma_y \sqrt{2\pi}} e^{-y^2/2\sigma_y^2} dy ,$$

$$(118) \quad \therefore g(z) = \frac{1}{\sigma_y \sqrt{2\pi}} \frac{e^{-z/2\sigma_y^2}}{\sqrt{z}} .$$

This function,  $g(z)$ , is the probability density function which governs  $\chi^2$ , and can be used to calculate the critical  $\chi^2$  for some probability at one degree of freedom.

The general  $\chi^2$  distribution (see [45]) is known to be

$$(119) \quad g_k(z) = \frac{z^{k/2-1}}{2^{k/2}\Gamma(k/2)} e^{-z/2} ,$$

where  $\Gamma$  is the gamma-function,

$$(120) \quad \Gamma(t) = \int_0^{\infty} x^{t-1} e^{-x} dx ,$$

and  $k$  is the number of degrees of freedom. For this analysis,  $k = 6$  for the two parameter model and  $k = 5$  for the three parameter model (8 bins - 2 or 3 parameters). By setting  $k$  to the appropriate value, integrating from  $\chi^2$  to positive infinity and setting the result equal to 0.05, and then solving for  $\chi^2$ , the critical limit for  $\chi^2$  can be found for a rejection probability of 95% (which is the percent of  $1 - 0.05$ ). As it turns out, for  $k \leq 7$  the 95% critical  $\chi^2$  is approximately  $2k$ , and so for this analysis if at any time the chosen optimal fit has a minimum  $\tilde{\chi}^2 \geq 2.0$  the chosen model is rejected with a probability of at least 95%.

There is one last important thing to note about  $\chi^2$ . If there is no reason to doubt the tested model, then  $\chi^2$  can be used to determine the uncertainties on the fit parameters themselves. Consider the vector space spanned by all possible  $\vec{\mu}$  for a given model. This space would have a number of dimensions,  $p$ , equal to the number of parameters used in the model. The optimal  $\vec{\mu}$  for a given set of measurements is a single point in this space. Repeating the experiment and testing the new measurements will result in a new point in this space which may not be the same as the old point. Repeating the experiment many times will result in a  $p$  dimensional distribution of possible  $\vec{\mu}$ , each with a different  $\chi^2$ . The question is then, what is the region in  $p$  space that contains 68% ( $1 \sigma$ ) of these points? How is that region defined?

This concept was first described and expressed by the astrophysicist Yoram Avni in 1976 [46]. He found that these confidence regions in  $p$  space were defined by some increment,  $\delta$ , on the minimum  $\chi^2$ . This increment only depends on the dimension of  $\vec{\mu}$  and *not* the number of degrees of freedom of  $\chi^2$ . For  $p=2$  (the two parameter model) this increment is

2.30 and for  $p=3$  (the three parameter model) this increment is 3.50. This means that for the two parameter model, the region of  $\vec{\mu}$  space where solutions will fall 68% of the time is the defined by the contour of constant  $\chi^2$  which has a value of  $\chi_{min}^2 + 2.30$ . The size of this contour defines the statistical uncertainties on the parameters of the solution space.

## 5.6. FORWARD FOLDING

Because the energy resolution of HAWC is poor (about 50%) it is impossible to directly fit the measured flux as a function of energy (see section 5.2.1). Instead, fits are done with respect to fHit. In order to do this, distributions of the expected excess as a function of fHit must be simulated, and compared to data. The  $\chi^2$  statistic is used to determine the goodness of fit of these simulations with respect to the data. The spectrum that produces the simulated expectation distribution that minimizes  $\chi^2$  is then reported as the fitted spectrum for the data. This method of simulating a detector response and fitting the result to the observed result is known as Forward Folding and was most recently employed to great effect by Fermi-LAT [47]. At first glance this may seem like a computationally intensive task, but in reality it can be done very quickly.

Forward folding is most easily expressed in the language of linear algebra. Consider the measured excess  $E_i$  where the index  $i$  runs over the HAWC analysis bins. The measured excess can be expressed as the linear transformation of some real flux,  $f_j$  through some matrix  $C_{ij}$ , plus the measured background  $b_i$ , where the index  $j$  runs over real energy bins. In short,

$$(121) \quad E_i = C_{ij}f_j + b_i .$$

where the summation over  $j$  is implied. The matrix  $C_{ij}$  can be thought of the detector response matrix. Mathematically, it transforms  $f_j$  from the energy basis,  $j$ , to the analysis bin basis,  $i$ . In physical terms it maps a real flux through the detectors response, effectively simulating the detector output. If  $C_{ij}$  can be determined then the simulation of the expected excess of a given spectrum becomes computationally trivial.

In practical terms  $C_{ij}$  is created by first simulating some spectrum, in this case the Crab nebula as measured by HESS, at the declination of a source that is to be fit (that is,  $C_{ij}$  must be created for every unique declination to be analyzed). Distributions of the simulated energy for events passing signal selection cuts are created for each of the ten fHit bins. These energy distributions are then reweighed, energy bin by energy bin, by the inverse of the expected flux from the Crab nebula at the median energy of that bin. The result is a cache of distributions, where the distribution in the  $i^{th}$  analysis bin is weighted at a simulated energy,  $E_{MC}$ , by

$$(122) \quad W_i(E_{MC}) = \frac{X_i(E_{MC})}{F(E_{MC})} ,$$

where  $X_i(E_{MC})$  is the simulated excess in analysis bin  $i$  at energy  $E_{MC}$  and  $F(E_{MC})$  is the calculated expected flux of the Crab nebula at energy  $E_{MC}$ . The simulated excess of a new spectrum in a given fHit bin is just the integral of the appropriate distribution after it has been reweighed by the calculated flux of the new spectrum.

## 5.7. MINIMIZATION ALGORITHMS

With the ability to quickly calculate the value of  $\chi^2(\vec{\mu})$  for a given model and model parameters, the next goal is to determine the most efficient way to find the global minimum of  $\chi^2$ . The vector  $\vec{\mu}$  described in section 5.5 is a member of the vector space spanned by

all possible solutions for a single model. In the case of a linear model, this would be a 2-space spanned by all possible combinations of slope and intercept. Finding the minimum value of  $\chi^2(\vec{\mu})$  for such a linear model would involve traversing the space, ideally in some intelligent fashion, and evaluating  $\chi^2(\vec{\mu})$  at each traversal step until some minimum is found. Note that because such a space is continuous, it is impossible to find an *exact* solution that best fits a set of physical measurements because that would require an arbitrary precision. In reality, the precision of the solution is limited either by the physical uncertainty of the measurements (either statistical or systematic) or the resolution of the searching method, whichever is worse.

The first, most direct algorithm used in this analysis for finding the minimum  $\chi^2(\vec{\mu})$  is a process known as grid searching. A grid search of the vector space  $\vec{\mu}$  involves dividing the space into a grid, evaluating  $\chi^2(\vec{\mu})$  at each grid intersection, and then simply selecting the smallest value. There are some serious issues with this algorithm, but there are also a couple benefits. First, a coarse evaluation of  $\chi^2(\vec{\mu})$  across the whole space is needed to properly characterize the uncertainties associated with the fit parameters. Second, if the grid resolution can be arbitrarily large (so the grid spaces are arbitrarily small) a grid search will always return the global minimum of the scanned space. That is to say, the grid search algorithm cannot be trapped by local minima or by regions where the change in  $\chi^2(\vec{\mu})$  is very small. On the other hand there are a number major drawbacks. First is the prohibitive cost (in number of function evaluations) of searching the entire space. This cost rises exponentially with the resolution and the number of dimensions in the vector space (so with 10 evaluations per dimension, it would take 100 evaluations to search two dimensions, 1000 for three, etc...). Second, the precision of the solution is directly dependent on the resolution of the search. At best, a solution reported via direct grid search has an absolute

minimum uncertainty of about one grid width. Finally, using the grid search method requires some knowledge about where to begin searching *and* knowledge about the possible range of reasonable solutions. For these reasons, grid searching was used for minimization for only those sources which could not be constrained to the three parameter model, and for all sources in order to evaluate the uncertainty on the fit parameters.

The second algorithm used for  $\chi^2(\vec{\mu})$  minimization in this analysis is the Nelder-Mead simplex descent algorithm. The simplex descent algorithm is a heuristic search algorithm that can be applied to any n dimensional space, and does not require any knowledge or evaluation of the derivatives of the objective function to be minimized ( $\chi^2(\vec{\mu})$  in this case). The algorithm functions by first defining a simplex of n+1 points within the search space (so a triangle in two dimensions, a tetrahedron in 3 dimensions, etc...). This simplex is deformed and moved through the space based on the evaluation of the objective function at the vertices. The goal of simplex descent is to encapsulate the global minimum within the simplex, and then contract the simplex around the minimum until the difference in the relative positions of the vertices is small, at which point the algorithm ends. Once a simplex of n+1 points  $\vec{\mu}_1, \vec{\mu}_2, \dots, \vec{\mu}_{n+1}$  has been chosen a single cycle of the descent algorithm is defined as follows.

First, all points in the simplex are sorted in ascending order based on the evaluation of  $\chi^2$  and the centroid,  $\vec{C}$ , of all but the worst point (the one with the largest  $\chi^2$  value,  $\vec{\mu}_{n+1}$ ) is calculated,

$$(123) \quad \chi^2(\vec{\mu}_1) \leq \chi^2(\vec{\mu}_2) \leq \dots \leq \chi^2(\vec{\mu}_{n+1}) ,$$

$$(124) \quad \vec{C} = \frac{1}{n} \sum_{i=1}^n \vec{\mu}_i$$

Next the worst point in the simplex,  $\vec{\mu}_{n+1}$ , is reflected across the centroid, creating a new point  $\vec{\mu}_r$ ,

$$(125) \quad \vec{\mu}_r = \vec{C} + (\vec{C} - \vec{\mu}_{n+1}) .$$

If  $\vec{\mu}_r$  is better than  $\vec{\mu}_n$  but worse than  $\vec{\mu}_1$  (that is,  $\chi^2(\vec{\mu}_1) < \chi^2(\vec{\mu}_r) < \chi^2(\vec{\mu}_n)$ ) then the reflected point would improve the simplex. The worst point is replaced by  $\vec{\mu}_r$  and the cycle returns to the beginning.

If it turns out that  $\vec{\mu}_r$  is better even than the best point  $\vec{\mu}_1$  (that is, if the reflected point leads “downhill”), then the expanded point,  $\vec{\mu}_e$  is created and tested,

$$(126) \quad \vec{\mu}_e = \vec{C} + 2(\vec{\mu}_r - \vec{C}) .$$

If this expanded point is better than the reflected point,  $\chi^2(\vec{\mu}_e) < \chi^2(\vec{\mu}_r)$ , then the worst point is replaced by the expanded point and the cycle returns. Otherwise the worst point is replaced by the reflected point and the cycle returns.

If the cycle hasn’t returned by this point, it is certain that  $\vec{\mu}_r$  is between point  $n$  and  $n + 1$ . If this occurs, then the contracted point,  $\vec{\mu}_c$  is created and tested,

$$(127) \quad \vec{\mu}_c = \vec{C} + \frac{1}{2}(\vec{\mu}_{n+1} - \vec{C}) .$$

If the contracted point is better than the worst point,  $\chi^2(\vec{\mu}_c) < \chi^2(\vec{\mu}_{n+1})$ , then the worst point is replaced and the cycle returns.

If this fails, then the simplex is reduced with respect to the best point,  $\vec{\mu}_1$ . All points except the best point move towards the best point,

$$(128) \quad \vec{\mu}_i = \vec{\mu}_1 + \frac{1}{2}(\vec{\mu}_i - \vec{\mu}_1) ,$$

and the cycle returns.

This descent method is relatively insensitive to local minima and starting conditions, and is much faster than a simple grid search. A precise three parameter grid search with 100 bins per dimension takes upwards of 1 hour for this analysis. Simplex descent accomplishes the same task in a matter of seconds. Because the algorithm is heuristic, there is no way of knowing if the solution returned by this method is indeed the optimal one, but this issue is mitigated by throwing multiple simplex starting conditions, and taking the best returned result.

## 5.8. UNCERTAINTIES

It is impossible to perfectly match a mathematical model to real data. This is a direct result of the presence of both statistical and systematic uncertainties. Statistical uncertainties (those that result from the natural fluctuations in any physical measurement) will always be present, and can really only be mitigated by taking more observations. There are three statistical uncertainties that need to be accounted for when fitting spectra with HAWC, and these are the uncertainties associated with the measured number of events, the estimated background, and the simulation. The statistical uncertainty for the measured number of events and the estimated background (done via MDI) are both assumed to be derived from Poisson statistics. The distribution in the difference in time of sequential events detected with HAWC is inversely exponential. The more time that passes after an event is detected,

the more likely it is that another will follow. This leads to a distribution of the number of detected events per unit time that is Poissonian,

$$(129) \quad P(n) = \frac{\lambda^n e^{-\lambda}}{n!} ,$$

where  $P(n)$  is the probability of detecting  $n$  events within some interval, and  $\lambda$  is the average number of events in the interval. This distribution has the interesting property that the variance of the distribution is the mean,  $\lambda$ . The number of events detected in an fHit bin is taken to be the mean,  $\lambda$ , of this distribution and so the uncertainty in that number is the standard deviation, or  $\sqrt{\lambda}$ .

The statistical uncertainty inherent in the simulation is somewhat trickier, because as discussed in the previous chapter, the simulation has no “time”. Instead this must be derived through the propagation of the uncertainty in the weights. The number of simulated events from forward folding in a single fHit bin,  $MC$ , is

$$(130) \quad MC = \sum_i W_i N_i ,$$

where  $W_i$  is the forward folding weight for the  $i^{th}$  energy bin of this fHit bin, and  $N_i$  is the sum of transit weights in that bin (effectively the number of simulated events at energy bin  $i$ ). The uncertainty in  $MC$ ,  $\sigma_{MC}$  comes from error propagation of  $W_i$  [44].

$$(131) \quad \sigma_{MC}^2 = \sum_i \left( \frac{\partial MC}{\partial N_i} \sigma_{N_i} \right)^2 .$$

The partial derivative picks out a single  $W_i$ , and so

$$(132) \quad \sigma_{MC}^2 = \sum_i W_i^2 \sigma_{N_i}^2 .$$

The variance in  $N_i$  is entirely dependent on the transit weighted sum of actual thrown simulations in energy bin  $i$ .

$$(133) \quad N_i = \sum_j \text{Twgt}_j M_j ,$$

where  $\text{Twgt}_j$  is the transit weight for the simulated source as calculated with equation 82 and  $M_j$  is the number of thrown events with weight  $\text{Twgt}_j$ . As before, calculating  $\sigma_{N_i}^2$  involves propagating uncertainty.

$$(134) \quad \sigma_{N_i}^2 = \sum_j \left( \frac{\partial N_i}{\partial M_j} \sigma_{M_j} \right)^2 ,$$

$$(135) \quad = \sum_j \text{Twgt}_j^2 \sigma_{M_j}^2 .$$

The uncertainty,  $\sigma_{M_j}$ , is the uncertainty of throwing  $M_j$  events in the simulation that have a weight  $\text{Twgt}_j$ . This number is non zero because the simulation is governed by Monte Carlo processes. Ideally, we can assume that the random number generator used in the Monte Carlo is perfect, and so  $\sigma_{M_j}$  would be the same as if *real* events were observed with the raw simulated spectrum. Therefore,  $\sigma_{M_j}$  must be  $\sqrt{M_j}$  and so

$$(136) \quad \sigma_{N_i}^2 = \sum_j \text{Twgt}_j^2 M_j = \sum_k \text{Twgt}_k ,$$

$$(137) \quad \therefore \sigma_{MC}^2 = \sum_i \sum_k W_i^2 \text{Twgt}_k^2 ,$$

Where, again,  $i$  is over energy bins and  $k$  is over the actual thrown events in bin  $i$ . Recall that  $\text{Twgt}$  contains a factor of  $1/N_{\text{thrown}}$ . More than six million events are simulated for

gamma rays alone, and so this uncertainty is vanishingly small (much less than one event) and can be ignored. It is included in this analysis for completeness.

Systematic uncertainties (those which result from the imperfections present in the detector or the analysis method) can be reduced by either modifying the detector or the detector simulation. Systematic uncertainties are therefore disagreements between the simulated behavior of a detector and the observed behavior (assuming no unknown physics is at work). These disagreements must be minimized or at least characterized in order to detect the presence of new physics. For every variable used to cut data for this analysis, there is an associated systematic.

#### 5.8.1. fHit.

The systematic uncertainty in fHit represents a disagreement between the number of PMTs in the simulation compared to the real detector. In order to quantify the effects of a disagreement in fHit on the fit spectra, data from the mid stages of the construction of HAWC, known as HAWC-111, were fit and examined. These data are described in section 5.1. In order to do this properly a separate set of cuts needed to be defined and optimized assuming 365 PMTs for epochs 1 and 429 PMTs for epoch 2(see table 5.3).

As these data were recorded before the creation of PINCness, the core fit  $\chi^2$  is used in its place.

The methods and the two parameter model from section 5.6 were used to fit the spectrum of the Crab nebula using epoch 1 and epoch 2 data. Only the two parameter model was used because there is insufficient data in epoch 1 and 2 to constrain the three parameter model. The  $\chi^2$  space spanned by  $\Phi_o$  and  $\gamma$  was scanned to directly find the global minimum. First, the Crab nebula was fit using the epoch 1 and 2 data sets independently using only bins 2 through 9.

TABLE 5.3. Cuts used in the analysis of epoch 1 and epoch 2 data for HAWC.

Bin #	fHit >	fHit ≤	Angular Bin (degrees)	Compactness >	Core Fit $\chi^2 <$	Angle Fit $\chi^2 <$
0	0.045	0.067	2.26	2.0	13.0	13.0
1	0.067	0.105	1.94	3.0	18.0	12.0
2	0.105	0.164	1.48	4.5	21.0	11.0
3	0.164	0.252	1.10	6.0	20.0	10.0
4	0.252	0.371	0.95	8.0	14.0	8.0
5	0.371	0.511	0.80	11.0	15.0	7.0
6	0.511	0.655	0.80	12.0	11.0	8.0
7	0.655	0.781	0.75	15.0	12.0	6.0
8	0.781	0.878	0.45	20.0	12.0	14.0
9	0.878	1.00	0.35	13.0	22.0	14.0

The epoch 1 spectrum was

$$(138) \quad \frac{dN}{dE}(\Phi_o, \gamma) = (3.63 \pm_{0.91}^{1.2}) \times 10^{-11} \left( \frac{E}{1\text{TeV}} \right)^{-2.59 \pm 0.23},$$

with a  $\chi^2$  of 1.85 and the epoch 2 spectrum was

$$(139) \quad \frac{dN}{dE}(\Phi_o, \gamma) = (3.71 \pm_{0.96}^{1.3}) \times 10^{-11} \left( \frac{E}{1\text{TeV}} \right)^{-2.65},$$

with a  $\chi^2$  of 6.86 with 6 degrees of freedom. The pivot of  $E_0 = 1\text{TeV}$  was chosen to make the fit results easily comparable to HESS. The tilt of the ellipsoidal contours of the  $\chi^2$  space for both fits indicate that the fit parameters are not linearly independent of each other (see fig. 5.7 and 5.8). This will be examined and corrected for, but for now it does not matter as only the change in the minimum is used for this systematic study (the statistical uncertainties in these fits were ignored when calculating the systematic).

The epoch 2 fit has a slightly steeper index than the epoch 1 fit. This is an effect resulting from the geometry of HAWC and the choice of binning variable. A 10 TeV shower will saturate HAWC: every single PMT will probably trigger if such a shower lands on the

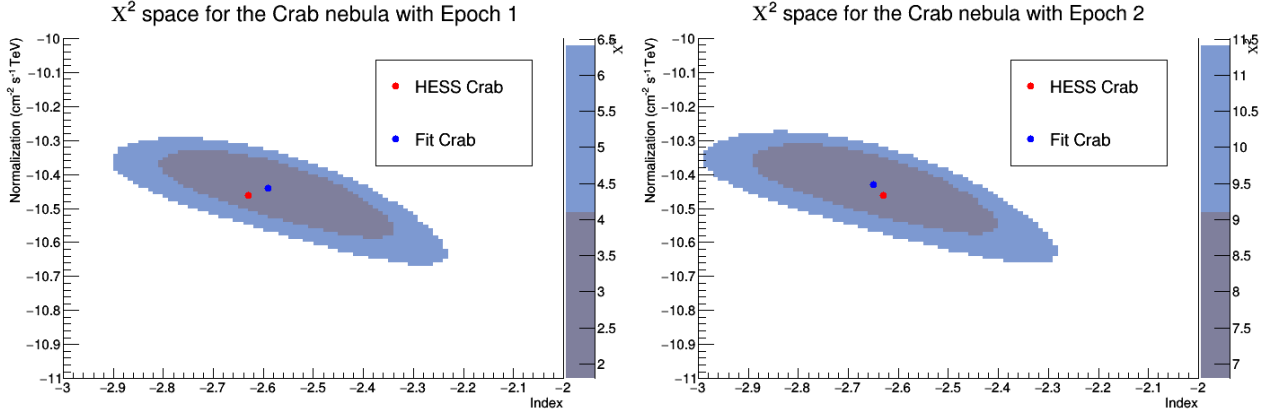


FIGURE 5.7. The  $\chi^2$  space for the epoch 1 fit (left) and the epoch 2 fit (right). The dark region represents  $1\sigma$  uncertainty and the light region is  $2\sigma$ . Both are within  $1\sigma$  of the HESS spectrum

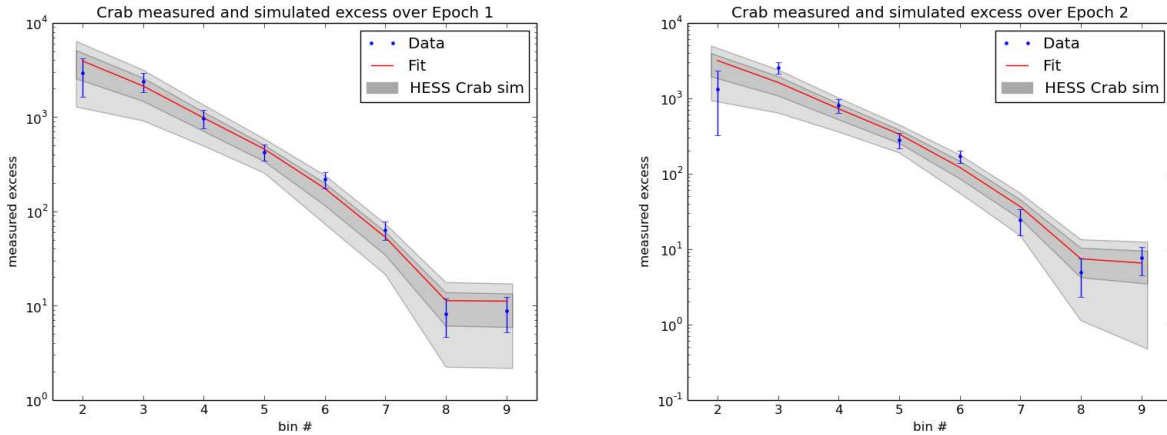


FIGURE 5.8. The epoch 1 fit (left) and epoch 2 fit (right). The dark and light grey bands represent the  $1\sigma$  and  $2\sigma$  excess uncertainties predicted the simulation of the HESS Crab.

array. The proxy energy variable used in this analysis is fHit: the fraction of the array triggered by a shower. Because of this epoch 1 has a lower saturation energy than epoch 2. Any events above this saturation energy will fall into the last few bins (depending on where it lands on HAWC). For equal exposures to the same source, the excess counts in the higher energy bins of epoch 1 are expected to be slightly larger than those in epoch 2, thus resulting in a slightly harder spectrum for epoch 1.

Using these fit results, the systematic uncertainty in the fit parameters can be estimated by examining the fit values as a function of the number of PMTs in the array. Remember, the primary thing that changed between epoch 1 and epoch 2 was the number of PMTs present in the HAWC array. Knowing this, the increase of 64 PMTs from epoch 1 to epoch 2 steepened the index and increased the normalization of the fit spectrum by 2.3% (from -2.59 to -2.65 in index and from -10.44 to -10.43 in  $\log(\text{Norm})$ ). This means that, assuming the relationship is linear, every inactive PMT in the full HAWC array will shift the index down and the normalization up by 0.035% per PMT when fit with a pivot of 1 TeV. Assuming a liberal estimate of 10% of the array being offline at any given time (120 PMTs), this effect would contribute 4.2% to the total systematic uncertainty.

If there is a sufficiently large number of inactive PMTs, then handling the resulting data will resemble the combined epoch 1+2 data set. In order to analyze the combined epoch 1 and 2 data set (and therefore compensate for any systematic that results from a change in the number of active PMTs), the fraction of the total data comprising each epoch must be determined. This can be found either by directly fitting for the fraction of epoch 1 in the joint data set, or by calculating a theoretical value based on live time and area.

Assuming that the measured excess is represented by some linear combination of the epoch 1 and 2 measurements, then

$$(140) \quad E_{12} = aE_1 + (1 - a)E_2 .$$

Fitting this value to the measured excess in the combined data set results in  $a = 0.51 \pm 0.20$ .

Ignoring any effects that do not directly involve the detector, the total raw number of gamma ray events in an epoch is proportional to the duration in which data was recorded, and the effective area of the detector. The effective area of the detector is directly proportional

to the number of PMTs in HAWC. This suggests that

$$(141) \quad E_{12} = \frac{bE_1 + cE_2}{b + c} ,$$

where

$$(142) \quad b = (\textit{duration of epoch 1})(365 \textit{ PMTs}) ,$$

and

$$(143) \quad c = (\textit{duration of epoch 2})(429 \textit{ PMTs}) .$$

The duration of epoch 1 was 2,507 hours and the duration of epoch 2 was 1,843 hours.

Relating these values to  $a$  shows that

$$(144) \quad a = \frac{b}{b + c} = 0.53 ,$$

which agrees with the fit result for  $a$ .

The Crab spectrum for the data set containing both epoch 1 and 2 was fit by creating a cache file for each of the epoch 1 and epoch 2 configurations. The expectation used for forward folding was then calculated using

$$(145) \quad E_{total} = aC_{ij1}f_j + (1 - a)C_{ij2}f_j + b_{1+2} ,$$

with a value of  $a = 0.53$ , which is consistent with the fit result of  $a = 0.51 \pm 0.20$ . This resulted in the spectrum

$$(146) \quad \frac{dN}{dE}(\Phi_o, \gamma) = (3.46 \pm_{0.65}^{0.79}) \times 10^{-11} \left( \frac{E}{1\text{TeV}} \right)^{-2.62 \pm 0.17},$$

with a  $\chi^2$  of 4.55 and 6 degrees of freedom (8 bins - 2 parameters). This also agrees with the results from HESS, but is significantly closer in both index and norm than the epoch 1 and epoch 2 fits alone (because of the difference in exposure, see figs 5.9 and 5.10). This suggests that the reweighting method used is a reasonable way to compensate for the change in the number of PMTs from epoch 1 to epoch 2.

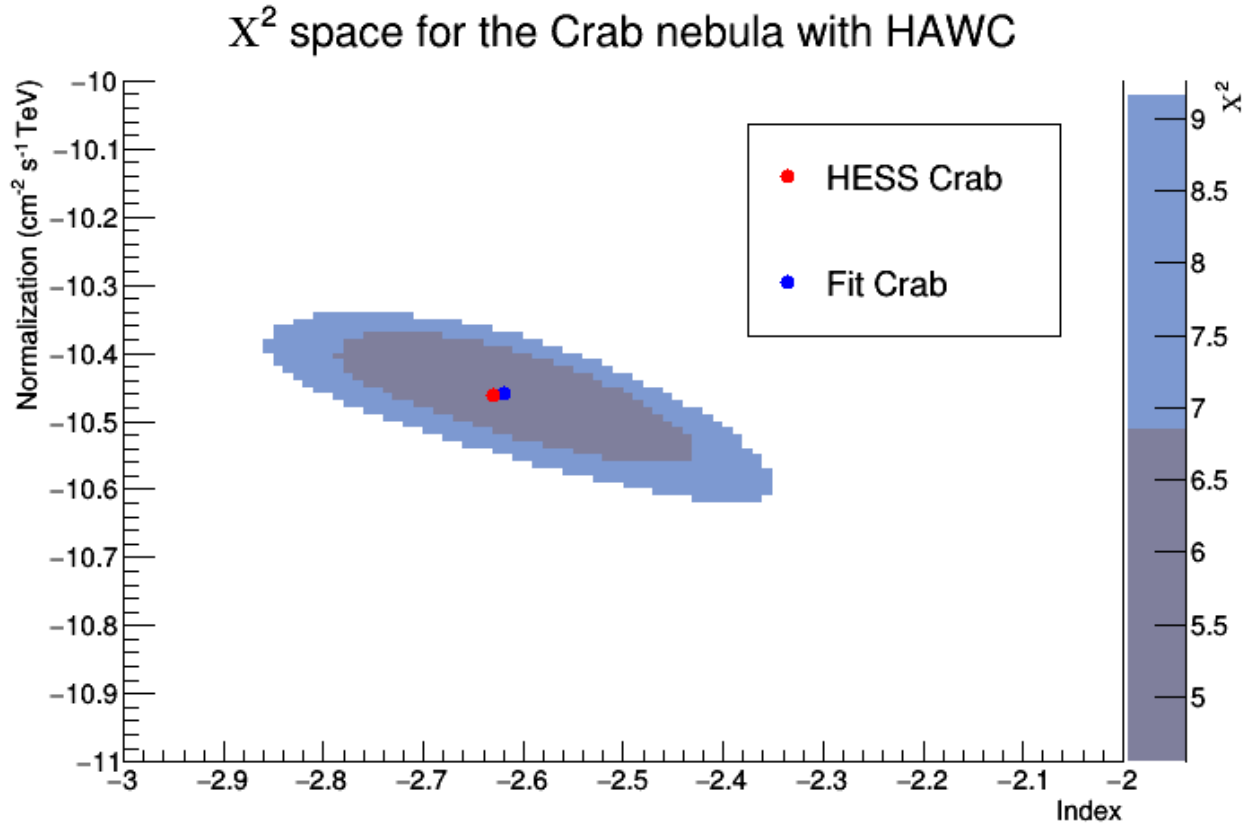


FIGURE 5.9. The epoch 1+2  $\chi^2$  space. The dark region represents  $1\sigma$  uncertainty and the light region is  $2\sigma$ .

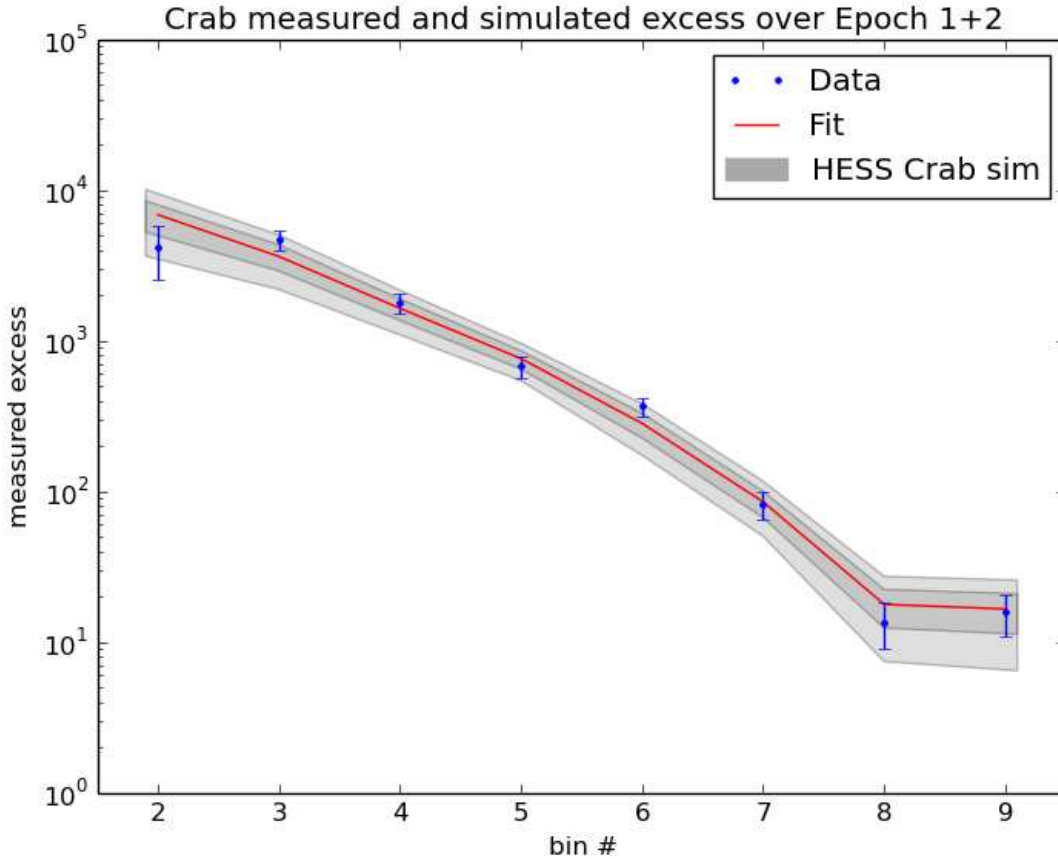


FIGURE 5.10. Resulting fit for the epoch 1+2 analysis. The dark and light gray bands represent the  $1\sigma$  and  $2\sigma$  excess uncertainties predicted by the simulation of the HESS Crab.

### 5.8.2. ANGULAR BIN.

The systematic uncertainty in the angular bin is a result of the disagreement between the simulated and measured PSF for HAWC. Quantifying this difference is a difficult task because determining the angular uncertainty of HAWC without simulation requires knowing the true origin location on the sky for a given event. It is impossible to know with certainty the origin of a single event, and so it is impossible to calculate the angular difference between the reconstructed and true origin on an event by event basis. That said, it is possible to examine a well known point source and determine the angular uncertainty (and therefore the PSF) from that. If the angular extent of a source is very small within the field of

view of a detector, then the measured distribution of events around that source is the PSF. Conveniently, the Crab fits this criteria well.

Determining the optimal angular bin from data can be done in two ways, just as it can be done in simulation: either fit a double Gaussian to the distribution of events vs angular distance from the Crab and calculate the analytical optimal bin, or select the angular bins that numerically maximize the significance of the source (see figs 5.11 and 5.12). These methods will yield slightly different angular bins, and so both should be examined to determine a systematic uncertainty in the PSF. The angular bins resulting from applying these methods to the data are in table 5.4.

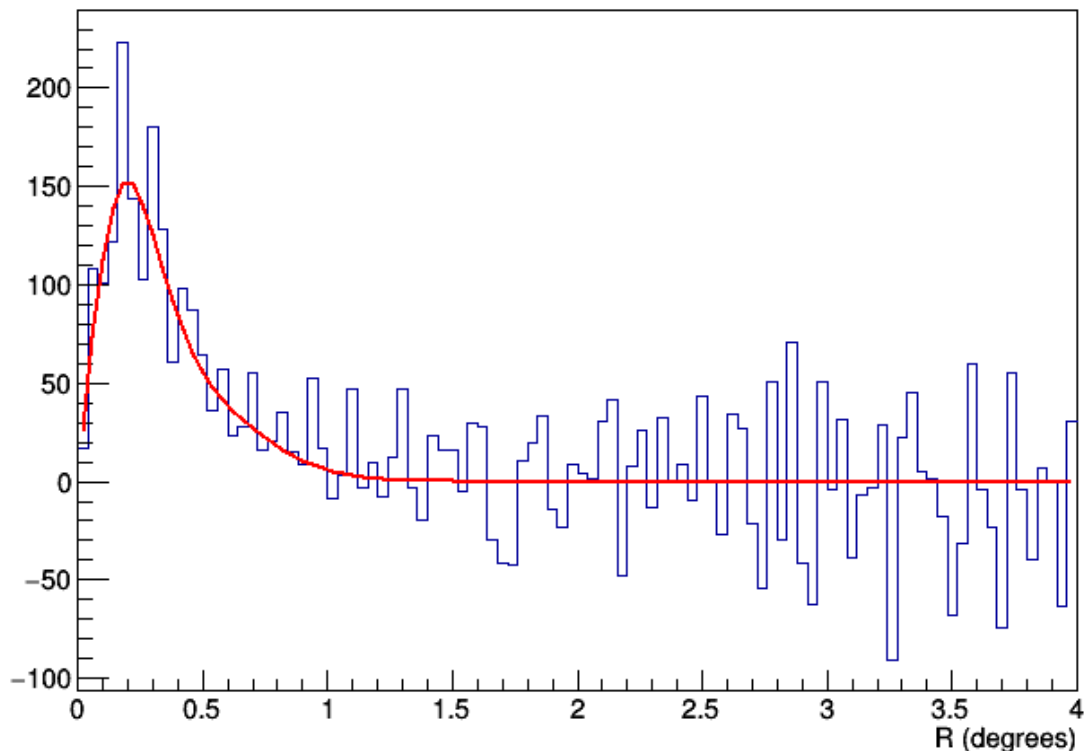


FIGURE 5.11. The distribution of the excess events in a given pixel as a function of the radial distance from the Crab to said pixel. The integral of this distribution from 0 to  $r$  will be the measured excess in an angular bin of radius  $r$  degrees. The red line is a double Gaussian fit.

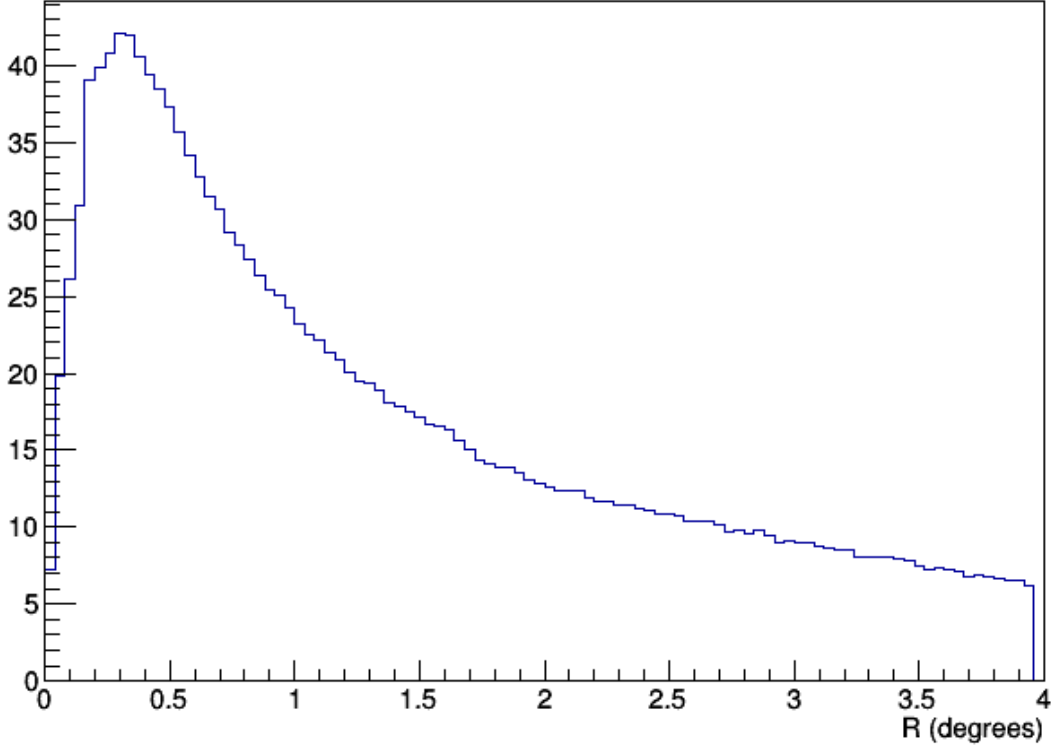


FIGURE 5.12. The distribution of significance as a function of angular bin size  $R$  (the integral of figure 5.11). The maximum significance is found at  $R = 0.3^\circ$ .

Using the values from calculating the optimal angular bin based on fitting the PSF to data results in the spectrum

$$(147) \quad \frac{dN}{dE}(\Phi_o, \gamma, E_c) = (3.34 \pm_{0.29}^{0.32}) \times 10^{-11} \left( \frac{E}{1\text{TeV}} \right)^{-2.55 \pm 0.09} e^{-E/150 \pm_{130}^{987}\text{TeV}},$$

With a  $\chi^2$  of 8.48 with 5 degrees of freedom (8 bins - 3 parameters). Again, the statistical uncertainties are not used to determine the systematic uncertainty. Using the values from choosing the angular bins which optimize the significance on the Crab in data results in the spectrum

$$(148) \quad \frac{dN}{dE}(\Phi_o, \gamma, E_c) = (3.60 \pm_{0.24}^{0.26}) \times 10^{-11} \left( \frac{E}{1\text{TeV}} \right)^{-2.60 \pm 0.07} e^{-E/319 \pm_{270}^{1788}\text{TeV}},$$

TABLE 5.4. Comparing the analytical optimal bin to the numerical solution. The analytical bins were chosen for this analysis because the numerical bins are limited by the bin width used to discretize the PSF distribution into a histogram.

Bin #	Chosen analytic bins (sim)	Crab analytic bins (data)	Crab numerical bins (data)
0	1.069	0.00214	3.70
1	0.849	0.979	1.34
2	0.652	0.553	0.70
3	0.522	0.520	0.58
4	0.419	0.395	0.38
5	0.353	0.276	0.30
6	0.337	0.227	0.26
7	0.250	0.233	0.18
8	0.231	0.182	0.18
9	0.202	0.115	0.14

With a  $\chi^2$  of 8.41 with 5 degrees of freedom (8 bins - 3 parameters). These are perfectly reasonable fits ( $\tilde{\chi}^2 < 2.0$  in both cases) which can yield some insight. First, it is probably impossible to constrain the cutoff of the spectrum with HAWC in a meaningful way, as slight changes to the angular bin dramatically changed the cutoff. This suggests that the systematic uncertainty on the cutoff is demonstrably large and dependent on the angular bin size. Second, without knowing the true Crab spectrum, the minimum systematic uncertainty on the index and normalization from an inaccurate characterization of the angular resolution can be estimated by comparing these two fit results. From this, the estimated minimum normalization systematic is 7% and the index systematic is 2%

### 5.8.3. CXPE AND PINC.

The compactness and PINCness are both gamma hadron separators, and so disagreements between data and simulation on these parameters should also lead to an estimate of systematic error in the spectral fit. The first step in characterizing this systematic uncertainty is

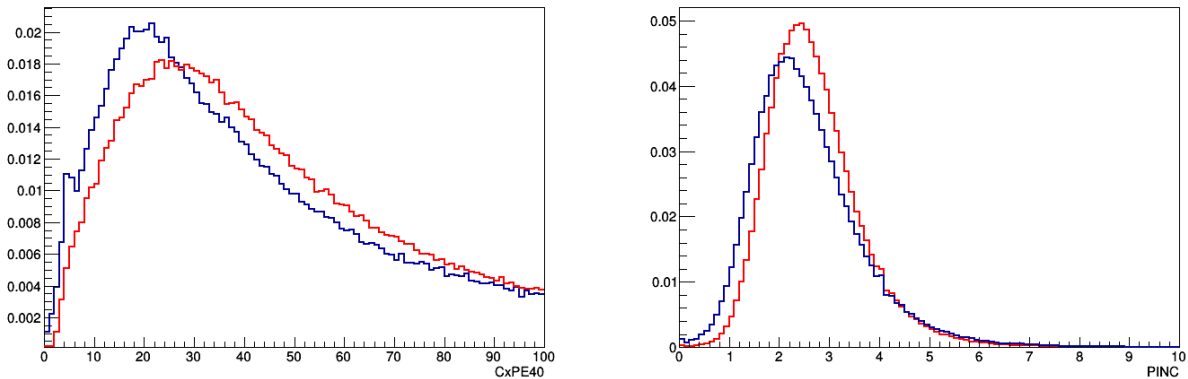


FIGURE 5.13. The normalized distributions of CxPE40 (left) and PINC (right) for both data (blue) and simulation (red) for bins 2-9.

to measure the difference between the simulation and data for both CxPE and PINC (see fig 5.13).

As it turns out these differences are small and the distributions are qualitatively similar when examining bins 2-9. Instead of tuning these variables in each individual bin, each individual value for PINC and CxPE in the simulation was shifted by a multiplicative factor equal to the fractional difference between data and simulation in the means of the distributions from fig 5.13. CxPE and PINC values in the simulation were shifted down by 1.05% and 5.31% respectively. The Crab nebula was then fit using the “corrected” simulations, resulting in a spectrum of

$$(149) \quad \frac{dN}{dE}(\Phi_o, \gamma) = (3.54) \times 10^{-11} \left( \frac{E}{1\text{TeV}} \right)^{-2.66} e^{-E/294\text{TeV}} ,$$

with a  $\chi^2$  of 4.01 and 5 degrees of freedom (8 bins - 3 parameters). This change to the simulation shifted the normalization by 1.1% and the index by 4.5% for the fit with a pivot of 1 TeV. The shift in the cutoff was again more than 100%, suggesting the true systematic uncertainty in the cutoff is huge.

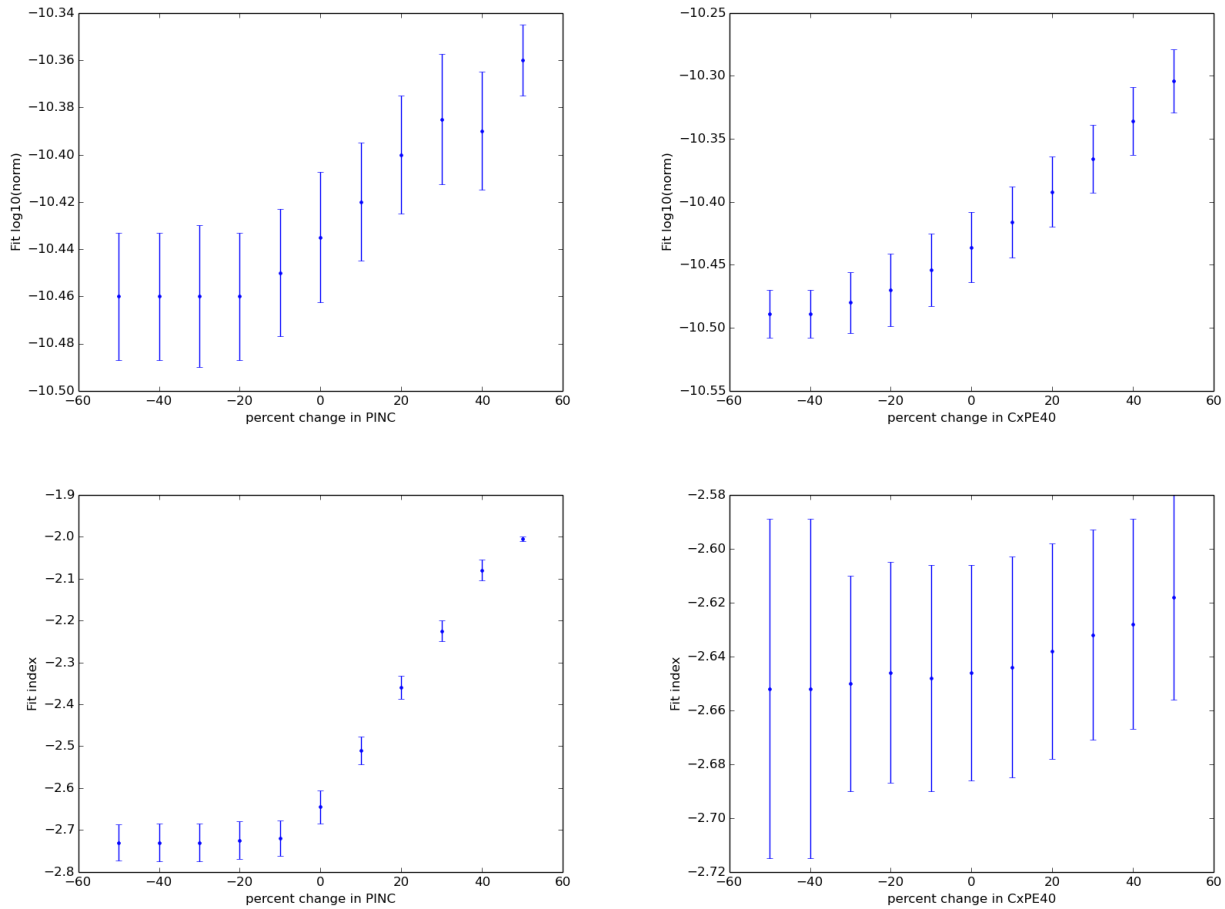


FIGURE 5.14. The change in resulting fit two parameter spectra as a function of shift in CxPE or PINC.

Scanning through a range of shift values and fitting the resulting simulations to data illustrates sensitivity of the fit parameters to both CxPE and PINC (see fig 5.14). The fit index is most sensitive to changes in PINC, requiring a disagreement between simulation and data of only 10-20% in order to change the index by 10% while CxPE would have to disagree by more than 60% to affect the same change. The fit normalization is most sensitive to changes in CxPE, requiring a disagreement between simulation and data of 20-30% in order to change the  $\log(\text{Norm})$  by 1%, while PINC would have to disagree by more than 60% to affect the same change. It is for this reason that both of these gamma-hadron separators are included in this analysis.

#### 5.8.4. TOTAL SYSTEMATIC.

Each of the systematics addressed above shifts the index and normalization of the spectral fit in a specific direction. However, this systematic study only quantifies the difference between the data and Monte Carlo simulations, and not *what* causes the disagreement. Because of this, the systematics used for this analysis cannot be corrected for. Indeed, it isn't even possible to say with certainty that determining the cause of the disagreements and correcting them would shift the spectrum in the appropriate direction, because it could result in new systematics which have not been addressed here. As a result, this study can only say that the fit results are within some estimated systematic range. A liberal estimate for the minimum systematic uncertainty would be the sum of the discussed systematics, or 12.3% uncertainty in normalization and 10.7% uncertainty in index at a pivot of 1 TeV (see table 5.5). The uncertainty in the cutoff as estimated by these methods is almost certainly on the order of 100%, and so only the statistical uncertainty will be reported.

TABLE 5.5. The systematics used for this analysis.

Source	% of Norm (1 TeV)	% of Index (1 TeV)	% of Norm (4 TeV)	% of Index (4 TeV)
fHit (10% array failure)	4.2%	4.2%	4.2%	4.2%
Optimal Bin	7%	2%	0.62%	2.3%
CxPE and PINC	1.1%	4.5%	14%	4.5%
Total	12.3%	10.7%	18.8%	11%

## 5.9. THE CRAB SPECTRUM

The methods and spectral models from the previous sections were used to fit the spectrum of the Crab nebula using HAWC-SP. Bins 0 and 1 were excluded, and the resulting fit for the two parameter model was

$$\frac{dN}{dE}(\Phi_o, \gamma) = (3.75 \pm_{0.20}^{0.21} \text{ stat} \pm 0.46 \text{ sys}) \times 10^{-11} \left( \frac{E}{1\text{TeV}} \right)^{-2.66 \pm 0.027 \text{ stat} + 0.28 \text{ sys}},$$

with a  $\chi^2$  of 13.47 with 6 degrees of freedom (8 bins - 2 parameters. see fig 5.15 and 5.16). Here, the reduced  $\chi^2$  is greater than two, and so the two parameter model is rejected above 95% confidence as a valid spectral fit for the Crab Nebula as observed with HAWC.

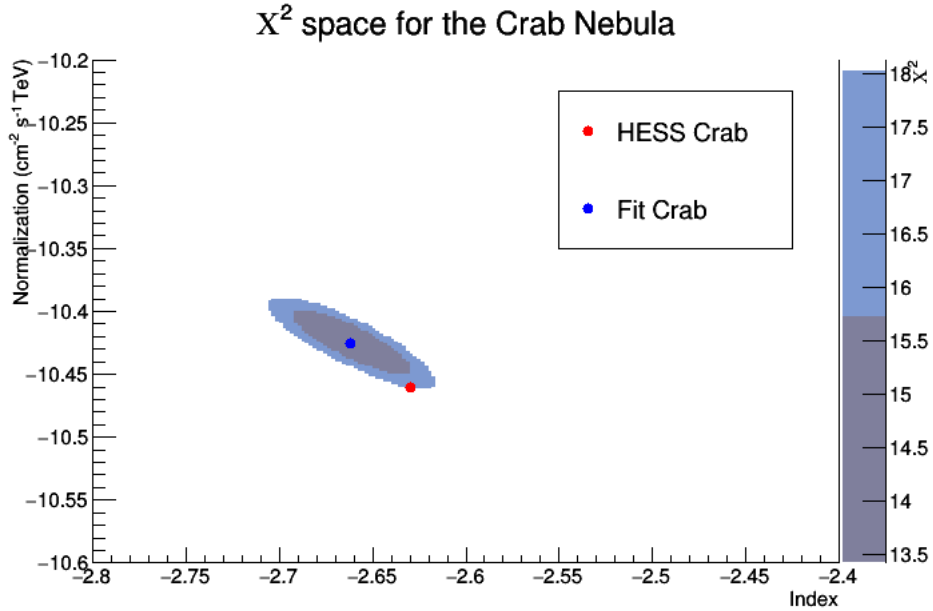


FIGURE 5.15. The  $\chi^2$  space of the Crab nebula as compared to HESS. The dark blue region represents  $1\sigma$  fit uncertainty, and the light blue is  $2\sigma$ .

The linear correlation between index and normalization can be seen in the slope of the  $1$  and  $2\sigma$  regions of  $\chi^2$  space. This can be adjusted by changing the pivot of the spectrum from  $1$  TeV to  $4$  TeV. Recalculating the systematic uncertainties at  $4$  TeV yields systematics of  $\pm$

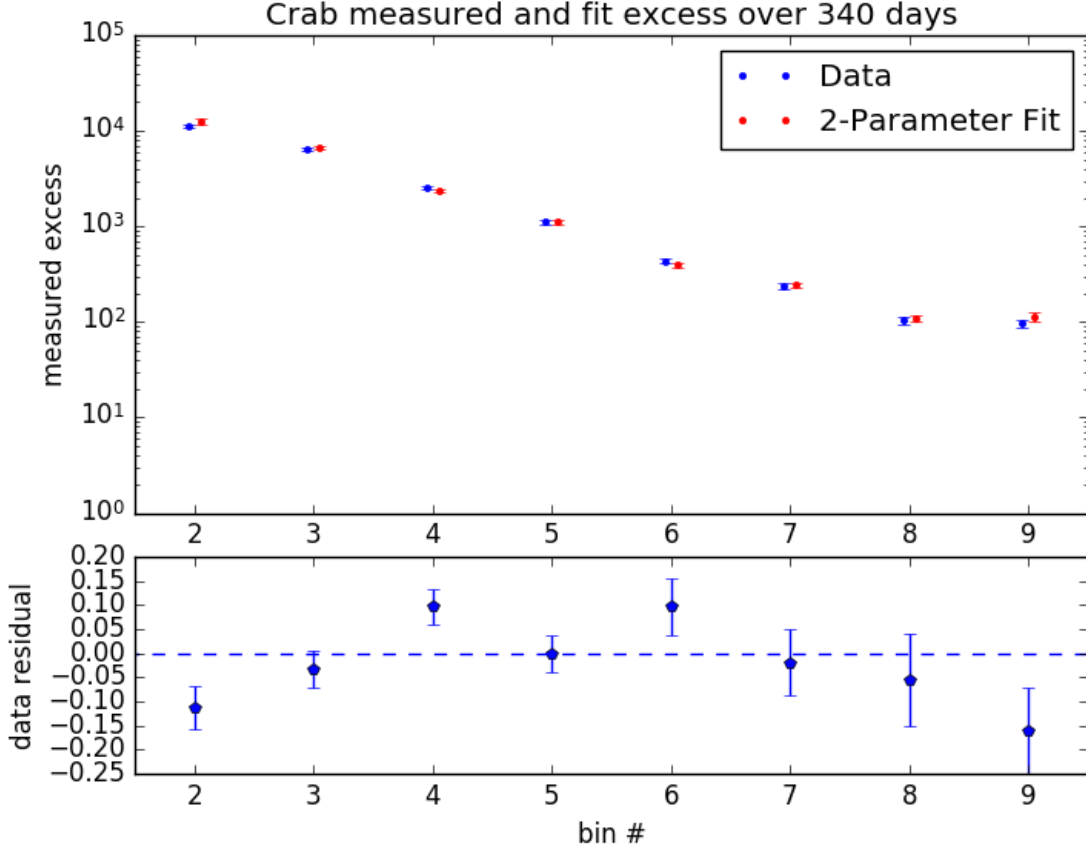


FIGURE 5.16. The resulting fit excess and data excess from HAWC in two parameters (top) and the residual, data-fit/fit (bottom). The error bars on the fit represent the fit results for solutions on the boundary of the  $1\sigma$  contour in  $\chi^2$  space.

18.82% in normalization and  $\pm 11\%$  in index. The resulting spectrum at this new pivot is

$$\frac{dN}{dE}(\Phi_o, \gamma) = (9.375 \pm_{0.28}^{0.28} \text{ stat} \pm 1.8 \text{ sys}) \times 10^{-13} \left( \frac{E}{4\text{TeV}} \right)^{-2.66 \pm 0.030 \text{ stat} \pm 0.29 \text{ sys}},$$

with a  $\chi^2$  of 13.42 with 6 degrees of freedom (8 bins - 2 parameters. see fig 5.17). Again, the two parameter model of the Crab Nebula is rejected above 95% confidence.

Examining the three parameter model at 4 TeV results in a spectrum of

$$\frac{dN}{dE} = (1.03 \pm_{0.083}^{0.091} \text{ stat} \pm 0.19 \text{ sys}) \times 10^{-12} \left( \frac{E}{4\text{TeV}} \right)^{-2.54 \pm 0.095 \text{ stat} \pm 0.27 \text{ sys}} e^{-E/(91.0 \pm_{59}^{174} \text{ stat TeV})},$$

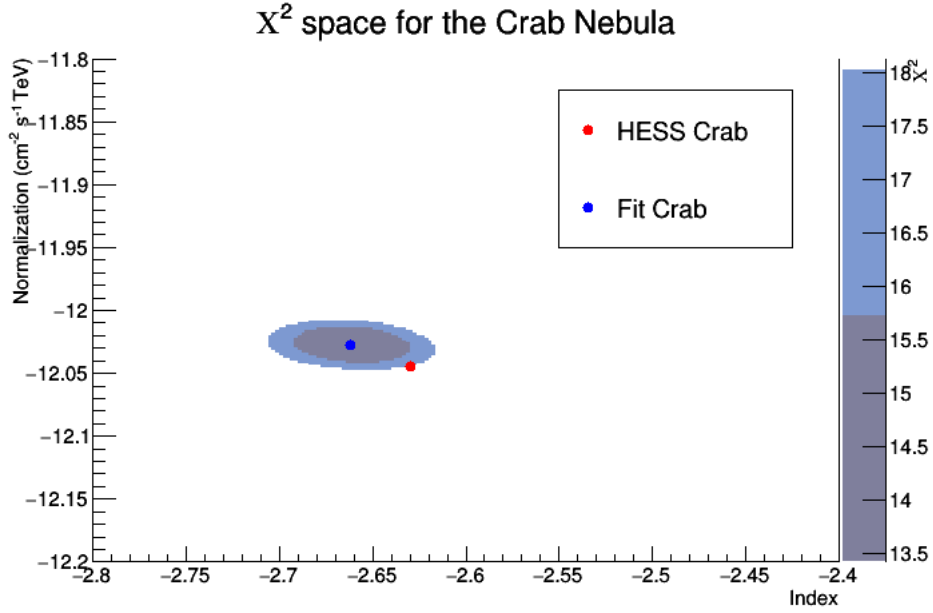


FIGURE 5.17. The  $\chi^2$  space of the Crab nebula as compared to HESS. The dark blue region represents  $1\sigma$  fit uncertainty, and the light blue is  $2\sigma$ .

with a  $\chi^2$  of 5.87 and 5 degrees of freedom (8 bins - 3 parameters, see fig 5.19 and 5.18). This is a reduced  $\chi^2$  of 1.18 and the probability of getting a  $\tilde{\chi}^2$  larger than this is approximately 32%, so there is no reason to doubt that the three parameter model is valid. That said, the cutoff energy is almost certainly untrustworthy, given the large and perhaps unreliable systematics it is subject to. Crosssectional slices of the  $\chi^2$  space which intersect with the solution fail to properly characterize the parameter uncertainties. This is because the solution space is now extended into three dimensions, and the once two dimensional contours are now three dimensional surfaces (see figures 5.20, 5.21, and 5.22).

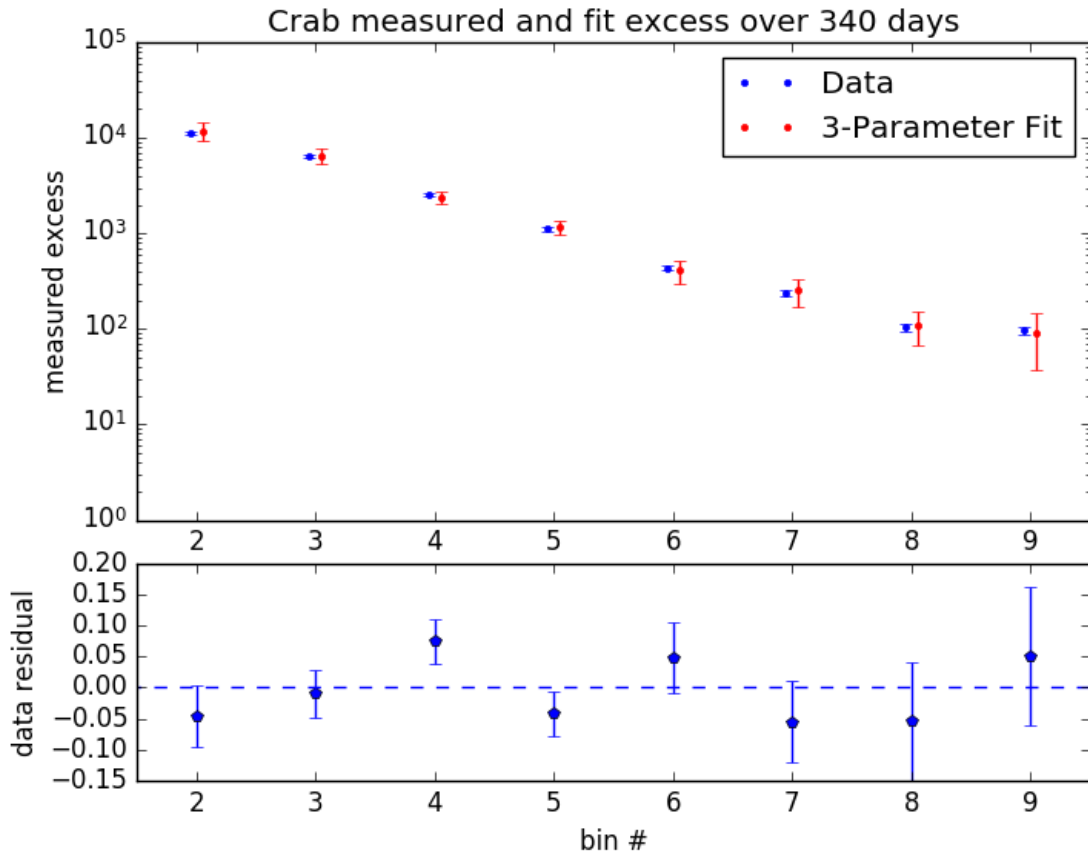


FIGURE 5.18. The resulting fit excess and data excess from HAWC in three parameters (top) and the residual, data-fit/fit (bottom). The error bars on the fit represent the fit results for solutions on the boundary of the  $1\sigma$  contour in  $\chi^2$  space.

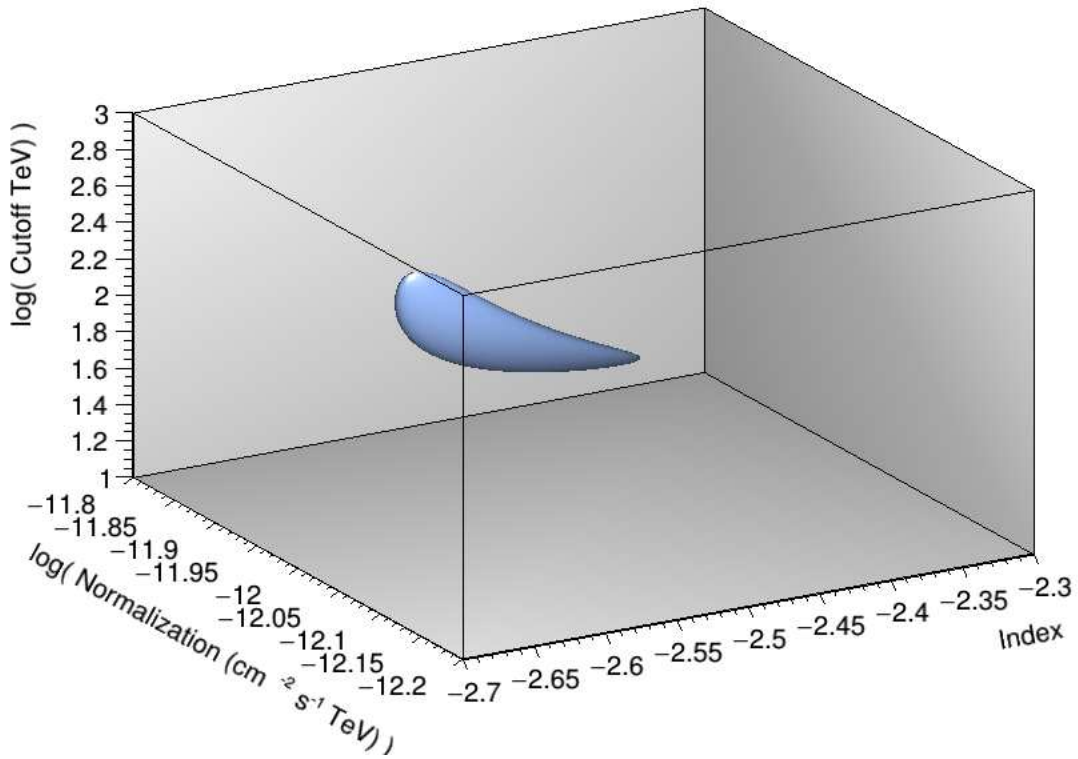


FIGURE 5.19. The  $\chi^2$  space for the three parameter Crab fit. The minimum solution is within the blue surface, which represents 68% uncertainty ( $1 \sigma$ )

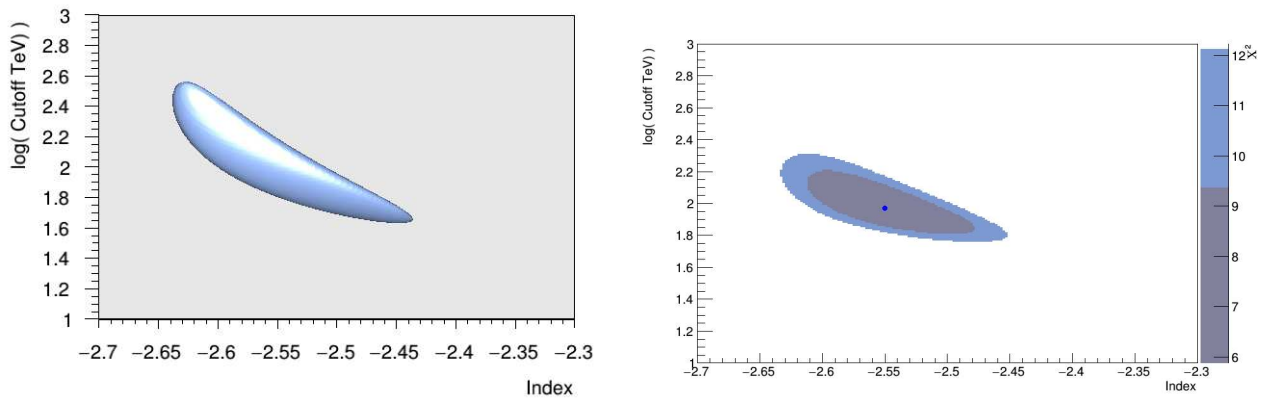


FIGURE 5.20. The  $\chi^2$  space of index versus  $\log(\text{cutoff})$  for the three parameter model as viewed looking along the normalization axis (left) and as viewed with an intersecting plane at the solution (right). The surface is at  $1 \sigma$ , while the intersecting plane shows both  $1 \sigma$  in dark blue and  $2 \sigma$  in light blue.

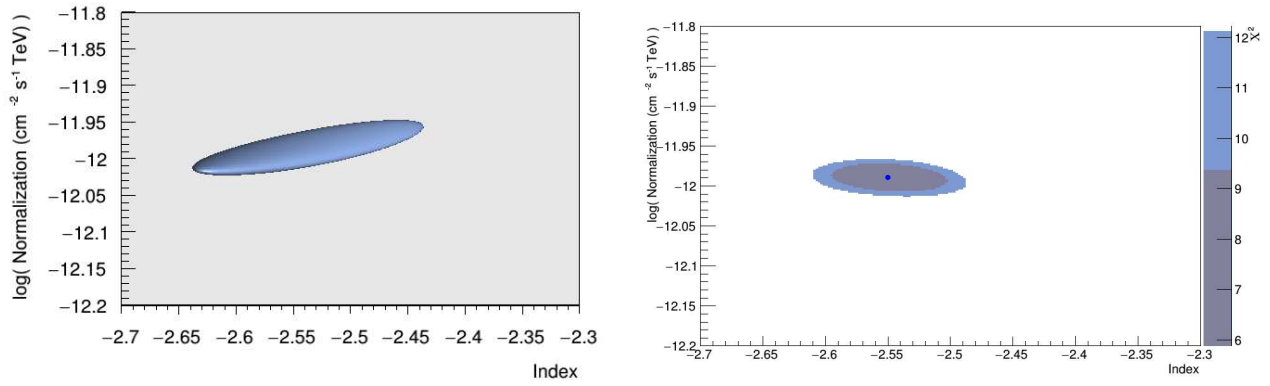


FIGURE 5.21. The  $\chi^2$  space of index versus  $\log(\text{normalization})$  for the three parameter model as viewed looking along the normalization axis (left) and as viewed with an intersecting plane at the solution (right). The surface is at  $1 \sigma$ , while the intersecting plane shows both  $1 \sigma$  in dark blue and  $2 \sigma$  in light blue.

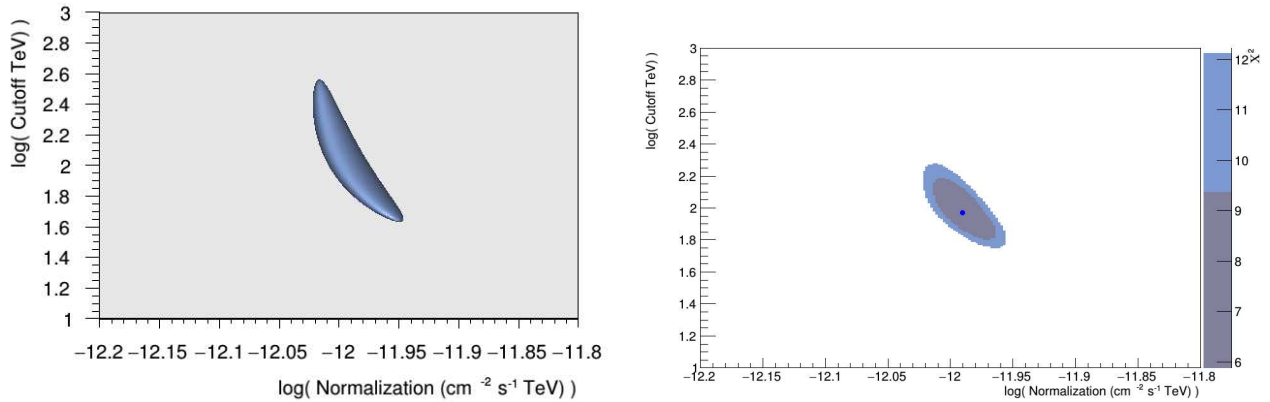


FIGURE 5.22. The  $\chi^2$  space of  $\log(\text{normalization})$  versus  $\log(\text{cutoff})$  for the three parameter model as viewed looking along the normalization axis (left) and as viewed with an intersecting plane at the solution (right). The surface is at  $1 \sigma$ , while the intersecting plane shows both  $1 \sigma$  in dark blue and  $2 \sigma$  in light blue.

## CHAPTER 6

### OTHER SOURCES

With the Crab nebula fit and systematics calculated, this fitting method can be applied to other sources within the field of view of HAWC, again using the HAWC-SP data set. That said, there are two core assumptions to the method described for this analysis which must hold in order for the results to make physical sense. First, the source must be spatially small in extent (point like). If a source is extended (that is, if it subtends a region of the sky more a few tenths of a degree) then the optimal bin calculations and measurements break down, and the simulation will greatly disagree with the data. Second, the source must be steady in time. If a source is transient (that is, the flux of gamma rays from the source wildly changes in time), then scaling the simulations in time (which are per transit) will not accurately represent the flux from the source, even if the source is significant on the sky.

Hotspots that are isolated enough can be explicitly named based on the nearest single source. If a source cannot be named either because it is too close to several known sources or because it is not near any known sources, it is designated by the prefix HAWC followed by the location of the hotspot in right ascension and declination to the nearest 0.01 degree (for example, HAWC12345-6789 is a hot spot located at (123.45,-67.89) in J2000 equatorial. This designation scheme is not the designation scheme used by the collaboration for confirmed sources. This is because the analysis makes no claim as to whether or not a hotspot is actually a source.

The top ten most significant hotspots observed with HAWC were fit using forward folding. The hotspot in the region of Geminga was also fit, as this is currently a source of interest to the collaboration.

## 6.1. MARKARIAN 421

Markarian galaxies are a class of galaxies first described and studied by Benjamin Markarian in 1963. All Markarian galaxies are characterized by the presence of intense ultraviolet radiation far exceeding that of other galaxies. Markarian 421 (or Mrk421) is a blazar located in the constellation of Ursa Major, between 122 Mpc and 133 Mpc from earth (making it one of the closest known blazars). Markarian 421 stands out as a source candidate because the spectrum of Mrk421 extends well into the TeV range. That said, Mrk421 is prone to intense intermittent flaring, and even outside of these flares, the flux of Mrk421 is still highly variable. For this analysis, Mrk421 was detected with a significance of  $32\sigma$  at  $(166.16^\circ, 38.21^\circ)$  J2000 equatorial (see figures 6.1 6.2 and 6.4). Bins 2 through 9 were used and the resulting 2 parameter spectrum was

$$\frac{dN}{dE}(\Phi_o, \gamma) = (4.79 \pm_{0.54}^{0.61} \text{ stat} \pm 0.90 \text{ sys}) \times 10^{-13} \left( \frac{E}{4\text{TeV}} \right)^{-3.26 \pm 0.045 \text{ stat} \pm 0.36 \text{ sys}},$$

with a  $\chi^2$  of 16.77 and 6 degrees of freedom (8 bins - 2 parameters), which rejects the 2 parameter model. Note that the  $\chi^2$  region is very small. This means that the region around the minimum value is very “deep”, not that the fit is particularly good. In three parameters the spectrum is

$$\frac{dN}{dE} = (1.23 \pm_{0.91}^{3.6} \text{ stat} \pm 0.23 \text{ sys}) \times 10^{-12} \left( \frac{E}{4\text{TeV}} \right)^{-2.61 \pm 0.39 \text{ stat} \pm 0.28 \text{ sys}} e^{-E/(6.4 \pm_{4.3}^{12} \text{ stat TeV})},$$

with a  $\chi^2$  of 4.74 with 5 degrees of freedom (8 bins - 3 parameters, see figures 6.5, 6.6, 6.7, and 6.8).

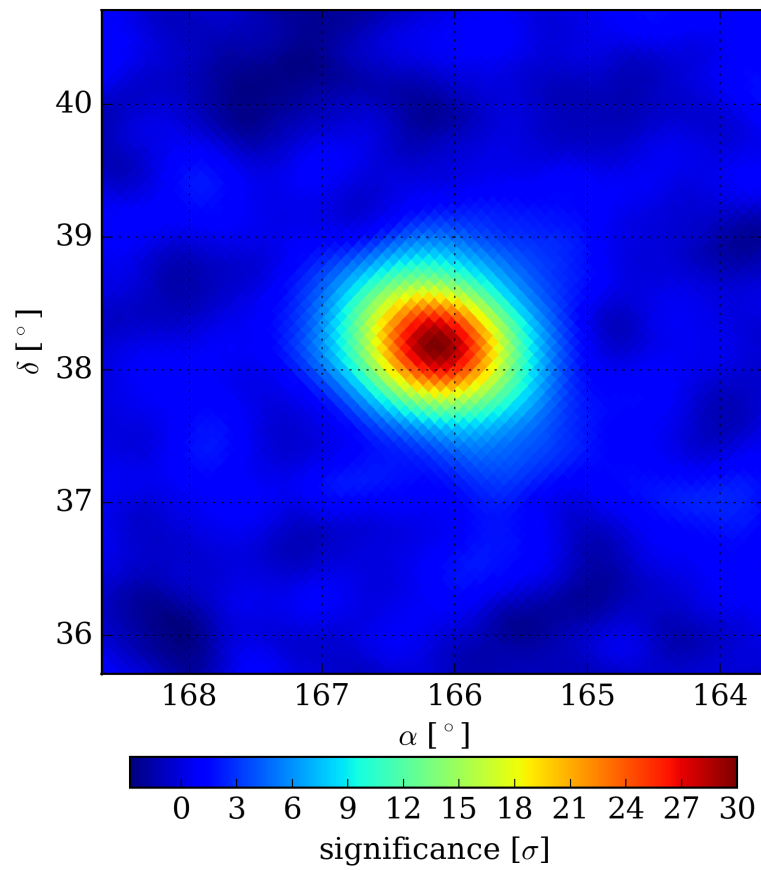


FIGURE 6.1. The blazar Markarian 421 as seen with the HAWC observatory.

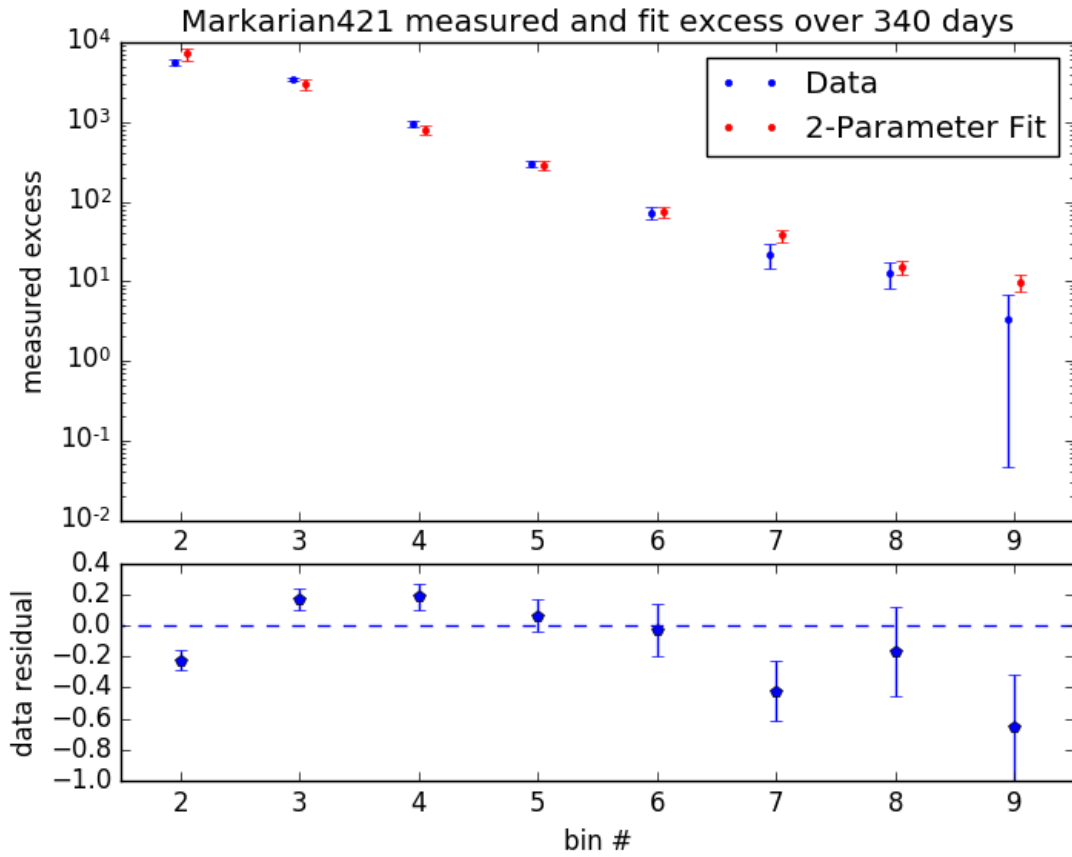


FIGURE 6.2. The measured excess form Markarian 421 and the fit spectrum in two parameters. The error bars on the fit represent the fit results for solutions on the boundary of the  $1\sigma$  contour in  $\chi^2$  space.

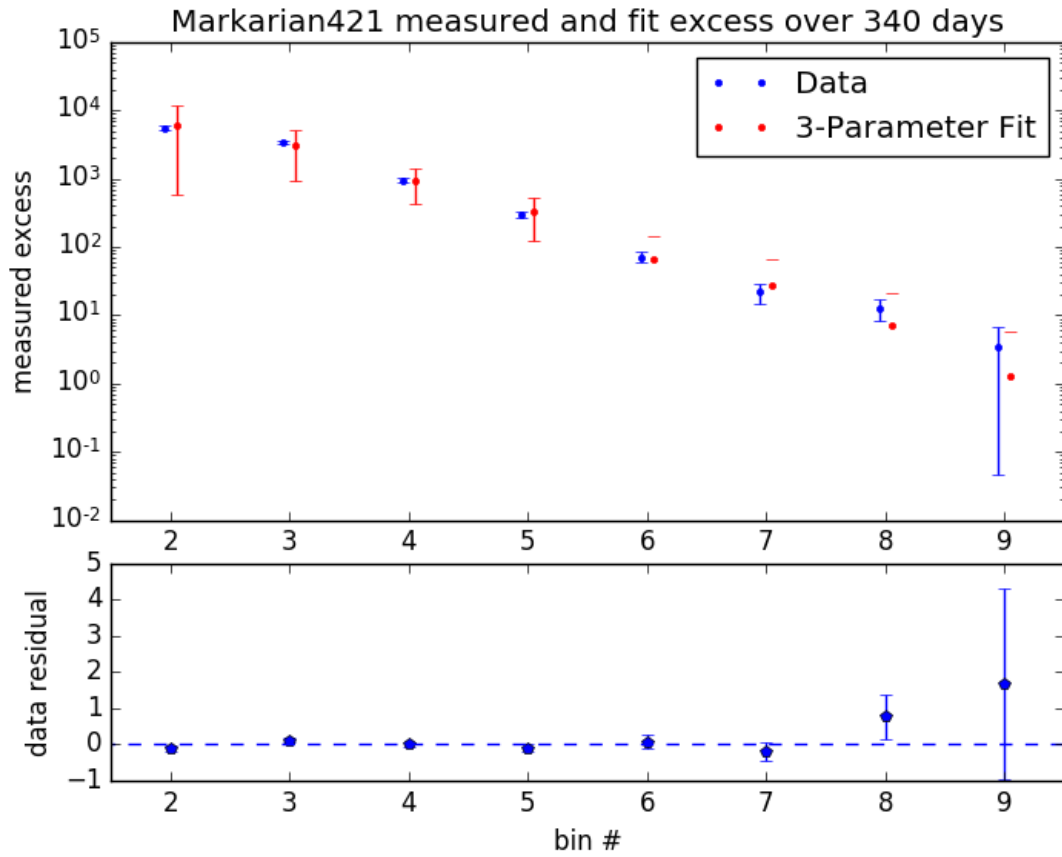


FIGURE 6.3. The measured excess from Markarian 421 and the fit spectrum in three parameters (top) and the residual, data-fit/fit (bottom). If an error bar is not present it means that the uncertainty extends to 0. The error bars on the fit represent the fit results for solutions on the boundary of the  $1\sigma$  contour in  $\chi^2$  space.

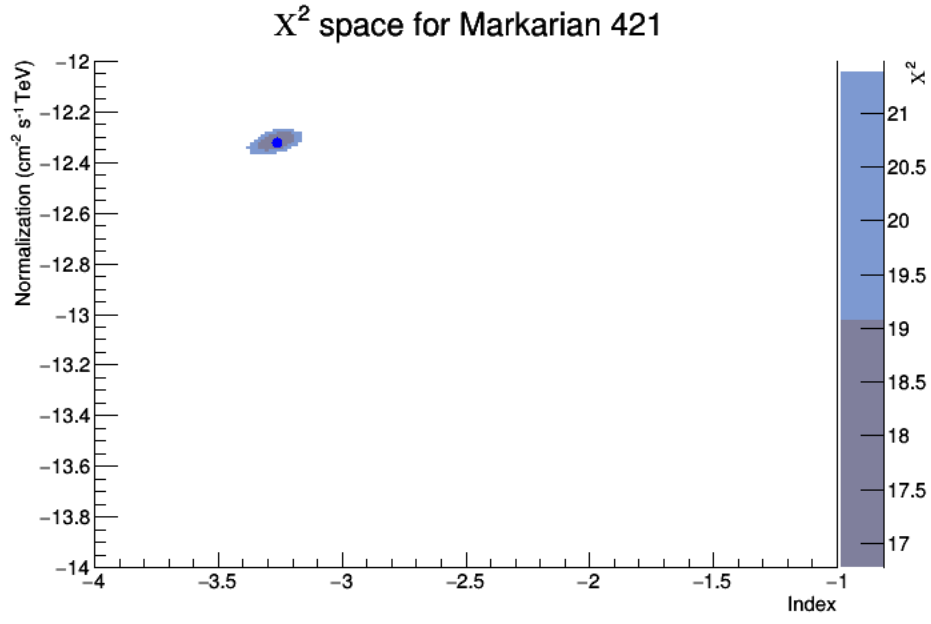


FIGURE 6.4. The  $\chi^2$  space for the fit of Markarian 421. Dark blue is  $1 \sigma$  uncertainty, and light blue is  $2 \sigma$ .

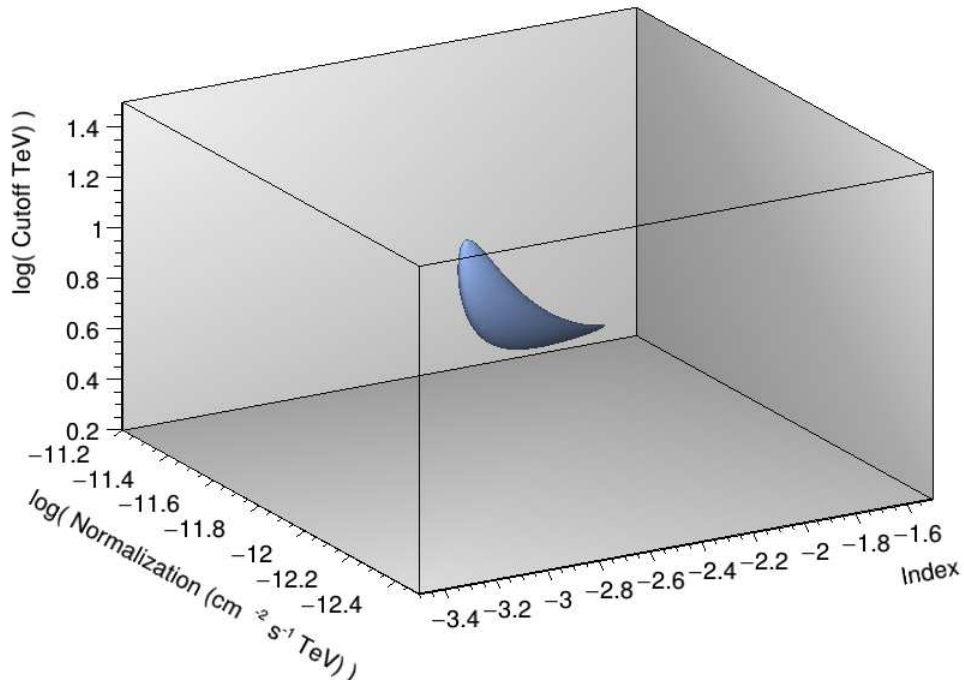


FIGURE 6.5. The  $\chi^2$  space for the three parameter fit of Markarian 421. The minimum solution is within the blue surface, which represents 68% uncertainty ( $1 \sigma$ )

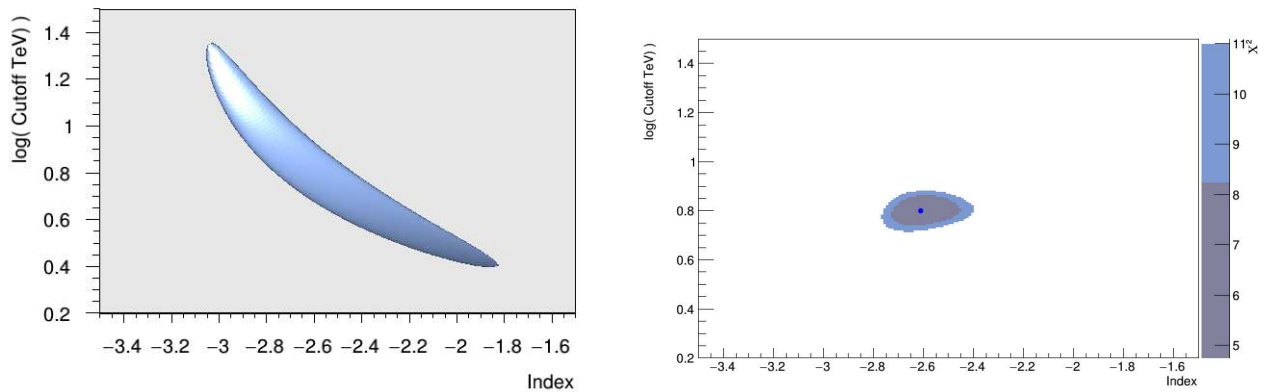


FIGURE 6.6. The  $\chi^2$  space of index versus  $\log(\text{cutoff})$  for Markarian 421 fit with the three parameter model as viewed looking along the normalization axis (left) and as viewed with an intersecting plane at the solution (right). The surface is at  $1 \sigma$ , while the intersecting plane shows both  $1 \sigma$  in dark blue and  $2 \sigma$  in light blue.

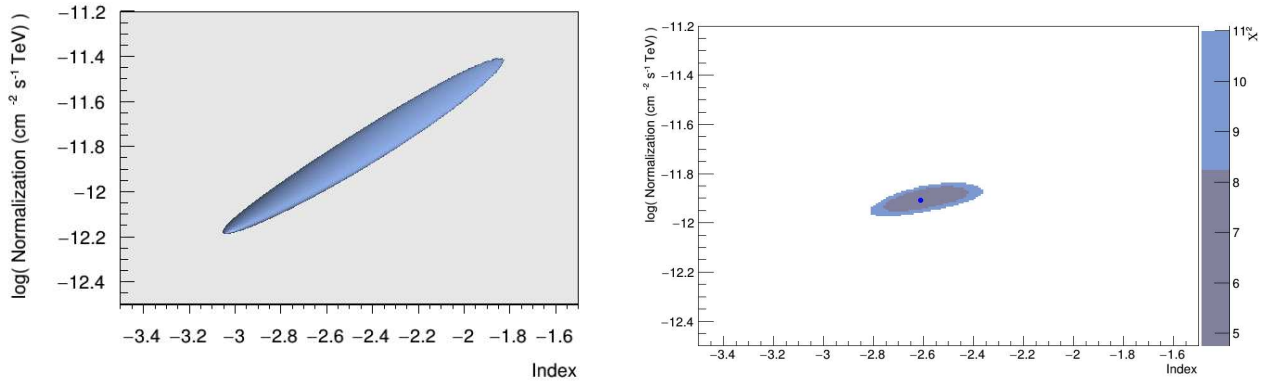


FIGURE 6.7. The  $\chi^2$  space of index versus  $\log(\text{normalization})$  for Markarian 421 fit with the three parameter model as viewed looking along the normalization axis (left) and as viewed with an intersecting plane at the solution (right). The surface is at  $1\sigma$ , while the intersecting plane shows both  $1\sigma$  in dark blue and  $2\sigma$  in light blue.

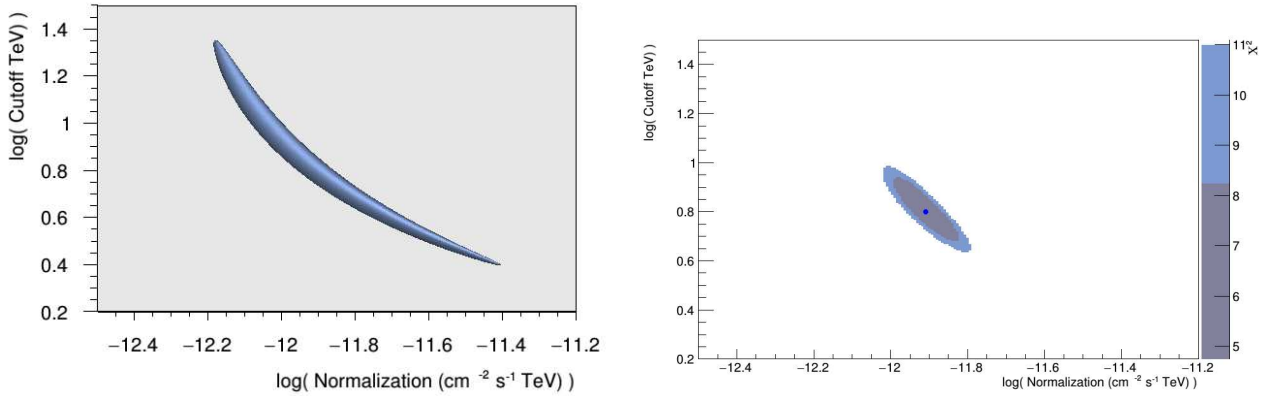


FIGURE 6.8. The  $\chi^2$  space of  $\log(\text{normalization})$  versus  $\log(\text{cutoff})$  for Markarian 421 fit with the three parameter model as viewed looking along the normalization axis (left) and as viewed with an intersecting plane at the solution (right). The surface is at  $1\sigma$ , while the intersecting plane shows both  $1\sigma$  in dark blue and  $2\sigma$  in light blue.

## 6.2. MARKARIAN 501

Markarian 501 is another Markarian class galaxy. It, like Markarian 421, is a blazar that is highly variable in the TeV range and is prone to flaring. Markarian 501 is located in the constellation of Hercules, and for this analysis it was detected with a significance of  $21.7\sigma$  at  $(253.48^\circ, 39.79^\circ)$  J2000 equatorial (see figs.6.9 6.10 and 6.12). Bins 2 through 9 were used and the resulting fit spectrum was

$$\frac{dN}{dE}(\Phi_o, \gamma) = (3.16 \pm_{0.45}^{0.53} \text{ stat} \pm 0.69 \text{ sys}) \times 10^{-13} \left( \frac{E}{4\text{TeV}} \right)^{-3.06 \pm 0.065 \text{ stat} \pm 0.33 \text{ sys}},$$

with a  $\chi^2$  of 16.16 and 6 degrees of freedom (8 bins - 2 parameters), which rejects the 2 parameter model at a confidence of 95% or more. In three parameters, the spectrum is

$$\frac{dN}{dE} = (7.25 \pm_{2.8}^{4.7} \text{ stat} \pm 1.4 \text{ sys}) \times 10^{-13} \left( \frac{E}{4\text{TeV}} \right)^{-2.19 \pm 0.31 \text{ stat} \pm 0.24 \text{ sys}} e^{-E/(7.94 \pm_{5.3}^{16} \text{ stat TeV})},$$

with a minimum  $\chi^2$  of 2.66 with 5 degrees of freedom (8 bins - three parameters, see figures 6.13, 6.14, 6.15, and 6.16).

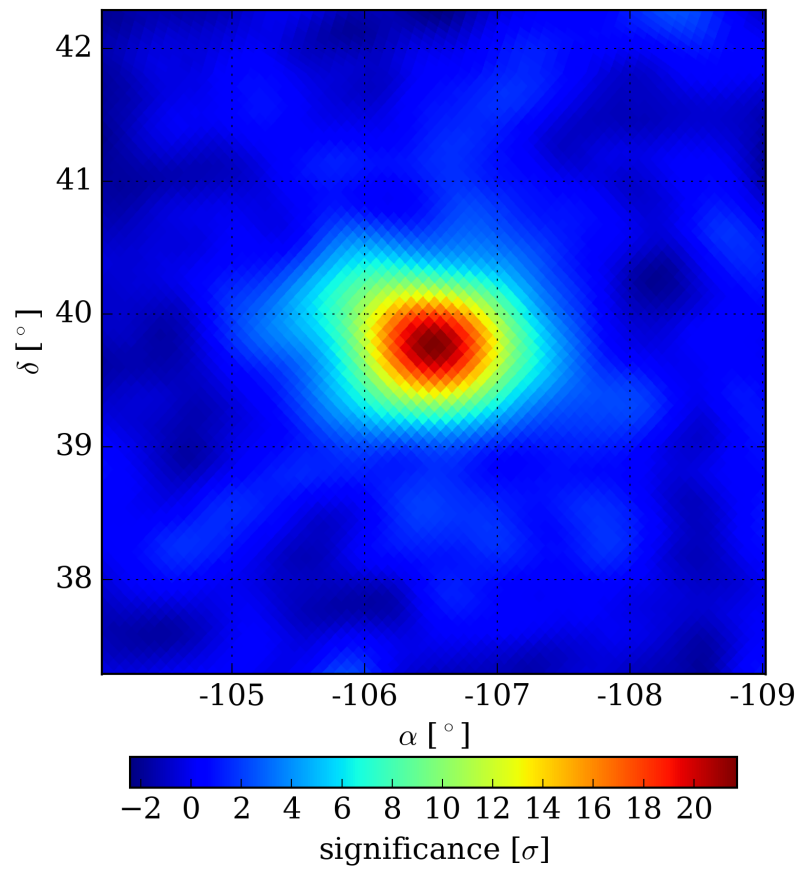


FIGURE 6.9. The blazar Markarian 501 as seen with the HAWC observatory.

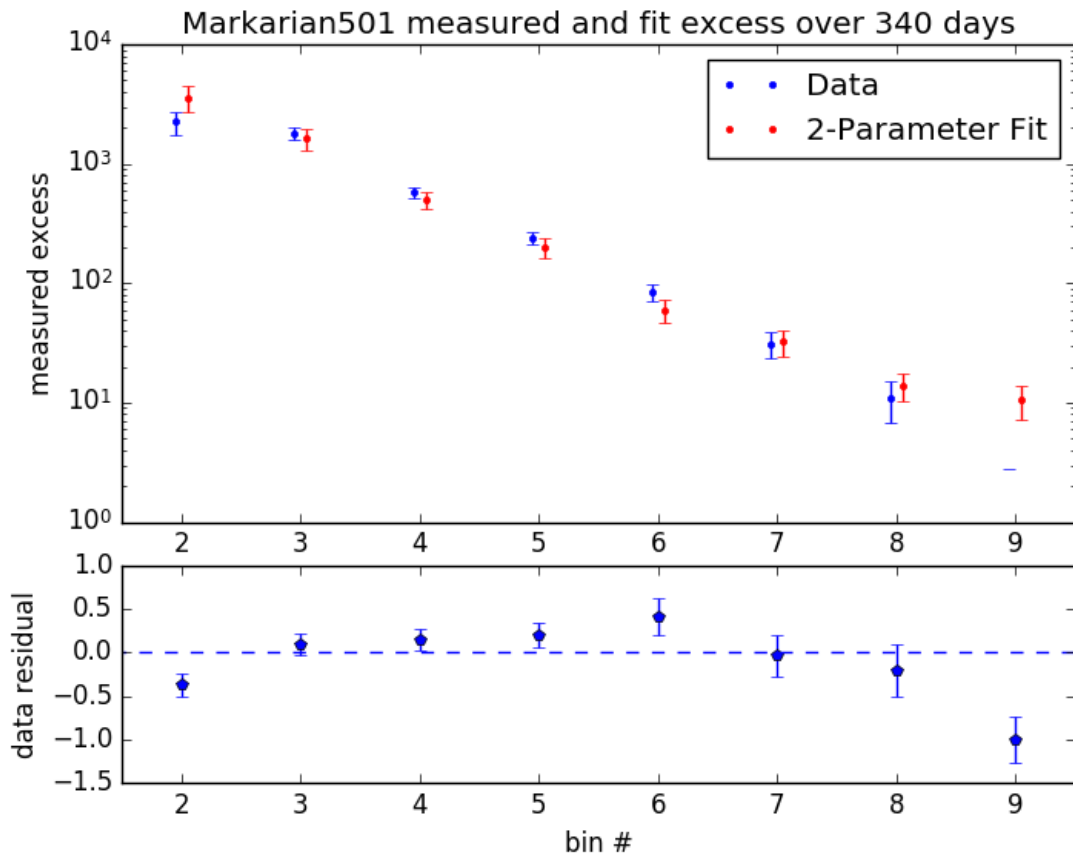


FIGURE 6.10. The measured excess from Markarian 501 and the fit spectrum in two parameters. The error bars on the fit represent the fit results for solutions on the boundary of the  $1\sigma$  contour in  $\chi^2$  space.

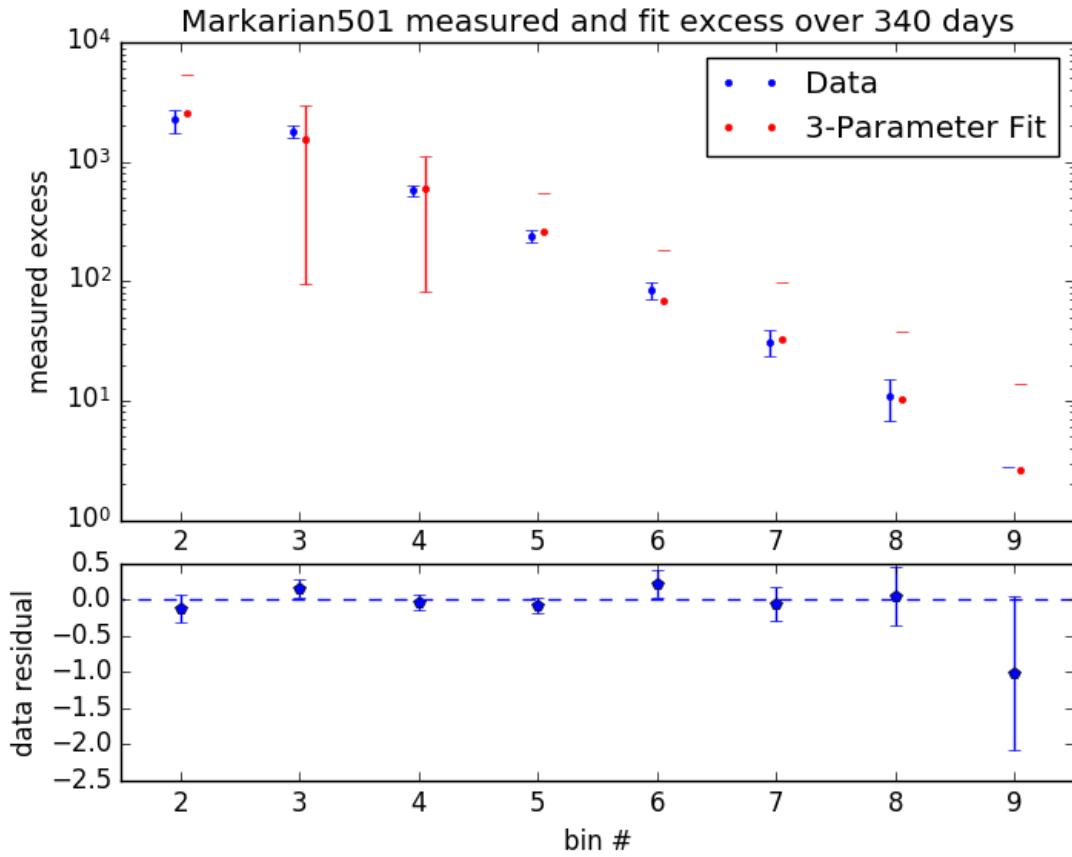


FIGURE 6.11. The measured excess from Markarian 501 and the fit spectrum in three parameters (top) and the residual, data-fit/fit (bottom). If an error bar is not present it means that the uncertainty extends to 0. The error bars on the fit represent the fit results for solutions on the boundary of the  $1\sigma$  contour in  $\chi^2$  space.

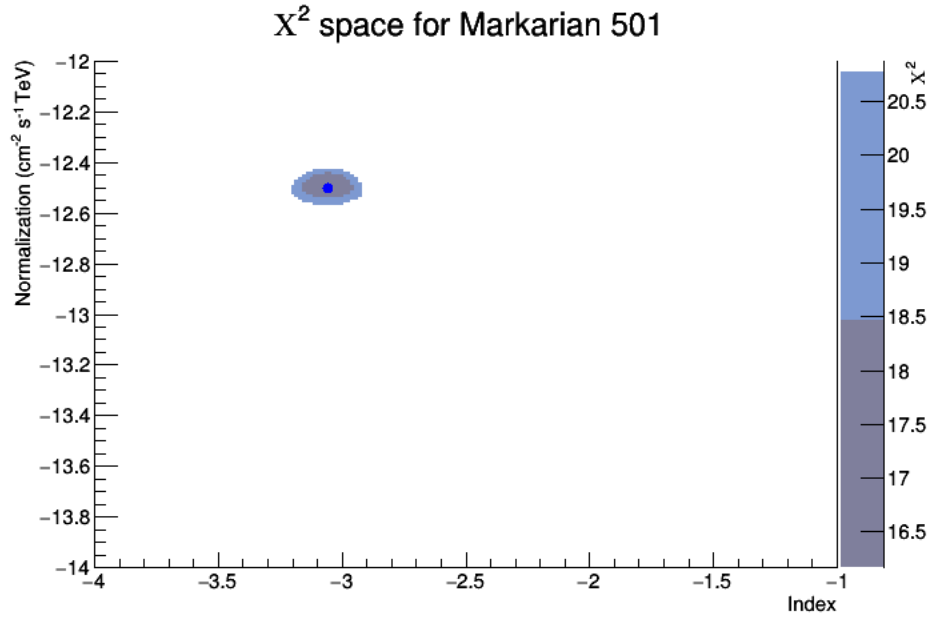


FIGURE 6.12. The  $\chi^2$  space for the fit of Markarian 501. Dark blue is  $1 \sigma$  uncertainty, and light blue is  $2 \sigma$ .

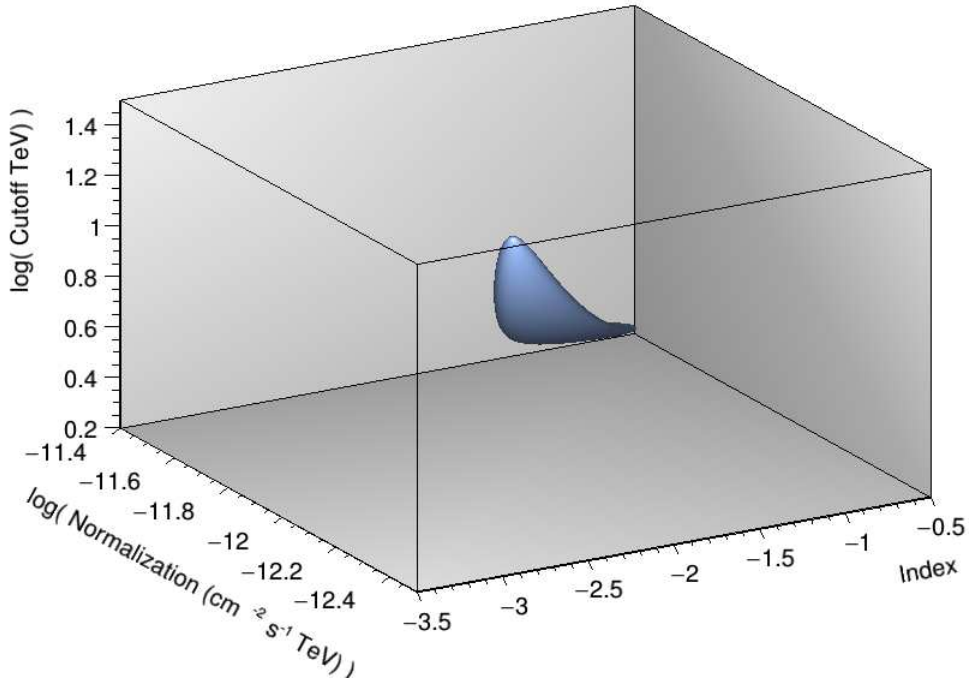


FIGURE 6.13. The  $\chi^2$  space for the three parameter fit for Markarian 501. The minimum solution is within the blue surface, which represents 68% uncertainty ( $1\sigma$ )

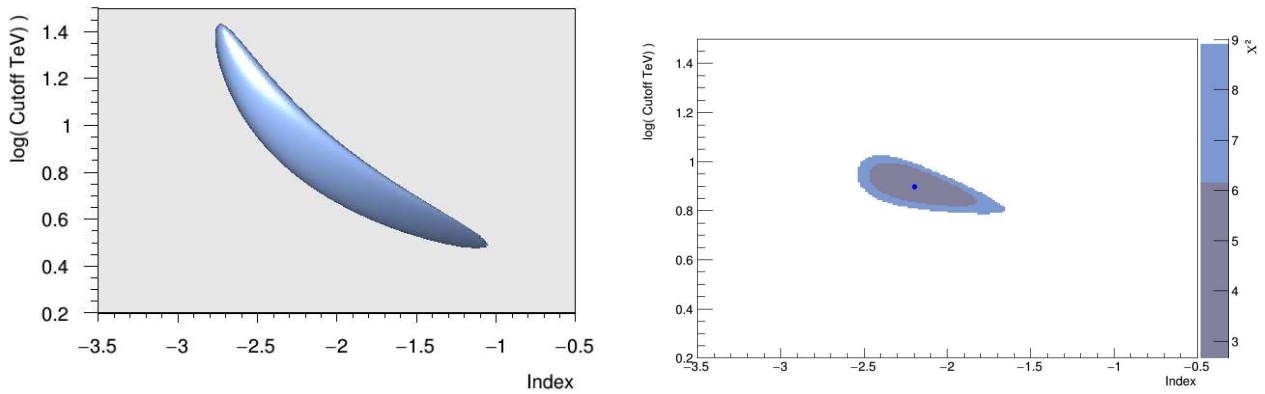


FIGURE 6.14. The  $\chi^2$  space of index versus  $\log(\text{cutoff})$  for Markarian 501 fit with the three parameter model as viewed looking along the normalization axis (left) and as viewed with an intersecting plane at the solution (right). The surface is at  $1\sigma$ , while the intersecting plane shows both  $1\sigma$  in dark blue and  $2\sigma$  in light blue.

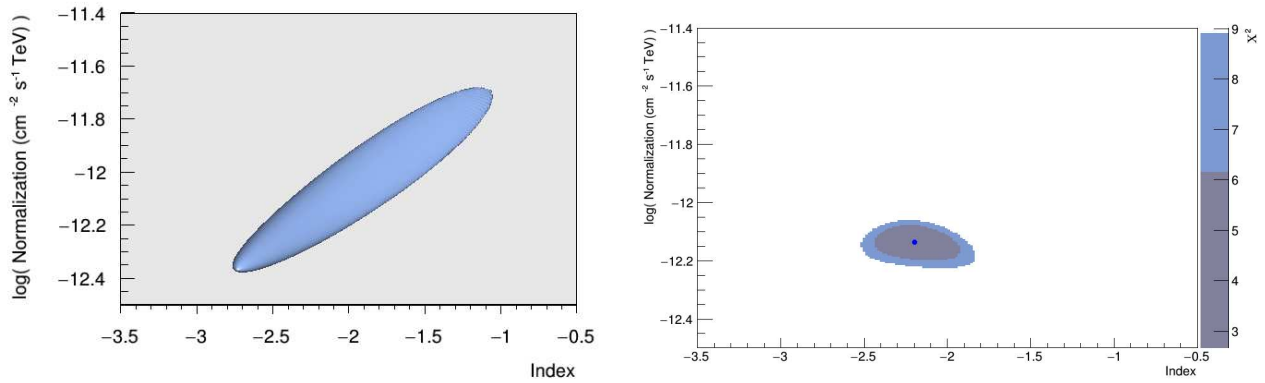


FIGURE 6.15. The  $\chi^2$  space of index versus  $\log(\text{normalization})$  for Markarian 501 fit with the three parameter model as viewed looking along the normalization axis (left) and as viewed with an intersecting plane at the solution (right). The surface is at  $1 \sigma$ , while the intersecting plane shows both  $1 \sigma$  in dark blue and  $2 \sigma$  in light blue.

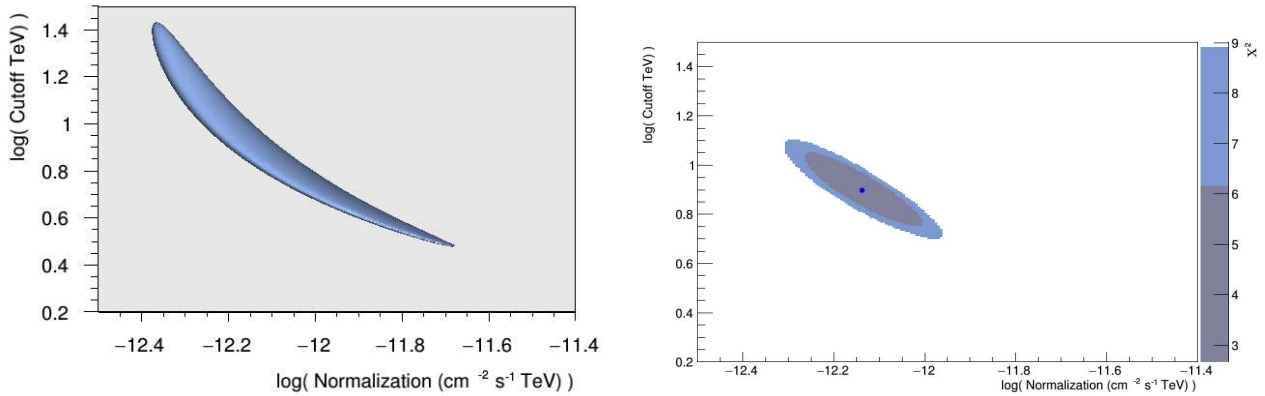


FIGURE 6.16. The  $\chi^2$  space of  $\log(\text{normalization})$  versus  $\log(\text{cutoff})$  for Markarian 501 fit with the three parameter model as viewed looking along the normalization axis (left) and as viewed with an intersecting plane at the solution (right). The surface is at  $1 \sigma$ , while the intersecting plane shows both  $1 \sigma$  in dark blue and  $2 \sigma$  in light blue.

### 6.3. HAWC27646-1340

Hotspot HAWC27646-1340 is closest in proximity to PWN HESSJ1825-137. It was detected at  $19.32\sigma$  and fit using bins 2-9 (see figs. 6.17, 6.18, and 6.19), resulting in a spectrum of

$$\frac{dN}{dE}(\Phi_o, \gamma) = (6.61 \pm_{1.6}^{2.3} \text{ stat} \pm 1.2 \text{ sys}) \times 10^{-13} \left( \frac{E}{4\text{TeV}} \right)^{-2.86 \pm 0.12 \text{ stat} \pm 0.31 \text{ sys}},$$

with a  $\chi^2$  of 5.2 and 6 degrees of freedom (8 bins - 2 parameters).

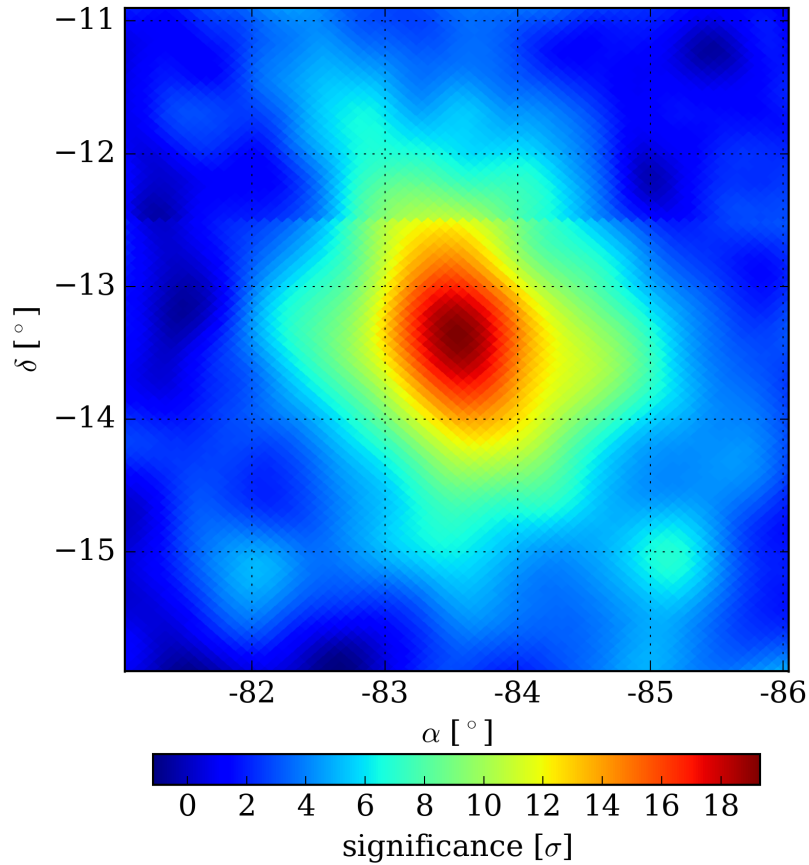


FIGURE 6.17. The hotspot HAWC27646-1340 as seen with the HAWC observatory.

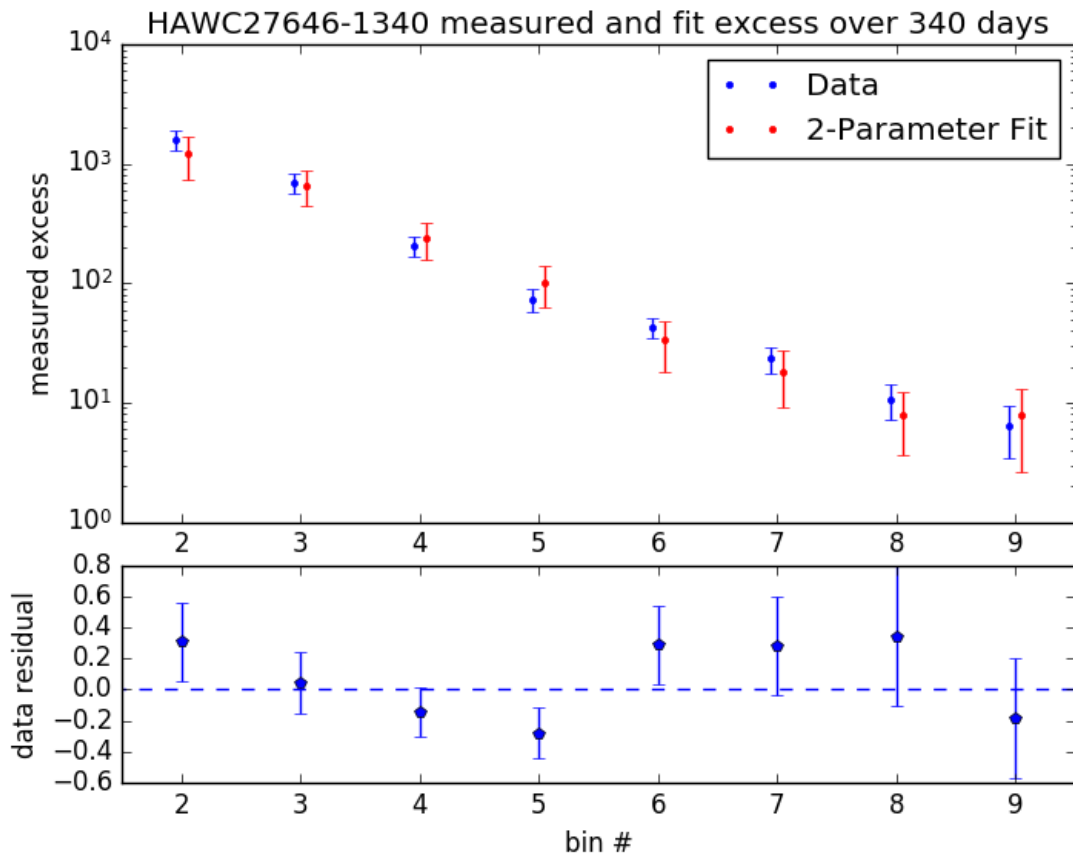


FIGURE 6.18. The measured excess form HAWC27646-1340 and the fit spectrum (top) and the residual, data-fit/fit (bottom).

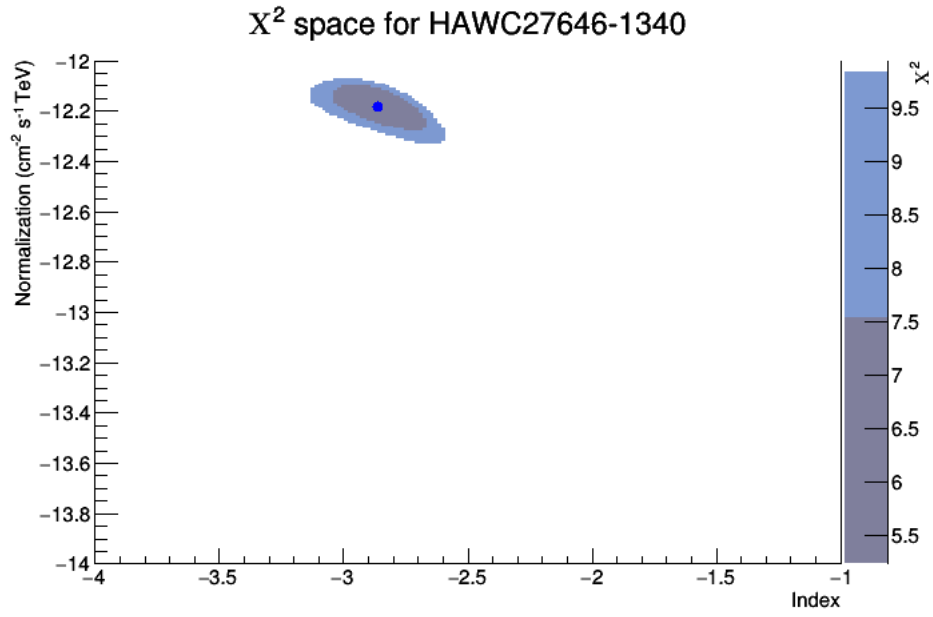


FIGURE 6.19. The  $\chi^2$  space for the fit of HAWC27646-1340. Dark blue is 1  $\sigma$  uncertainty, and light blue is 2  $\sigma$ .

#### 6.4. HAWC27936-0665

Hotspot HAWC27936-0665 is closest in proximity to PWN HESS J1837-069. It was detected at  $17.72\sigma$  and fit using bins 2-9 (see figs. 6.20, 6.21, and 6.22), resulting in a spectrum of

$$\frac{dN}{dE}(\Phi_o, \gamma) = (2.63 \pm_{0.53}^{0.66} \textit{stat} \pm 0.49 \textit{sys}) \times 10^{-13} \left( \frac{E}{4\text{TeV}} \right)^{-3.09 \pm 0.10 \textit{stat} \pm 0.34 \textit{sys}},$$

with a  $\chi^2$  of 10.02 and 6 degrees of freedom (8 bins - 2 parameters).

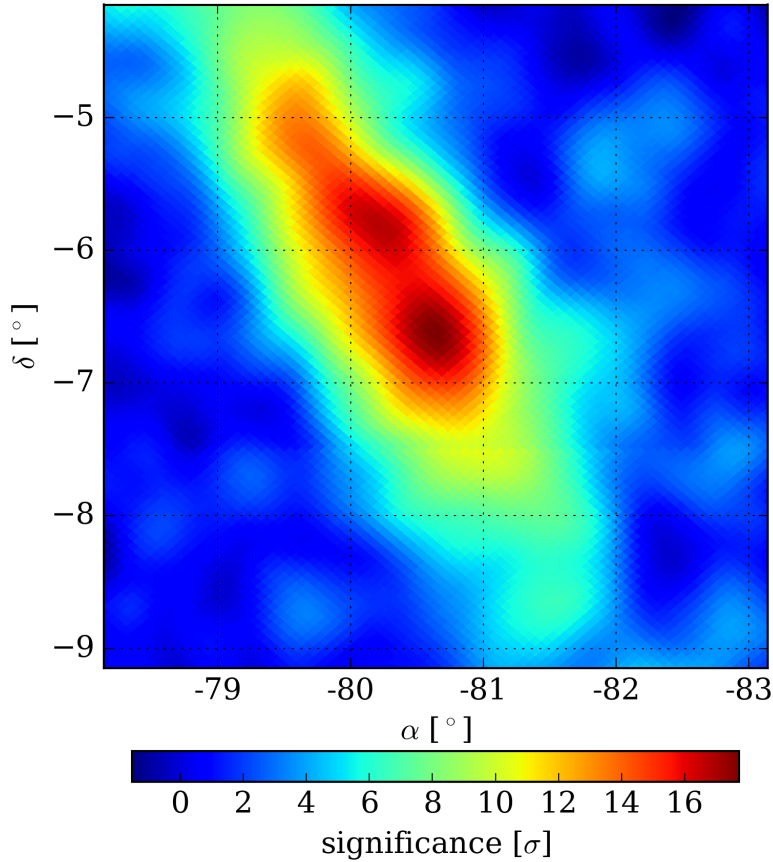


FIGURE 6.20. The hotspot HAWC27936-0665 as seen with the HAWC observatory.

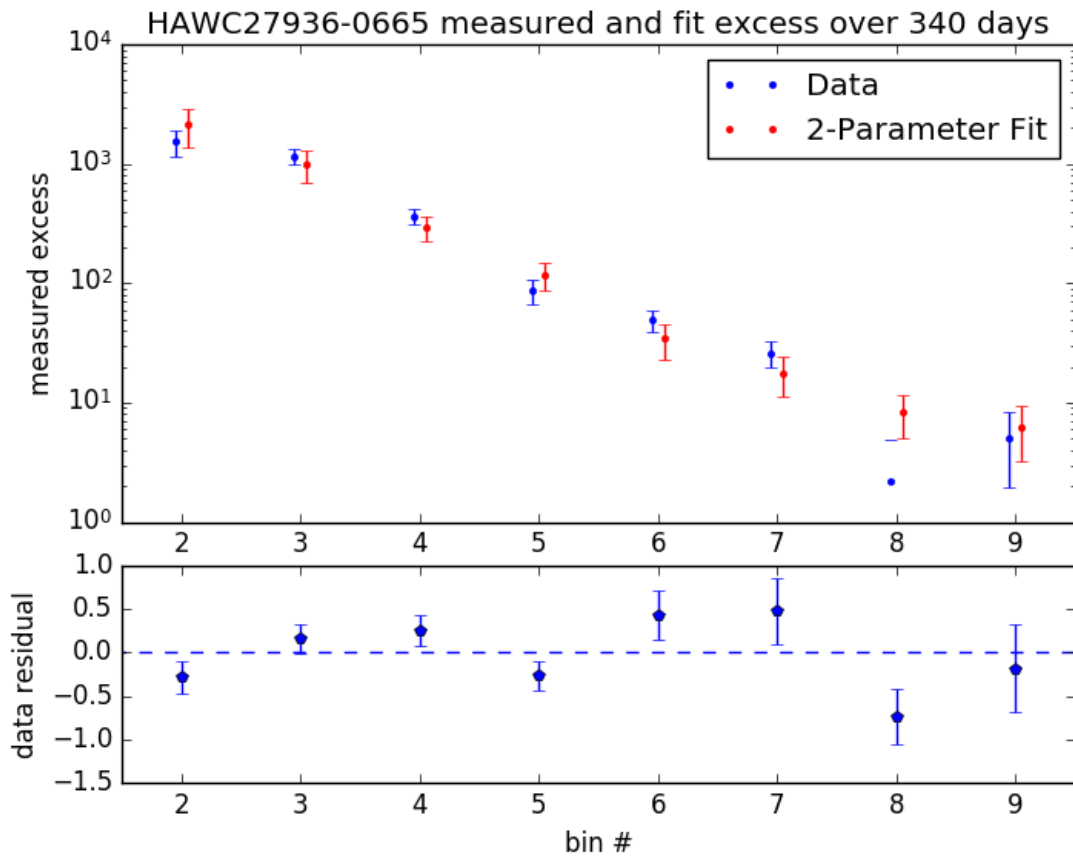


FIGURE 6.21. The measured excess form HAWC27936-0665 and the fit spectrum (top) and the residual, data-fit/fit (bottom).

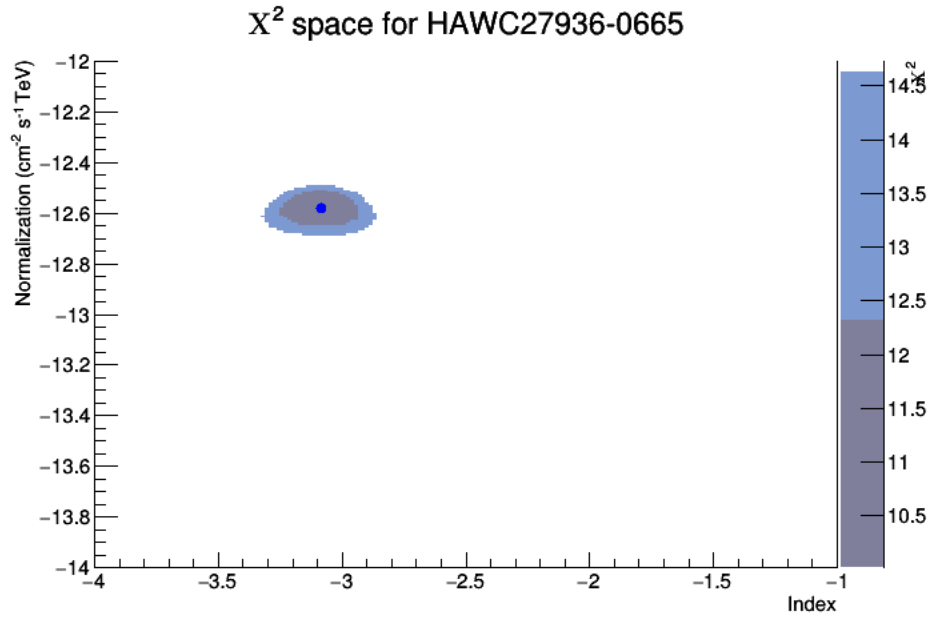


FIGURE 6.22. The  $\chi^2$  space for the fit of HAWC27936-0665. Dark blue is 1  $\sigma$  uncertainty, and light blue is 2  $\sigma$ .

## 6.5. HAWC27980-0583

Hotspot HAWC27980-0583 is closest in proximity to the unidentified source HESS J1841-055. It was detected at  $16.77\sigma$  and fit using bins 2-9 (see figs. 6.23, 6.24, and 6.25), resulting in a spectrum of

$$\frac{dN}{dE}(\Phi_o, \gamma) = (2.51 \pm_{0.54}^{0.69} \text{ stat} \pm 0.47 \text{ sys}) \times 10^{-13} \left( \frac{E}{4\text{TeV}} \right)^{-3.09 \pm 0.14 \text{ stat} \pm 0.34 \text{ sys}},$$

with a  $\chi^2$  of 6.21 and 6 degrees of freedom (8 bins - 2 parameters).

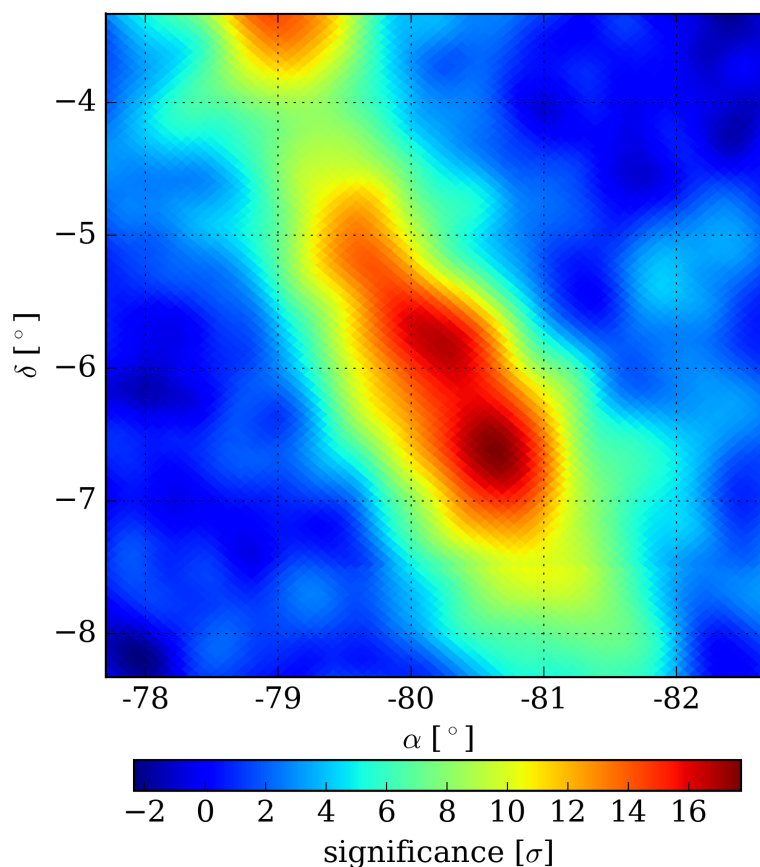


FIGURE 6.23. The hotspot HAWC27980-0583 as seen with the HAWC observatory.

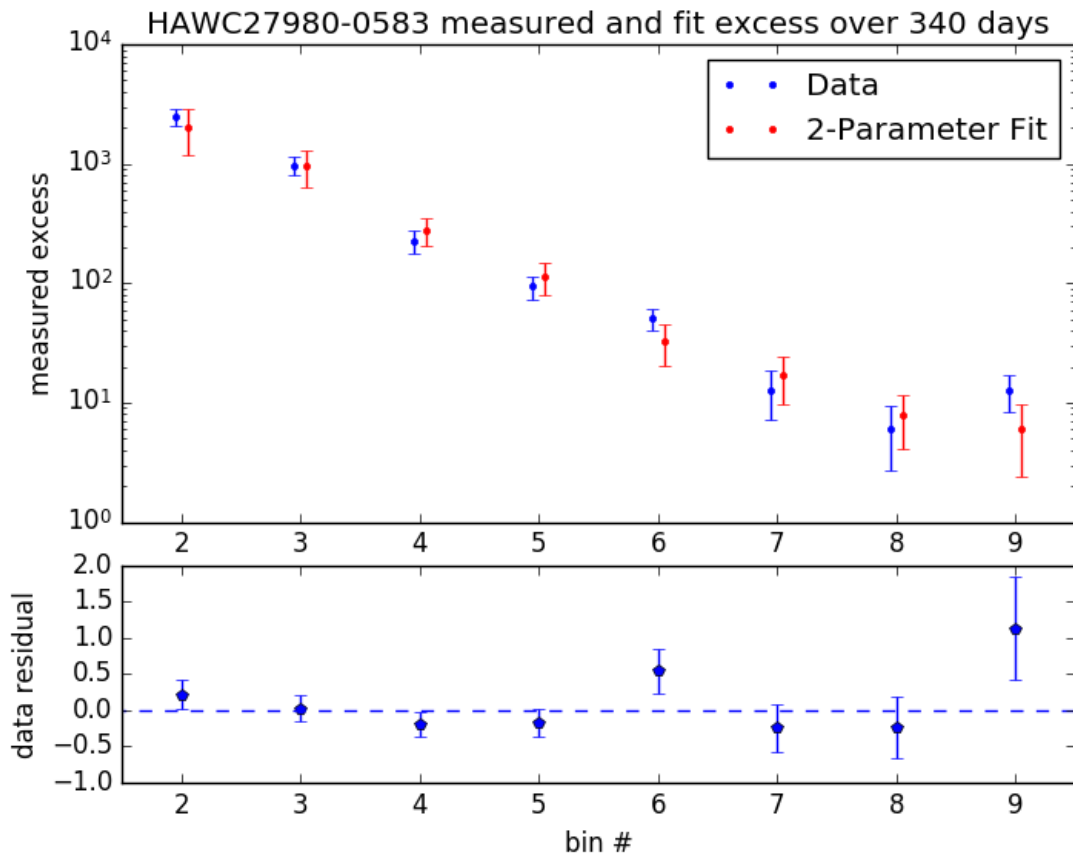


FIGURE 6.24. The measured excess form HAWC27980-0583 and the fit spectrum (top) and the residual, data-fit/fit (bottom).

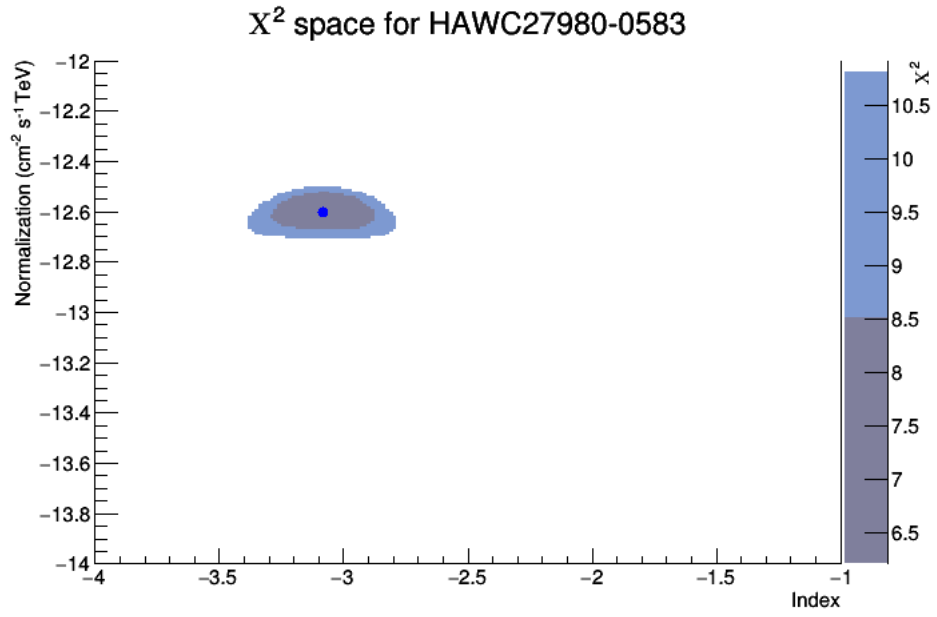


FIGURE 6.25. The  $\chi^2$  space for the fit of HAWC27980-0583. Dark blue is  $1 \sigma$  uncertainty, and light blue is  $2 \sigma$ .

## 6.6. HAWC28107-0332

Hotspot HAWC28107-0332 is closest in proximity to both the unidentified HESS J1843-033 and J1844-030. It was detected at  $14.33\sigma$  and fit using bins 2-9 (see figs. 6.26, 6.27, and 6.28) resulting in a spectrum of

$$\frac{dN}{dE}(\Phi_o, \gamma) = (2.09 \pm_{0.63}^{0.91} \text{ stat} \pm 0.39 \text{ sys}) \times 10^{-13} \left( \frac{E}{4\text{TeV}} \right)^{-2.82 \pm 0.13 \text{ stat} \pm 0.31 \text{ sys}},$$

with a  $\chi^2$  of 0.59 and 6 degrees of freedom (8 bins - 2 parameters).

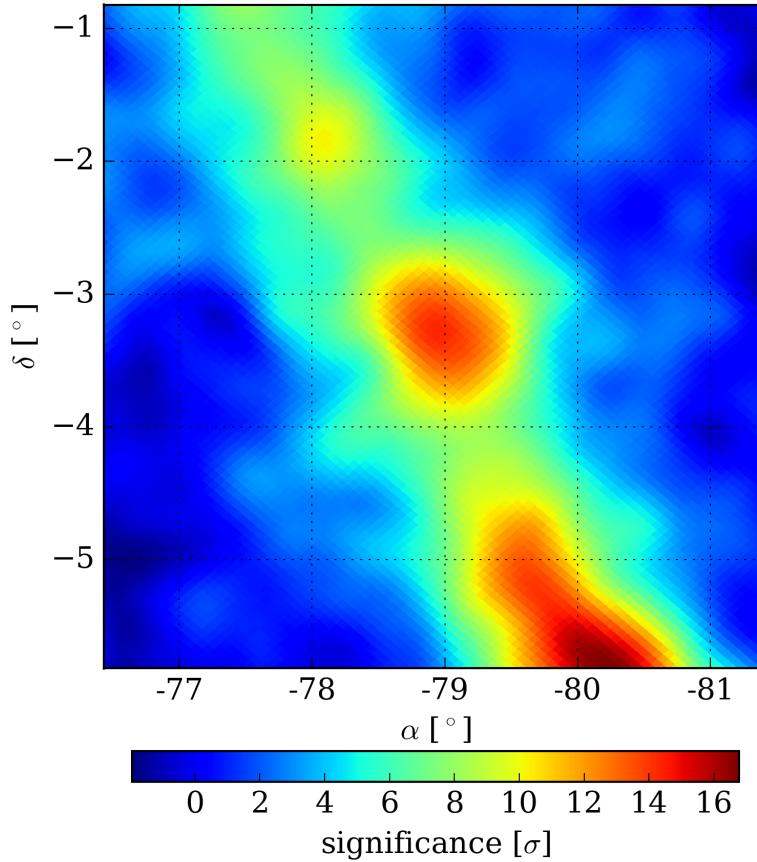


FIGURE 6.26. The hotspot HAWC28107-0332 as seen with the HAWC observatory.

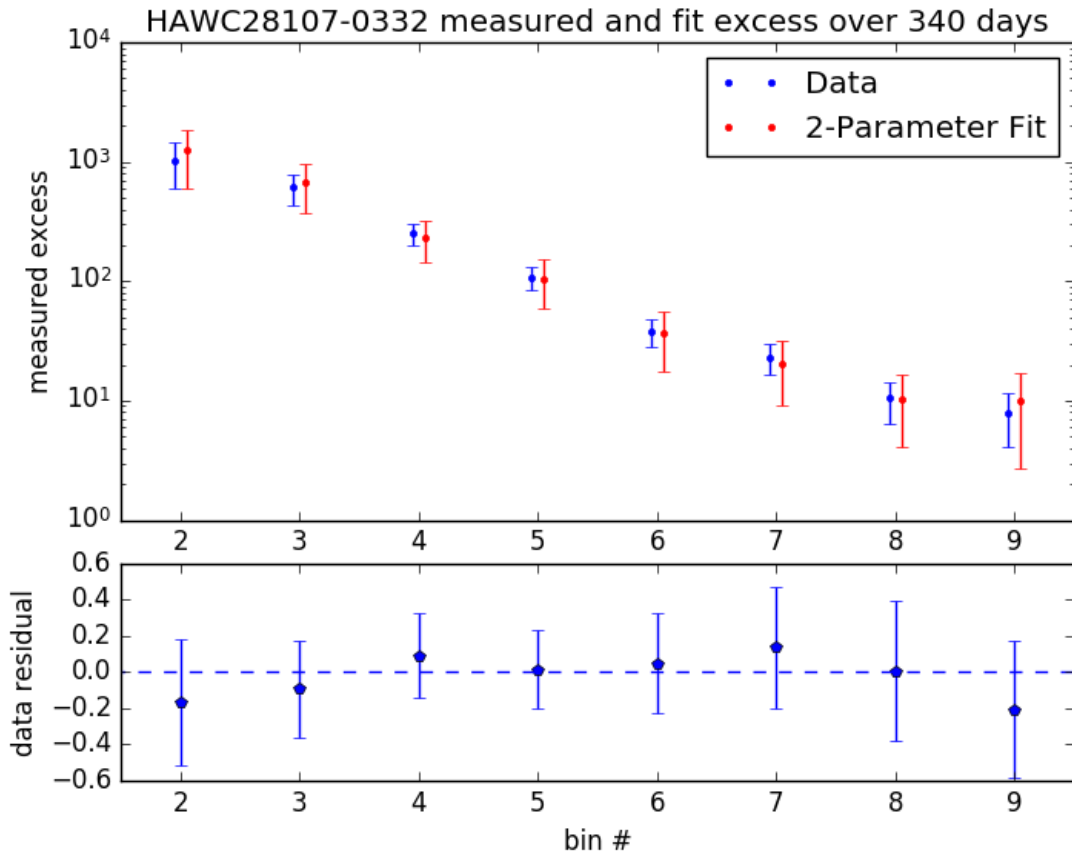


FIGURE 6.27. The measured excess form HAWC28107-0332 and the fit spectrum (top) and the residual, data-fit/fit (bottom).

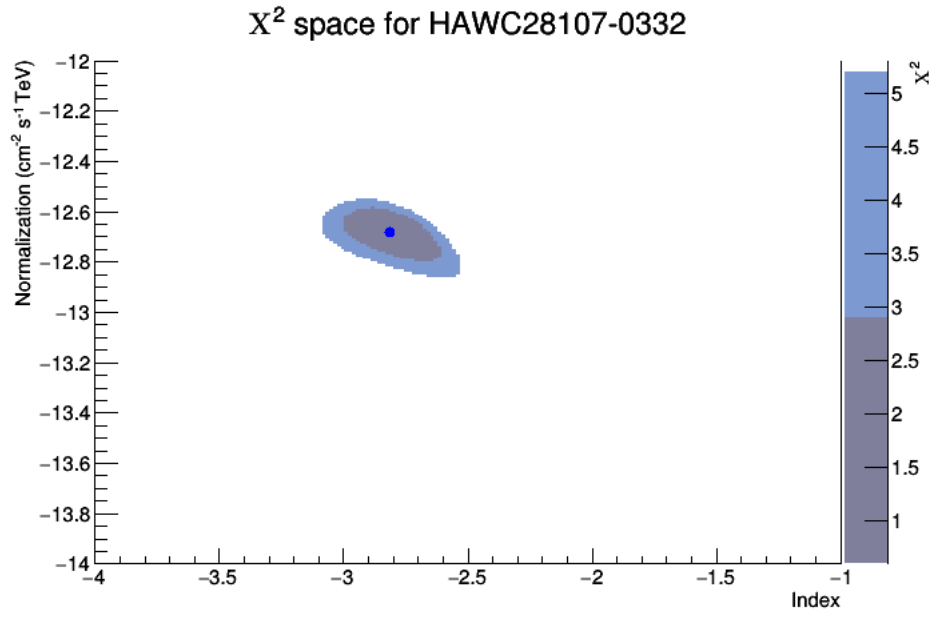


FIGURE 6.28. The  $\chi^2$  space for the fit of HAWC28107-0332. Dark blue is 1  $\sigma$  uncertainty, and light blue is 2  $\sigma$ .

## 6.7. HAWC28433+0280

Hotspot HAWC28433+0280 is closest in proximity to HESS J1857+026. It was detected at  $14.26\sigma$  and fit using bins 2-9 (see figs. 6.29, 6.30, and 6.31), resulting in a spectrum of

$$\frac{dN}{dE}(\Phi_o, \gamma) = (1.45 \pm_{0.35}^{0.46} \text{ stat} \pm 0.27 \text{ sys}) \times 10^{-13} \left( \frac{E}{4\text{TeV}} \right)^{-3.05 \pm 0.12 \text{ stat} \pm 0.34 \text{ sys}},$$

with a  $\chi^2$  of 3.81 and 6 degrees of freedom (8 bins - 2 parameters).

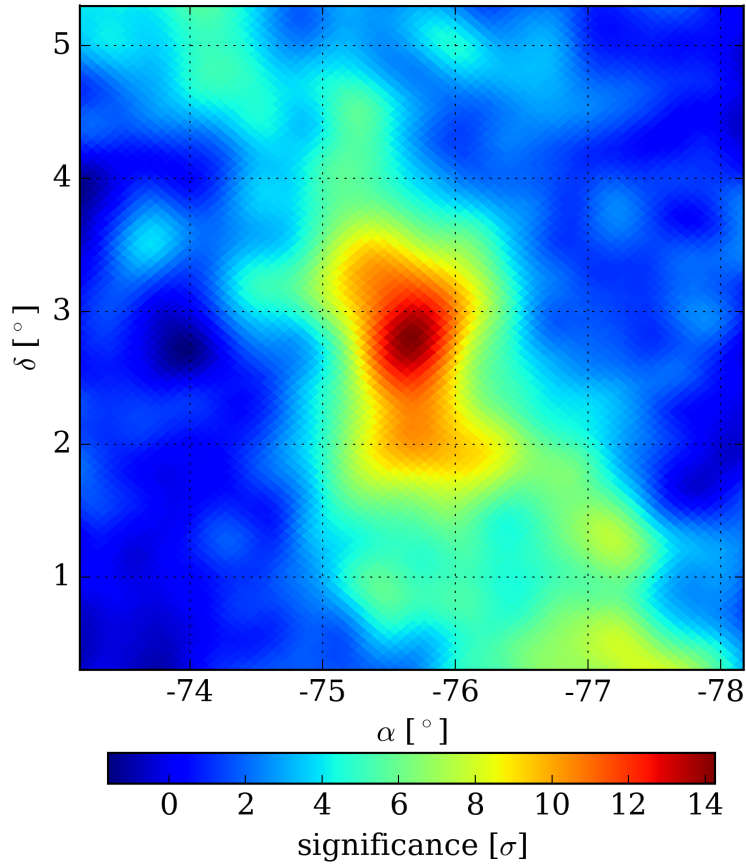


FIGURE 6.29. The hotspot HAWC28433+0280 as seen with the HAWC observatory.

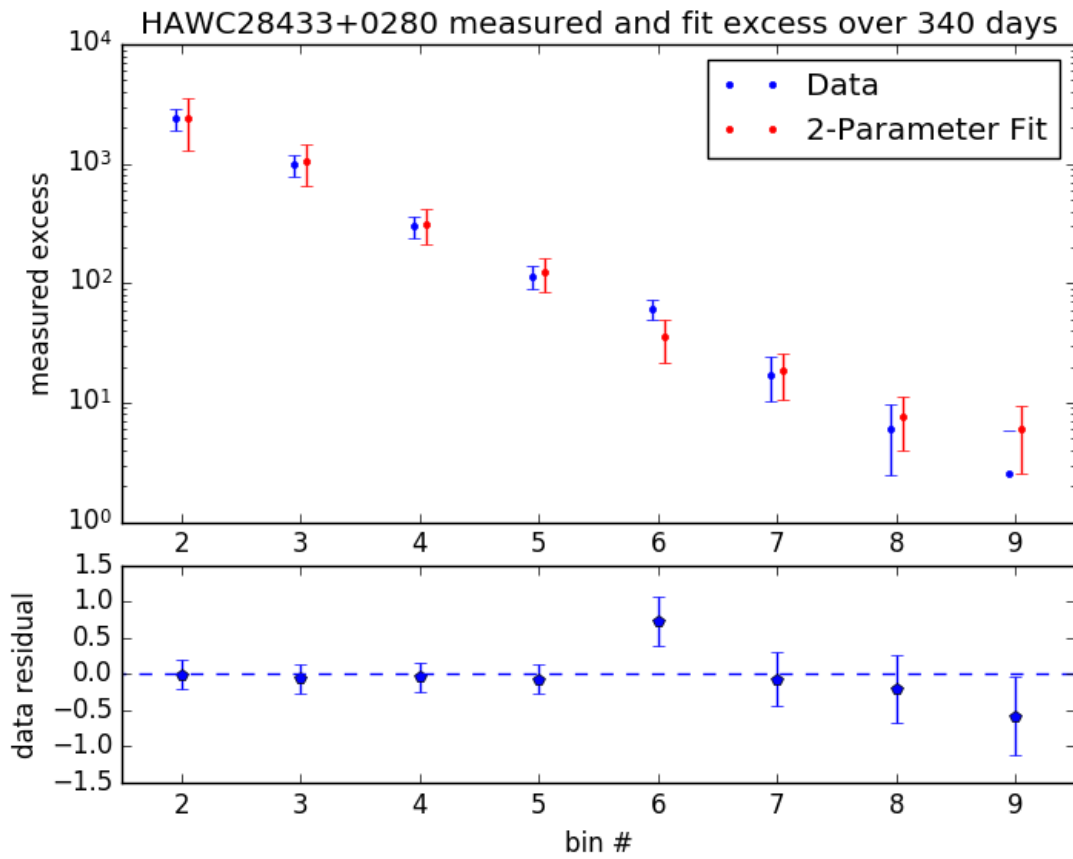


FIGURE 6.30. The measured excess form HAWC28433+0280 and the fit spectrum (top) and the residual, data-fit/fit (bottom).

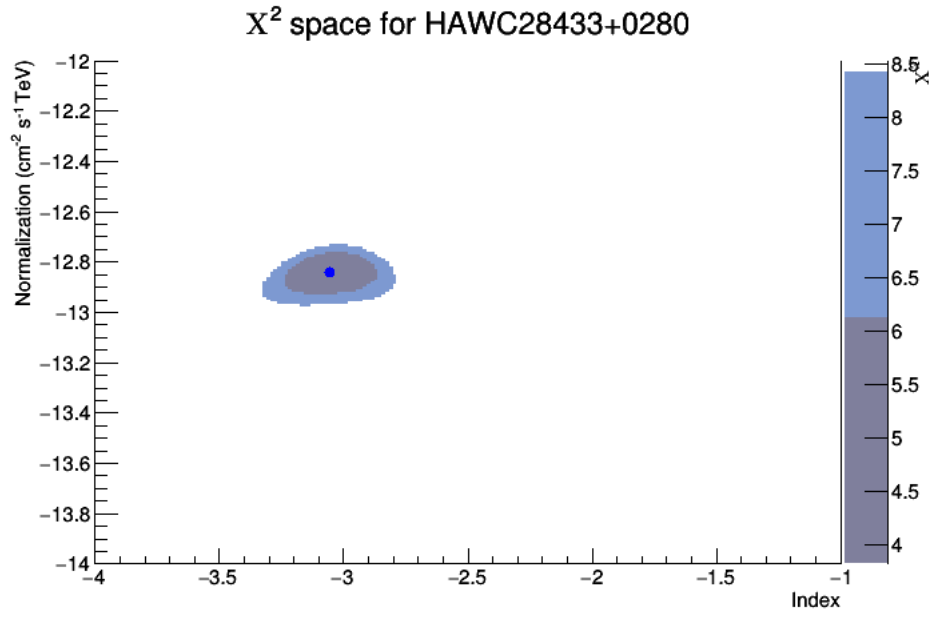


FIGURE 6.31. The  $\chi^2$  space for the fit of HAWC28433+0280. Dark blue is  $1\sigma$  uncertainty, and light blue is  $2\sigma$ .

## 6.8. HAWC28710+0643

Hotspot HAWC28710+0643 is closest in proximity to MGRO J1908+06. It was detected at  $14.26\sigma$  and fit using bins 2-9 (see figs. 6.32, 6.33, and 6.34), resulting in a spectrum of

$$\frac{dN}{dE}(\Phi_o, \gamma) = (1.48 \pm_{0.40}^{0.54} \text{ stat} \pm 0.28 \text{ sys}) \times 10^{-13} \left( \frac{E}{4\text{TeV}} \right)^{-2.65 \pm 0.11 \text{ stat} \pm 0.29 \text{ sys}},$$

with a  $\chi^2$  of 1.39 and 6 degrees of freedom (8 bins - 2 parameters).

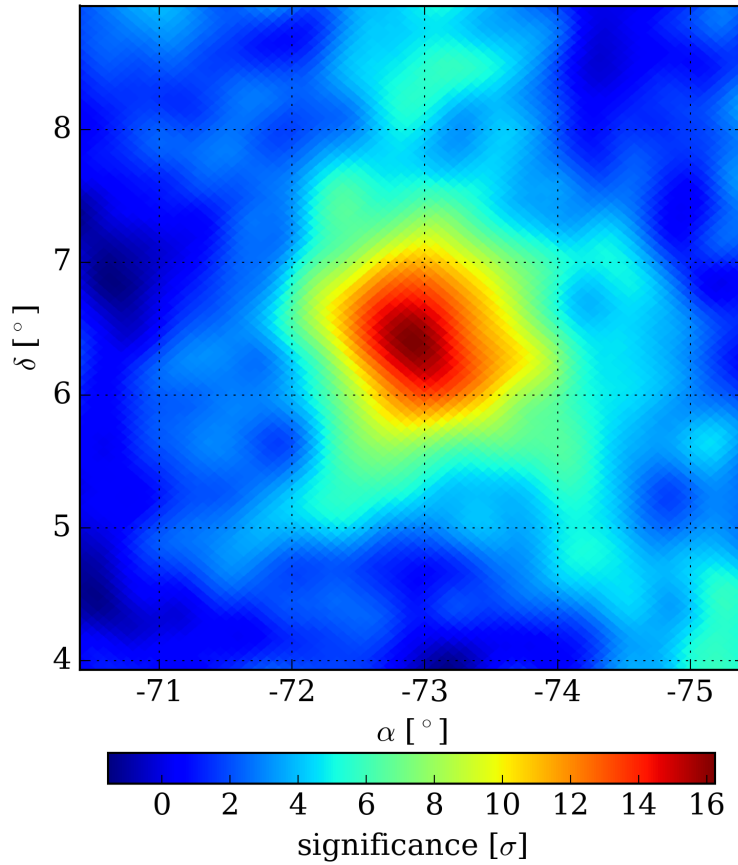


FIGURE 6.32. The hotspot HAWC28710+0643 as seen with the HAWC observatory.

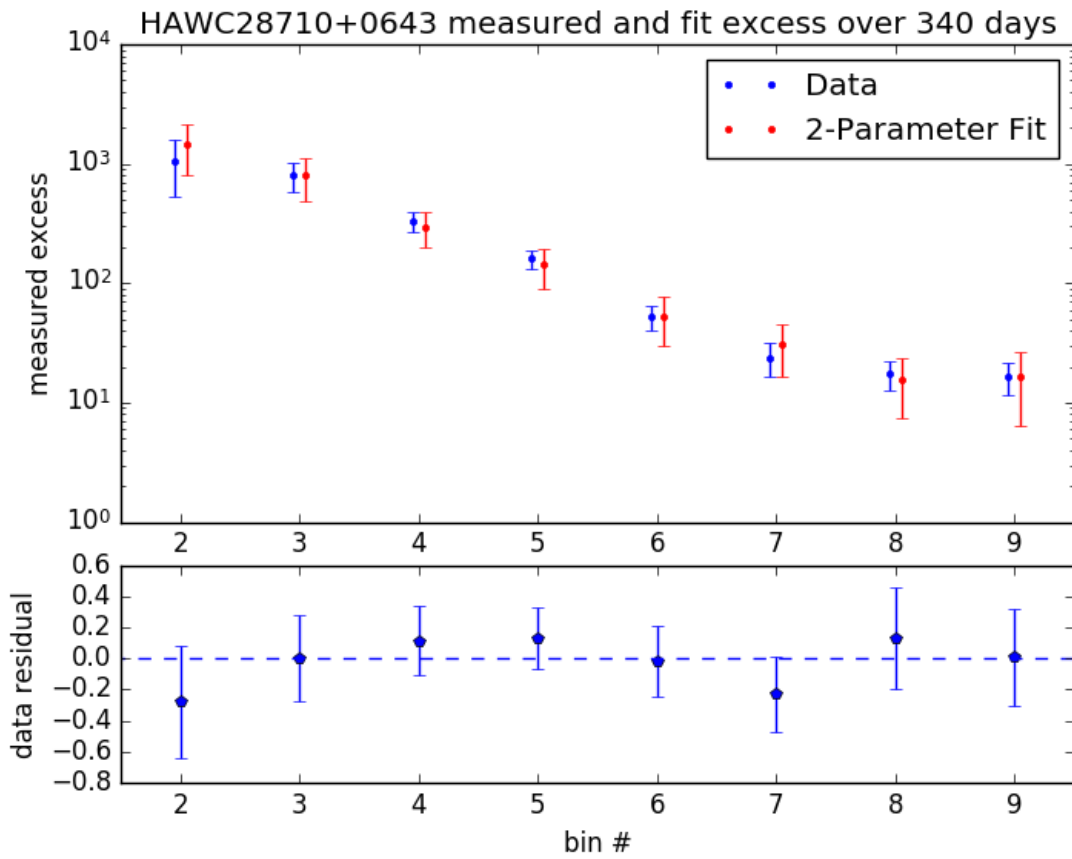


FIGURE 6.33. The measured excess form HAWC28710+0643 and the fit spectrum (top) and the residual, data-fit/fit (bottom).

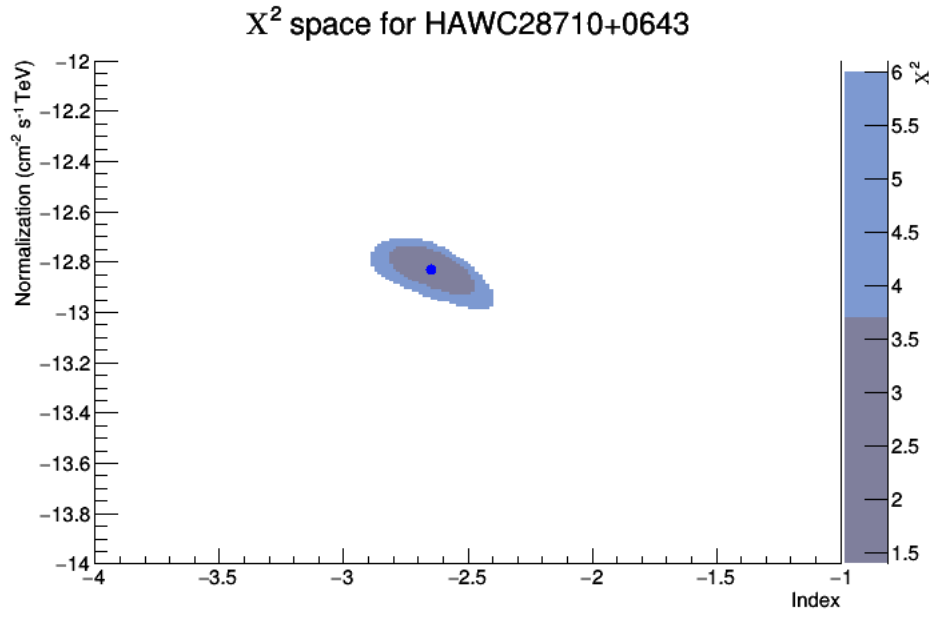


FIGURE 6.34. The  $\chi^2$  space for the fit of HAWC28710+0643. Dark blue is  $1\sigma$  uncertainty, and light blue is  $2\sigma$ .

## 6.9. HAWC30476+3680

Hotspot HAWC30476+3680 is closest in proximity to VER J2019+368. It was detected at  $15.43\sigma$  and fit using bins 2-9 (see figs. 6.35, 6.36, and 6.37), resulting in a spectrum of

$$\frac{dN}{dE}(\Phi_o, \gamma) = (1.14 \pm_{0.39}^{0.59} \text{ stat} \pm 0.21 \text{ sys}) \times 10^{-13} \left( \frac{E}{4\text{TeV}} \right)^{-2.46 \pm 0.11 \text{ stat} \pm 0.27 \text{ sys}},$$

with a  $\chi^2$  of 3.77 and 6 degrees of freedom (8 bins - 2 parameters).

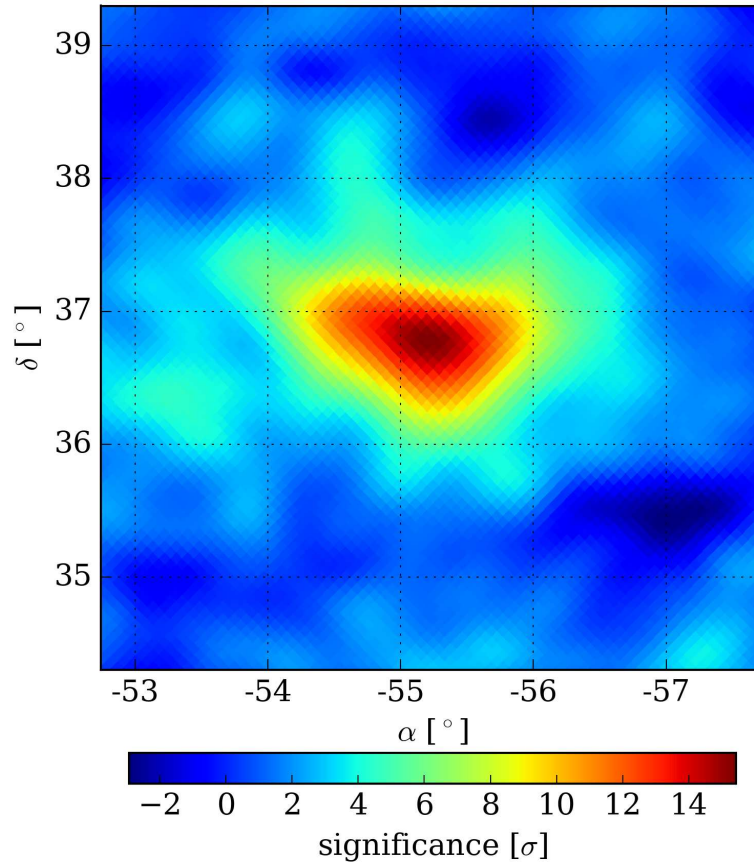


FIGURE 6.35. The hotspot HAWC30476+3680 as seen with the HAWC observatory.

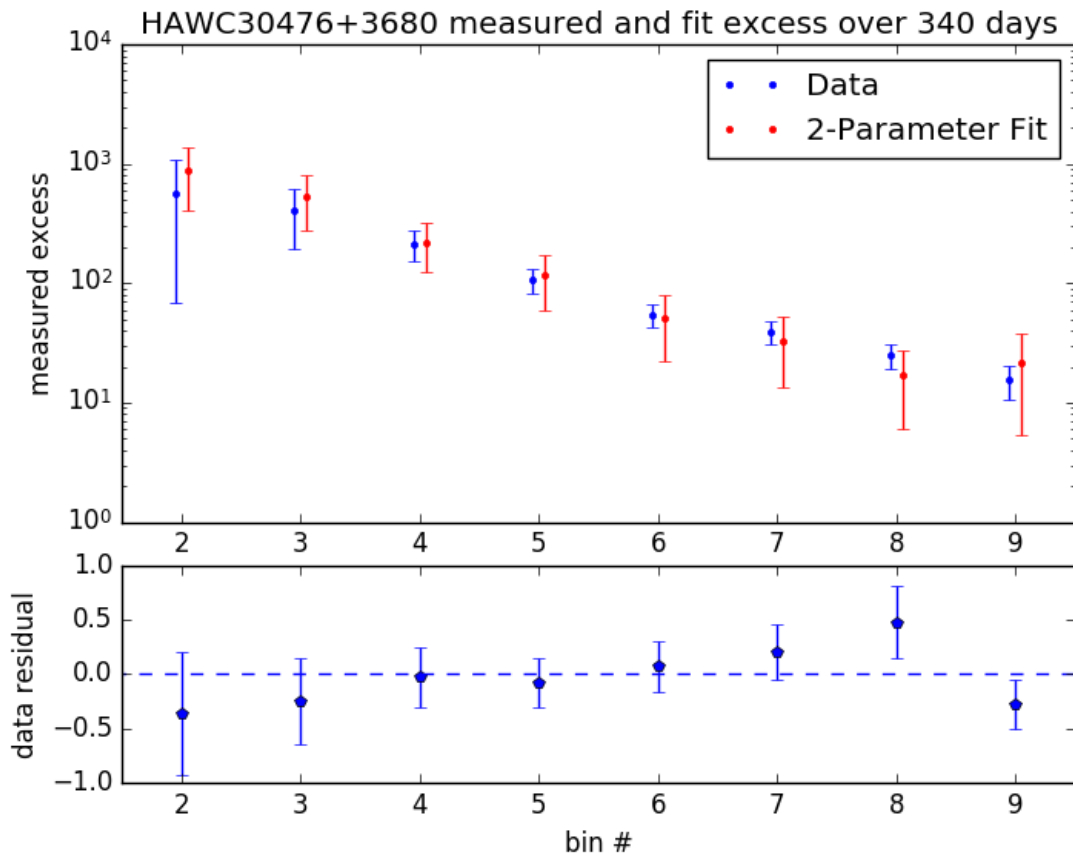


FIGURE 6.36. The measured excess form HAWC30476+3680 and the fit spectrum (top) and the residual, data-fit/fit (bottom).

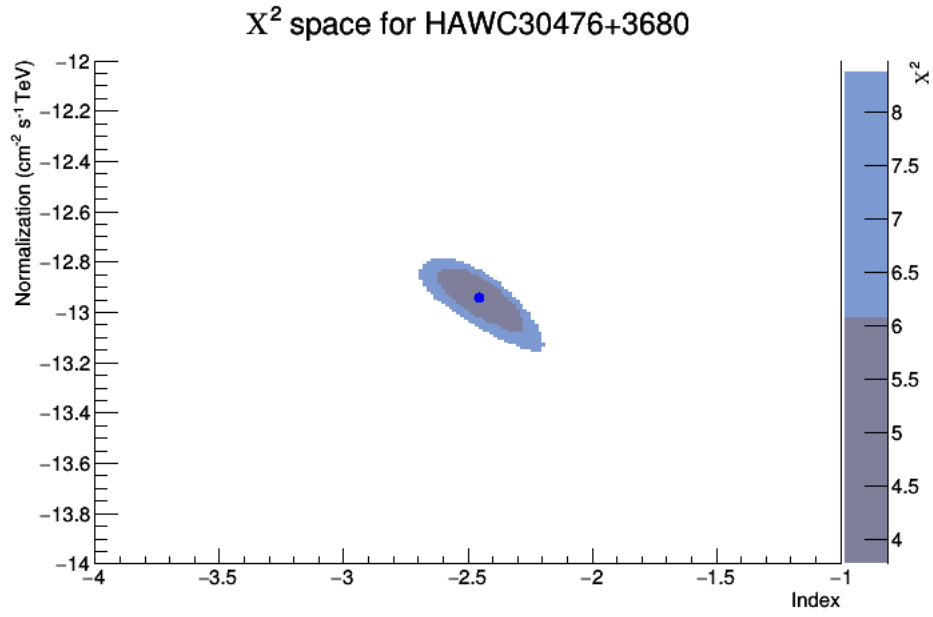


FIGURE 6.37. The  $\chi^2$  space for the fit of HAWC30476+3680. Dark blue is  $1\sigma$  uncertainty, and light blue is  $2\sigma$ .

## 6.10. HAWC30784+4151

Hotspot HAWC30784+4151 is closest in proximity to MGRO J2031+41. It was detected at  $10.32\sigma$  and fit using bins 2-9 (see figs. 6.38, 6.39, and 6.40), resulting in a spectrum of

$$\frac{dN}{dE}(\Phi_o, \gamma) = (9.12 \pm_{4.7}^{10.0} \text{ stat} \pm 1.7 \text{ sys}) \times 10^{-14} \left( \frac{E}{4\text{TeV}} \right)^{-2.52 \pm 0.22 \text{ stat} \pm 0.28 \text{ sys}},$$

with a  $\chi^2$  of 4.79 and 6 degrees of freedom (8 bins - 2 parameters). Because the uncertainty in the normalization is approximately the value itself, the fit cannot be constrained in normalization space.

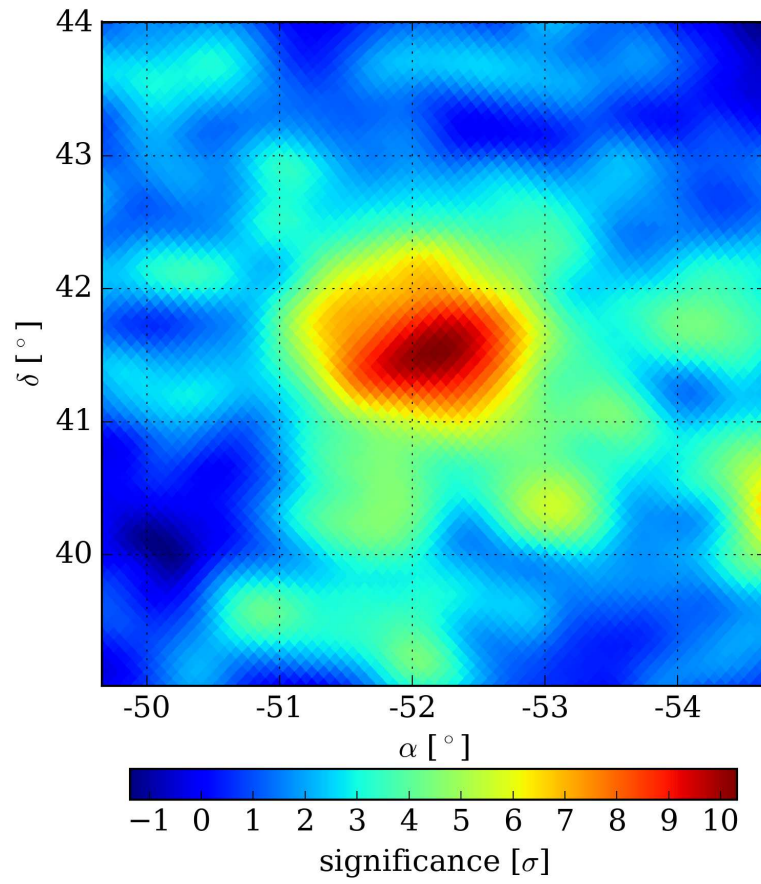


FIGURE 6.38. The hotspot HAWC30784+4151 as seen with the HAWC observatory.

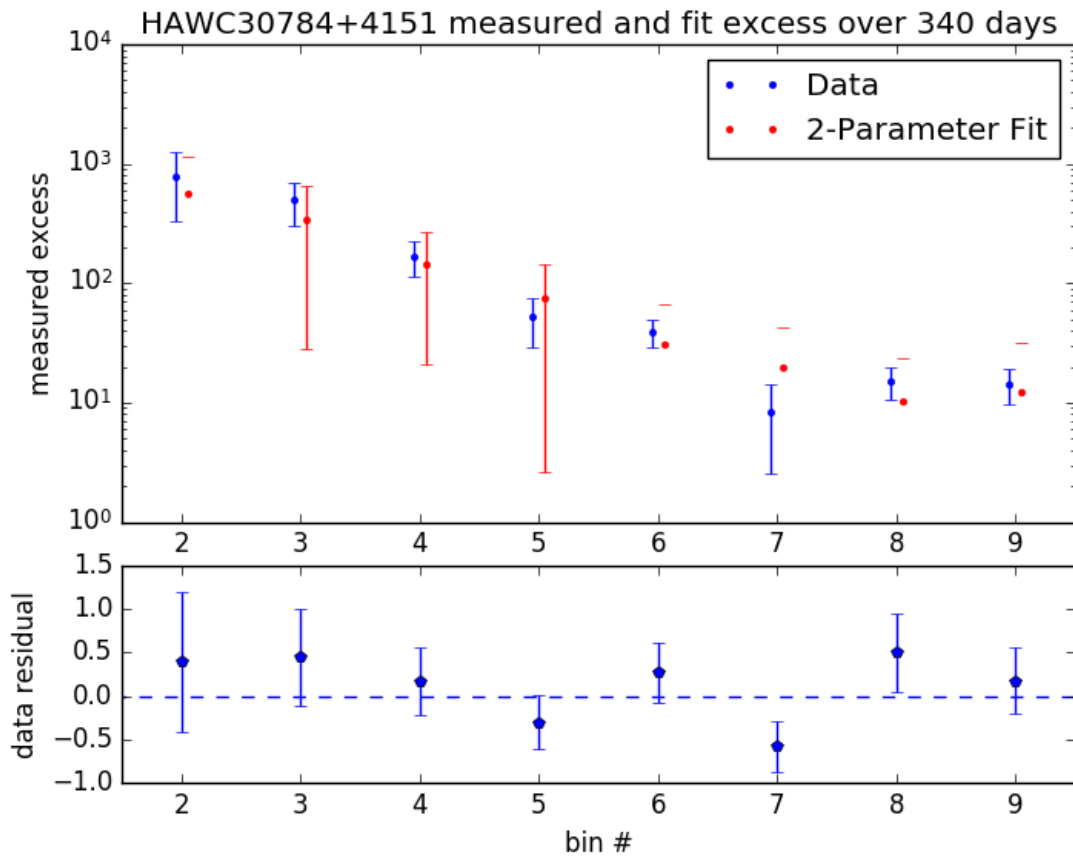


FIGURE 6.39. The measured excess form HAWC30784+4151 and the fit spectrum (top) and the residual, data-fit/fit (bottom).

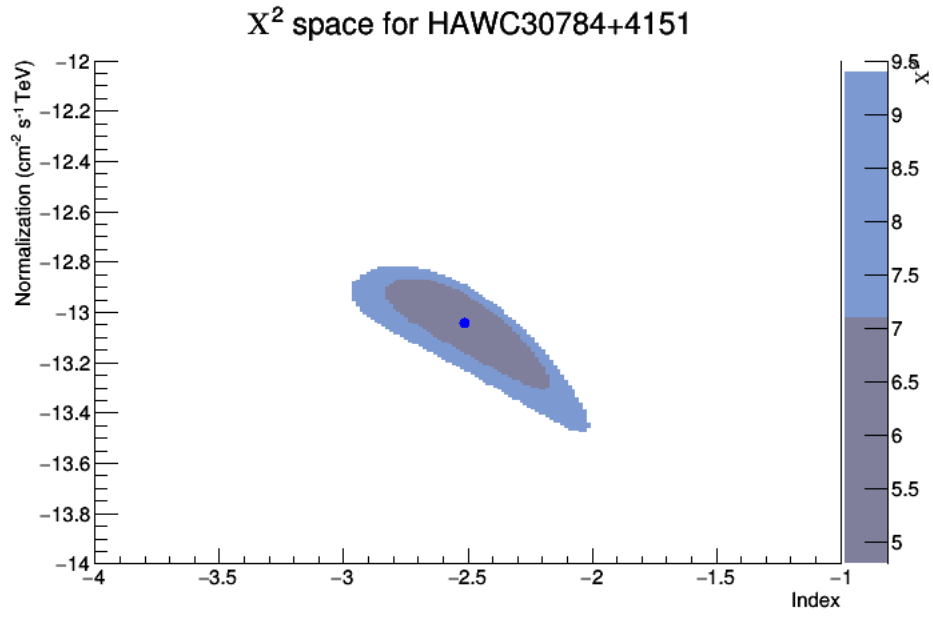


FIGURE 6.40. The  $\chi^2$  space for the fit of HAWC30784+4151. Dark blue is  $1\sigma$  uncertainty, and light blue is  $2\sigma$ .

## 6.11. GEMINGA

Geminga is a PWN located only 250 parsecs from Earth in the constellation of Gemini. Unlike the Crab, Geminga is highly extended, with a characteristic diameter of about  $3^\circ$ . TeV emissions were first reported by Milagro 2007 but were not definitively detected until 2009. For this analysis, a hot spot of  $5.6 \sigma$  was detected within the vicinity of Geminga at  $(97.91^\circ, 16.92^\circ)$  J2000 equatorial (see figs.6.41 6.42 and 6.43). Bins 4 through 9 were used and the resulting fit spectrum was

$$\frac{dN}{dE}(\Phi_o, \gamma) = (5.75 \pm_{3.7}^{10.4} \text{ stat} \pm 1.08 \text{ sys}) \times 10^{-14} \left( \frac{E}{4\text{TeV}} \right)^{-2.73 \pm 0.37 \text{ stat} \pm 0.30 \text{ sys}},$$

with a  $\chi^2$  of 0.99 and 3 degrees of freedom (5 bins - 2 parameters). Because the statistical uncertainty in normalization is greater than the value, the fit cannot be constrained in normalization space.

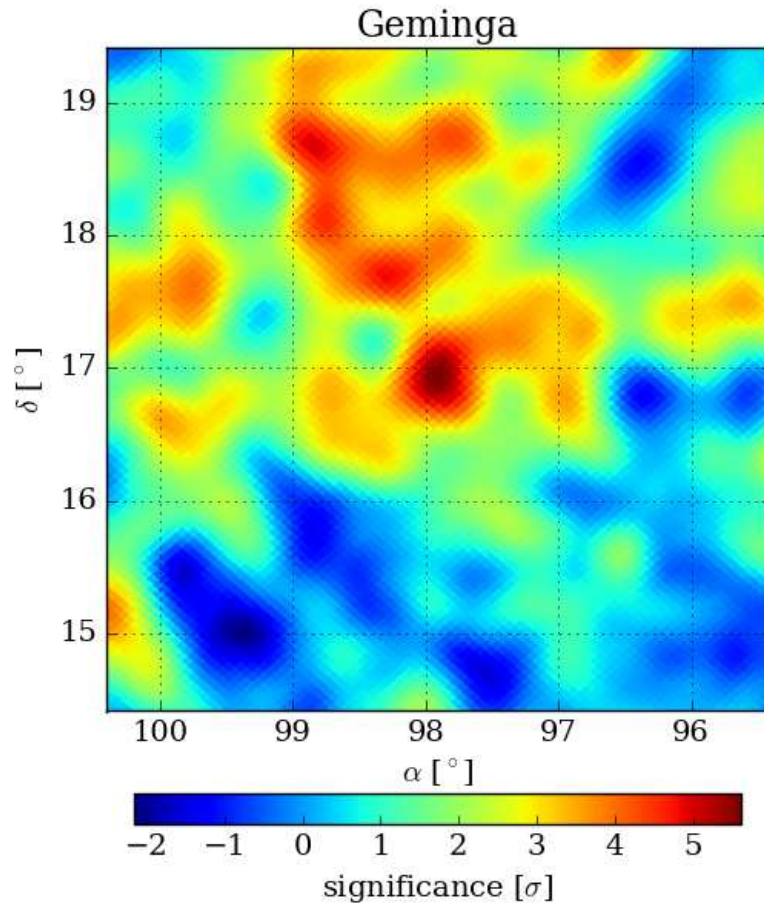


FIGURE 6.41. The PWN Geminga as seen with the HAWC observatory.

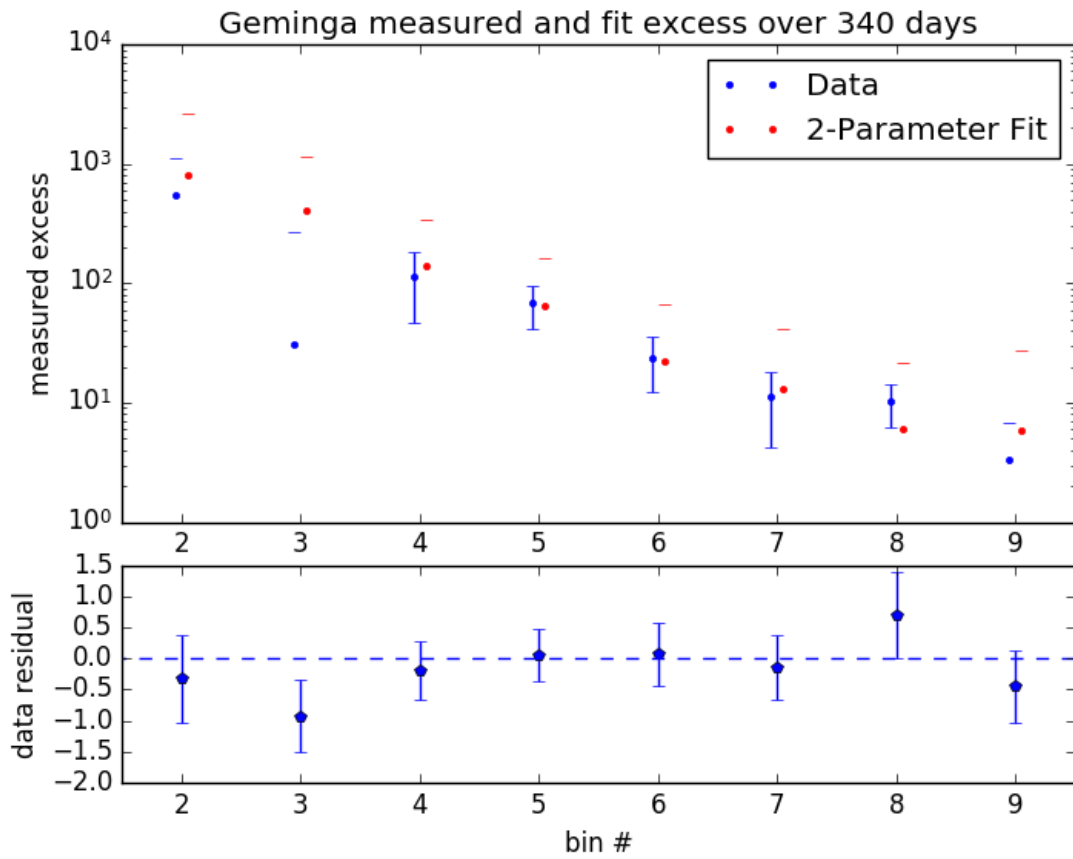


FIGURE 6.42. The measured excess from Geminga and the fit spectrum (top) and the residual, data-fit/fit (bottom).

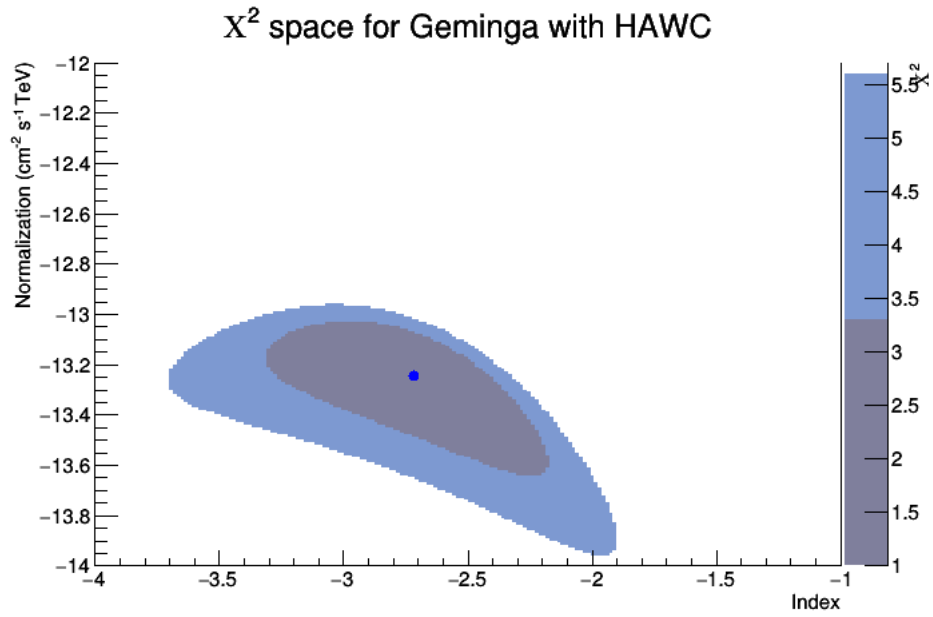


FIGURE 6.43. The  $\chi^2$  space for the fit of Geminga. Dark blue is  $1\sigma$  uncertainty, and light blue is  $2\sigma$ .

## CHAPTER 7

# CONCLUSIONS, DISCUSSION, FUTURE WORK

## AND ALL THAT JAZZ

The tabulated results from fitting sources can be seen in table 7.2. There are a few important conclusions to draw from them.

First, the minimum significance and normalization a source must have before a fit can be properly constrained is between 10 and 14  $\sigma$  with a normalization of at least  $10^{-13}\text{TeV}^{-1}\text{cm}^{-2}\text{s}^{-1}$ . Anything less than this results in an uncertainty on the normalization on the order of the normalization value. This means that the HAWC observatory can constrain the Crab with less than a week of observation time. Anything less than this and the fit uncertainties increase rapidly (see fig 7.1).

Second, the systematic uncertainties are reasonable but possibly unreliable. Quantitatively speaking, 19% on the normalization and 11% on the index is within the expected range for a particle array experiment. Milagro reported a systematic in normalization of 30% and a systematic in the index of 0.1 (about 5%)<sup>25</sup> [39]. Qualitatively, the reason why the systematics of this work should be considered unreliable comes from the effect of systematics that would not be detected by comparing simulations to data. For example, suppose the simulated PMTs trigger at a slightly different threshold than what is observed in HAWC. The trigger “rate” for all PMTs in the simulation would change, which would change the number of events per transit in every bin without changing the individual variable distributions. This

---

<sup>25</sup>HESS reports a systematic of 20% in normalization and .1 in index (on the order of 5%), and as an IACT with a comparable sensitivity to that of HAWC, I would expect HAWC to have an uncertainty close to or greater than this.

systematic would be entirely undetectable with the methods used for this analysis. Because of this, the reported systematic uncertainty should be considered lower limits.

Third, HAWC currently cannot constrain the cutoff energy, and this can be seen in the statistical uncertainties in the cutoff, which are on the order of the value. This is probably a result of the energy proxy chosen for this analysis, fHit. Because the energy resolution of HAWC is poor when using fHit, the cutoff energy should have an uncertainty of  $\pm 50\%$  at *best*. That said, the results from the Crab force the rejection of the two parameter model at a confidence above 95%. Even though the cutoff cannot currently be constrained with HAWC, this result strongly suggests that the two parameter model is an insufficient description of the physics at work within the Crab.

Finally, source identification is key to being able to get useful fit result. Consider HAWC27936-0665, HAWC27980-0583, and HAWC28107-0332. These are three hot spots that could very easily be three distinct sources, or a single source and two statistical fluctuations. There is no way to tell without having some measure of the statistical certainty that a given hot spot on the sky is a unique TeV source. As a result, there is no way to attribute the fit spectra to a specific source or physical process. A “clump” of sources on the sky might look like one very large source, and visa versa. This is especially apparent for Geminga, which is highly extended. The best way to mitigate this problem is to only apply this method to extra galactic sources, far from the galactic plane.

The most profitable direction for future work would be in the definition of a new energy proxy variable. A direct extension of fHit would be to examine the fraction of hits in PE bins, and derive an energy heuristic from that. For example, consider defining two PE bins: a low bin for hits with less than 10 PEs, and a high bin for hits more than 10 PEs. It is reasonable to assume that an event that triggers with an equal fraction of PMTs in the low

bin as the high bin would have *less* energy than an event that triggers with a significantly larger fraction of PMTs in the high bin than the low bin.

In general, this work demonstrates the ability to measure energy spectra *without* the need to directly measure primary energy. The methods presented here could be applied to any ground array experiment, which are possibly some of the least costly and most effective cosmic ray detectors at very high energies. This work also adds to our knowledge of the Crab nebula, the standard candle for any cosmic ray experiment. Further constraints on the spectrum of the Crab will improve the mathematical models we use to describe the processes at work. These models may directly lead to new particle acceleration technologies and applications.

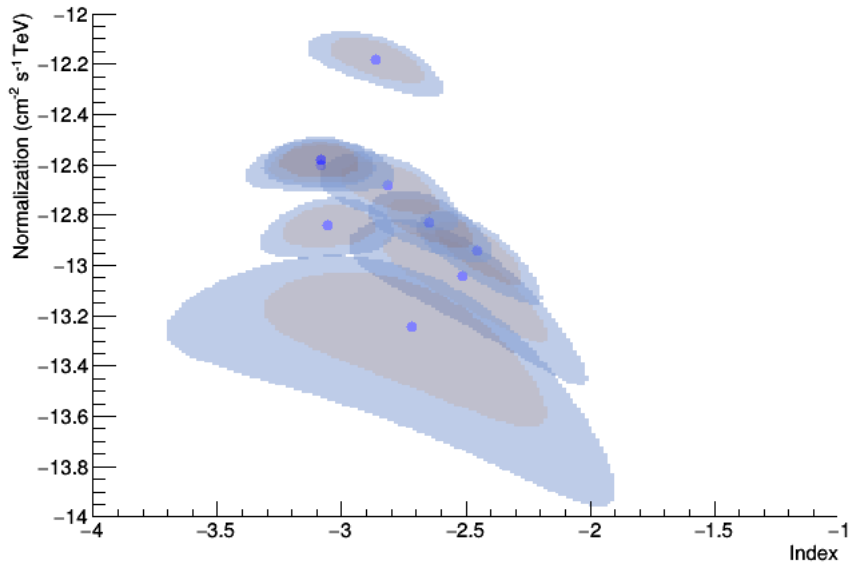


FIGURE 7.1. The  $\chi^2$  space for all sources that had a two parameter fit with a reasonable  $\chi^2$  overlaid on the same range. The change at  $10^{-13}$  is dramatic.

TABLE 7.1. Table of final 4.0 TeV, two parameter fit results determined by this analysis.

Designation	$\sigma$	Norm ( $\text{TeV}^{-1}\text{cm}^{-2}\text{s}^{-1}$ )	Index	$\chi^2/\text{DOF}$
HAWC27646-1340	19.3	$(6.61 \pm_{1.6}^{2.3} \text{ stat} \pm 1.2 \text{ sys}) \times 10^{-13}$	$-2.86 \pm 0.12 \text{ stat} \pm 0.31 \text{ sys}$	5.2 / 6
HAWC27936-0665	17.7	$(2.63 \pm_{0.53}^{0.66} \text{ stat} \pm 0.49 \text{ sys}) \times 10^{-13}$	$-3.09 \pm 0.10 \text{ stat} \pm 0.34 \text{ sys}$	10.02 / 6
HAWC27980-0583	16.7	$(2.51 \pm_{0.54}^{0.69} \text{ stat} \pm 0.47 \text{ sys}) \times 10^{-13}$	$-3.09 \pm 0.14 \text{ stat} \pm 0.34 \text{ sys}$	6.21 / 6
HAWC30476+3680	15.4	$(2.09 \pm_{0.63}^{0.91} \text{ stat} \pm 0.39 \text{ sys}) \times 10^{-13}$	$-2.82 \pm 0.13 \text{ stat} \pm 0.31 \text{ sys}$	0.59 / 6
HAWC27980-0583	14.3	$(1.45 \pm_{0.35}^{0.46} \text{ stat} \pm 0.27 \text{ sys}) \times 10^{-13}$	$-3.05 \pm 0.12 \text{ stat} \pm 0.34 \text{ sys}$	3.81 / 6
HAWC28433+0280	14.2	$(1.48 \pm_{0.40}^{0.54} \text{ stat} \pm 0.28 \text{ sys}) \times 10^{-13}$	$-2.65 \pm 0.11 \text{ stat} \pm 0.29 \text{ sys}$	1.39 / 6
HAWC28710+0643	14.2	$(1.14 \pm_{0.39}^{0.59} \text{ stat} \pm 0.21 \text{ sys}) \times 10^{-13}$	$-2.46 \pm 0.11 \text{ stat} \pm 0.27 \text{ sys}$	3.77 / 6
HAWC30784+4151	10.3	$(9.12 \pm_{4.7}^{10.0} \text{ stat} \pm 1.7 \text{ sys}) \times 10^{-14}$	$-2.52 \pm 0.22 \text{ stat} \pm 0.28 \text{ sys}$	4.79 / 6
Geminga	5.6	$(5.75 \pm_{3.7}^{10.4} \text{ stat} \pm 1.08 \text{ sys}) \times 10^{-14}$	$-2.73 \pm 0.37 \text{ stat} \pm 0.30 \text{ sys}$	0.99 / 3

TABLE 7.2. Table of final 4.0 TeV, three parameter fit results determined by this analysis.

Designation	$\sigma$	Norm ( $\text{TeV}^{-1}\text{cm}^{-2}\text{s}^{-1}$ )	Index	Cutoff (TeV)	$\chi^2/\text{DOF}$
Crab	83	$(1.03 \pm_{0.083}^{0.091} \text{ stat} \pm 0.19 \text{ sys}) \times 10^{-12}$	$-2.54 \pm 0.095 \text{ stat} \pm 0.27 \text{ sys}$	$91.0 \pm_{59}^{174} \text{ stat}$	5.87 / 5
Markarian 421	32	$(1.23 \pm_{0.91}^{3.6} \text{ stat} \pm 0.23 \text{ sys}) \times 10^{-12}$	$-2.61 \pm 0.39 \text{ stat} \pm 0.28 \text{ sys}$	$6.4 \pm_{4.3}^{12} \text{ stat}$	4.74 / 5
Markarian 501	21	$(7.25 \pm_{2.8}^{4.7} \text{ stat} \pm 1.4 \text{ sys}) \times 10^{-13}$	$-2.19 \pm 0.31 \text{ stat} \pm 0.24 \text{ sys}$	$7.94 \pm_{5.3}^{16} \text{ stat}$	2.66 / 5

## BIBLIOGRAPHY

- [1] P. D. Group, *Cosmic Rays, Physics Letters B* **667** (2008) 254–260.
- [2] G. T. K. Cronin J and S. S. P, *Cosmic rays at the energy frontier, Scientific American* **276** (1, 1997).
- [3] P. Sommers and S. Westerhoff, *Cosmic Ray Astronomy, New Journal of Physics* **11** (2009).
- [4] R. Beck and P. Hoernes, *Magnetic spiral arms in the galaxy NGC6946, Nature* **379** 47–49.
- [5] K. Greisen, *End to the Cosmic Ray Spectrum?, Physical Review Letters* **16(17)** 748–750.
- [6] V. A. Zatsepin, G. T.; Kuz'min, *Upper Limit of the Spectrum of Cosmic Rays, Journal of Experimental and Theoretical Physics Letters* **4** 78–80.
- [7] T. P. A. Collaboration, *Measurement of the energy spectrum of cosmic rays above  $10^{18}$  eV using the Pierre Auger Observatory, Physics Letters B* **685(4-5)** 239–246.
- [8] T. H. Collaboration, *Final Results from the High Resolution Fly's Eye (HiRes) Experiment, Nuclear Physics B Proceedings Supplements* **212** 74–78.
- [9] E. Fermi, *On the Origin of the Cosmic Radiation, Physical Review* **75** 1169–1174.
- [10] D. Perkins, *PARTICLE Astrophysics*. Oxford Univ. Press, 4 ed., 2006.
- [11] G. B. Gelmini, *High energy cosmic rays, J. Phys. Conf. Ser.* **171** (2009) 012012, [arXiv:0903.4716].
- [12] D. G., “Gamma-ray binaries and related systems.”.
- [13] T. V. Collaboration, *Observations of the Crab Pulsar with VERITAS, ArXiv e-prints* (2013) [1303.0275].

- [14] J. W. T. Hessels et al., *A Radio Pulsar Spinning at 716 Hz*, *Science* **331** (2006) 1901–1904.
- [15] A. Abramowski et al., *Very-high-energy gamma-ray emission from the direction of the Galactic globular cluster Terzan 5*, *Astronomy and Astrophysics* **531** (2011) L18.
- [16] K. Makishima et al., *Discovery of two new burst sources in the globular clusters Terzan 1 and Terzan 5*, *The Astrophysical Journal* **247** (1981) L23–25.
- [17] T. F.-L. Collaboration, *GeV Observations of Star-forming Galaxies with the Fermi Large Area Telescope*, *Astrophysical Journal* **755** (2012) [1206.1346].
- [18] T. H. Collaboration, *On the nature of HESS J1503-582 revealed by the H.E.S.S. experiment: Coincidence with a FVW?*, in *American Institute of Physics Conference Series*, vol. 1085 of *American Institute of Physics Conference Series*, pp. 281–284, 2008. 1206.1346.
- [19] J. M. Jauch and F. Rohrlich, *The theory of photons and electrons : the relativistic quantum field theory of charged pARTICLES with spin one-half / J. M. Jauch and F. Rohrlich*. Springer-Verlag New York, 2d expanded ed. ed., 1976.
- [20] A. Abdo et al., *Milagro Observations of TeV Emission from Galactic Sources in the Fermi Bright Source List*, *Astrophys.J.* **700** (2009) L127–L131, [arXiv:0904.1018].
- [21] Milagro Collaboration, R. W. Atkins et al., *TeV gamma-ray survey of the Northern hemisphere sky using the Milagro Observatory*, astro-ph/0403097.
- [22] H. Collaboration, “Construction of the HAWC Gamma-Ray Observatory.” HAWC proposal to NSF, 2011.
- [23] J. Wood, “Random 2 edge pairs vs. real 4 edge hits.” [http://private.hawc-observatory.org/wiki/images/b/b5/2014-03-25\\_pe-promotion.pdf](http://private.hawc-observatory.org/wiki/images/b/b5/2014-03-25_pe-promotion.pdf), March, 2014.

- [24] G. Moliere, *Theorie der streuung schneller geladener teilchen i: Einzelstreuung am abgeschirmten coulomb-feld*, *A Journal of Physical Sciences* **2** (1947).
- [25] N. N. Kalmykov et al., *On the choice of the lateral distribution function for eas charged particles*, *Bulletin of the Russian Academy of Sciences: Physics* **71** (4, 2007).
- [26] B. Dingus, *Study of Ultra-High Energy Emissions from Cygnus X-3 and Hercules X-1*. PhD thesis, University of Maryland, 1988.
- [27] D. Heck et al., *CORSIKA: a Monte Carlo code to simulate extensive air showers*. Feb, 1998. Forschungszentrum Karlsruhe GmbH, Karlsruhe (Germany).
- [28] K. Werner, *Strings, pomerons and the venus model of hadronic interactions at ultrarelativistic energies*, *Physics Reports* **232** (9, 1993).
- [29] S. Ostapchenkov, *Qgsjet-ii: towards reliable description of very high energy hadronic interactions*, *Nuclear Physics B Proceedings Supplements* **151** (1, 2006).
- [30] J. Ranft, *Dual parton model at cosmic ray energies*, *Phys. Rev. D* **51** (1, 1995).
- [31] R. S. Fletcher, T. K. Gaisser, P. Lipari, and T. Stanev, *sibyll: An event generator for simulation of high energy cosmic ray cascades*, *Phys. Rev. D* **50** (11, 1994).
- [32] H. Fesefeldt, *The simulation of hadronic showers: Physics and applications*, tech. rep., PITHA-85/02 (RWTH Aachen).
- [33] T. B. et al., *The fluka code: Developments and challenges for high energy and medical applications*, *Nuclear Data Sheets* **120** (2014).
- [34] S. A. Bass et al.
- [35] H. Hirayama et al., *The egs5 code system*, tech. rep., Stanford Linear Accelerator Center, Standford University, 2005. available from <http://slac.stanford.edu/cgi-wrap/getdoc/slac-r-730.pdf>.

- [36] R. Sternheimer et al., *Density effect for the ionization loss of charged particles in various substances*, *Atomic Data and Nuclear Data Tables* **30** (3, 1984).
- [37] B. M. Gaensler and P. O. Slane, *The evolution and structure of pulsar wind nebulae*, *Ann.Rev.Astron.Astrophys.* **44** (2006) 17–47, [[astro-ph/0601081](#)].
- [38] A. A. Fermi Collaboration Abdo et al., *Gamma-Ray Flares from the Crab Nebula*, *Science* **331** (Feb., 2011) 739–, [[arXiv:1011.3855](#)].
- [39] M. Collaboration, *Observation and Spectral Measurements of the Crab Nebula with Milagro*, *Astrophysical Journal* **750** (may, 2012) 63, [[arXiv:1110.0409](#)].
- [40] HESS, F. Aharonian, *HESS VHE Gamma-Ray Sources Without Identified Counterparts*, *Astron.Astrophys.* **477** (2008) 353–363, [[arXiv:0712.1173](#)].
- [41] VERITAS Collaboration: J. Grube, *Observations of the Crab Nebula with the Whipple 10 m Telescope*, *ArXiv e-prints* (Sept., 2007) [[arXiv:0709.4300](#)].
- [42] P. K. F. Grieder, *Extensive Air Showers: High Energy Phenomena and Astrophysical Aspects A Tutorial, Reference Manual and Data Book*. Springer Berlin Heidelberg, 2010.
- [43] T.-P. Li and Y.-Q. Ma, *Analysis methods for results in gamma-ray astronomy*, *The Astrophysical Journal* **272** (sep, 1983) 317–324.
- [44] J. R. Taylor, *An Introduction to Error Analysis*. University Science Books, 2 ed., 1997.
- [45] E. M. Pugh and G. H. Winslow, *The Analysis of Physical Measurements*. Addison-Wesley, 1 ed., 1966.
- [46] Y. Avni, *Energy spectra of x-ray clusters of galaxies*, *Astrophysical Journal* **210** (Dec, 1976) 642–646.
- [47] A. A. Fermi Collaboration Abdo et al., *Binned grb spectral analysis*, may, 2015.